Development of CO_2 stable $(La_{0.6}Ca_{0.4})(Co_{0.8}Fe_{0.2})O_{3-\delta}$ hollow fiber membranes for the plasma induced CO_2 conversion

Von der Naturwissenschaftlichen Fakultät der

Gottfried Wilhelm Leibniz Universität Hannover

zur Erlangung des Grades

Doktor der Naturwissenschaften

(Dr. rer. nat.)

genehmigte Dissertation

von

Frederic Felix Buck, M.Sc.

(2021)

Referent: Prof. Dr. rer. nat. Jürgen Caro

Korreferent: Apl. Prof. Dr. rer. nat. habil. Armin Feldhoff

Tag der Promotion: 11. November 2021

Preface

The present results of this thesis were obtained since March 2018 during my Ph.D. study at Fraunhofer Institute for Interfacial Engineering and Biotechnology (IGB) in Stuttgart. The thesis was supervised by Prof. Dr. Jürgen Caro from the Gottfried Wilhelm Leibniz Universität Hannover. In this period, I worked on the project PiCK (Plasma induzierte CO_2 Konversion, project number: 03SFK2S3).

Four research papers in which I am the first author are included in this work. The following statement will clarify my contribution to the articles used in this thesis. For all articles, I would like to express my attitude for the comments and fruitful discussion from the co-authors and the referees, particularly from Prof. Dr. J. Caro, Prof. Dr. A. Feldhoff and Dr. T. Schiestel.

The first article "Use of Perovskite Hollow Fiber Membranes in a Microwave Plasma" was written by me. I got support on the manuscript preparation from all the co-authors, especially from Dr. T. Schiestel. The manufacturing and the permeation tests were done by myself. The experiments in the air plasma were done by Irina Kistner (Institute of Interfacial Process Engineering and Plasma Technology (IGVP), Universität Stuttgart) and me. The SEM images were done by Monika Riedl (IGB).

The first draft of the second article "Permeation improvement of LCCF hollow fiber membranes by spinning and sintering optimization" was written by me. Dr. T. Schiestel, Prof. Dr. A. Feldhoff and Prof. Dr. J. Caro spent much time on correcting and improving the article. The manufacturing of the hollow fibers and the permeation tests were done by me. The characterization of the hollow fibers with SEM, EDXS, TEM and XRD was done by Prof. Dr. A. Feldhoff (Institute of Physical Chemistry and Electrochemistry, Leibniz Universität Hannover).

The third article "High flux CO_2 stable oxygen transport hollow fiber membranes through surface engineering" was written by me, optimized and modified by Prof. Dr. J. Caro and Dr. T. Schiestel. The manufacturing and coating of the asymmetric hollow fibers were done by Osman Bunjaku (IGB) together with me. The etching of the fibers and the permeation measurements were done by myself. The EDX and SEM measurements were done by Monika Riedl (IGB).

The fourth article "Effect of plasma atmosphere on the oxygen transport of mixed ionic and electronic conducting hollow fiber membranes" was written by me. I got support on the manuscript from all the co-authors, especially by Thomas Schiestel. The manufacturing of the hollow fibers and the permeation test in the oven were done by me. The temperature

measurements and the permeation measurements in the plasma were done by Katharina Wiegers (IGVP) and me together. The measurements of the plasma composition were done by Katharina Wiegers. The SEM images were done by Monika Riedl (IGB).

Acknowledgement

First of all, I would like to express my appreciation to Prof. J. Caro for giving me this opportunity to do my Ph. D. thesis under his supervision. I am deeply thankful for his support and patient guidance throughout my entire Ph. D. thesis.

I am honoured that Prof. Dr. Armin Feldhoff managed to be my co-referee. Because of his membrane knowledge and activities this is a benefit to my promotion.

A special thank you goes to Dr. Thomas Schiestel, whose door was always open to me for questions and problems. Above all, you have always motivated me in countless meetings, asked the right questions and given me new impulses for the progress of my work.

Then I want to thank my Ph. D. colleague, Sarah Übele, for everything that good roomies do: supporting each other, discussing and having fun.

Furthermore, I want to thank my colleagues from the "Innovationsfeld Membrane" with Christopher Hänel, Marita Southan, Bentsian Elkin, Monika Riedl Janina Kapp, Tobias Götz, Chayenne Tasche and Max Witte for the technical cooperation and the helpfulness. In addition, every single one of them made sure that there was always something to laugh about in everyday work. It was always a pleasure to come to work.

I also want to thank Irina Kistner, Katharina Wiegers and Andreas Schulz from the Institute of Interfacial Process Engineering and Plasma Technology (IGVP) for the good collaboration and the help to understand the plasma process.

I became support from several students, who made a direct or indirect contribution to this thesis. In chronological order: Nikos Alexiadis, Noah Keim, Fawaz Al Hussein and Osman Bunjaku.

My parents cannot be thanked enough for their never-ending support and advice, anytime and in every way.

And last, but certainly not least, my dear Corina. Without your love, patience and support this work was probably never finished. I am looking forward to new experiences and challenges with you.

Abstract

The present work deals with the perovskite $(La_{0.6}Ca_{0.4})(Co_{0.8}Fe_{0.2})O_{3-\delta}$ (LCCF) in the form of dense hollow fiber membranes for the oxygen separation from CO_2 containing gas mixtures. A potential application is the in situ extraction of oxygen from a CO_2 plasma. In such a plasma, the CO_2 can be split into CO and oxygen by microwave energy. The goal of this work was the development of LCCF hollow fiber membranes, the optimization of the oxygen transport through these membranes and to confirm the applicability of the extraction of oxygen from a CO_2 plasma. Prerequisite for the material and the membrane was a good CO_2 stability and a good thermal shock resistance. In a long-term test (>200 h) at 900 °C a good CO_2 stability could be verified.

To optimize the oxygen permeation flux through the membrane, the bulk diffusion and the surface exchange reactions were affected. To optimize the bulk diffusion, hollow fiber membranes with different wall thicknesses and different sintering temperatures were manufactured. With a wall thickness of 81 µm and a sintering temperature of 1220 °C the highest oxygen permeation flux (6.2 ml min^{-1} cm^{-2} at 1000 °C) in a CO_2 containing atmosphere could be achieved.

The surface exchange reactions were affected by the surface etching method. The goal was to increase the roughness of the surfaces, what could be obtained, by H_2SO_4 treatment. The best results could be achieved by treating the inner and outer surface with H_2SO_4 for 180 min. The permeation flux could be increased by 86 % compared to the pristine hollow fiber.

Furthermore, both permeation limiting steps were addressed by developing asymmetric hollow fibers with a porous support of LCCF and a thin dense layer of LCCF. A gastight dense layer of 22 µm could be achieved. The oxygen permeation flux compared to a dense hollow fiber membrane (wall thickness 179 µm) could be improved by 68.6 %.

Finally, the applicability of the plasma induced CO_2 conversion was analysed. The oxygen permeation flux of LCCF hollow fiber membranes in different plasmas (air and CO_2) were compared with the permeation in an oven heated system. The permeation in an air plasma was 60.6 % higher at a similar temperature, which is caused by the special plasma atmosphere. In the CO_2 plasma, the feasibility of the conversion of CO_2 in oxygen and CO could be proven and the generated oxygen can be extracted through the LCCF hollow fiber membranes. At a microwave power of 1 kW an oxygen permeation flux of 4.96 ml min^{-1} cm^{-2} in a CO_2 plasma could be achieved.

Keywords: Plasma, CO_2 conversion, MIEC hollow fiber membranes, oxygen permeation

Kurzfassung

Die vorliegende Arbeit beschäftigt sich mit dem Perowskit $(La_{0.6}Ca_{0.4})(Co_{0.8}Fe_{0.2})O_{3-\delta}$ (LCCF) in Form von dichten Hohlfasermembranen zur Sauerstoffabtrennung aus CO_2-haltigen Gasgemischen. Eine mögliche Anwendung ist die in-situ-Extraktion von Sauerstoff aus einem CO_2-Plasma. Im thermischen Plasma dissoziiert CO_2 zu CO und Sauerstoff. Ziel dieser Arbeit war es, Hohlfasern aus LCCF herzustellen, den Sauerstofftransport durch die Membran zu optimieren und die Anwendbarkeit der O_2-Gewinnung aus einem CO_2-Plasma nachzuweisen. Voraussetzung für das Material ist eine gute CO_2-Stabilität und eine gute Temperaturwechselbeständigkeit. In einem Langzeittest (>200 h) bei 900 °C konnte die gute CO_2-Stabilität nachgewiesen werden.

Um den O_2-Fluss durch die Membran zu optimieren wurden die Volumendiffusion und die Oberflächenaustauschreaktionen beeinflusst. Zur Optimierung der Volumendiffusion wurden Hohlfasermembranen bei unterschiedlichen Sintertemperaturen und mit unterschiedlichen Wandstärken hergestellt. Bei einer Wandstärke von 81 µm und einer Sintertemperatur von 1220 °C konnte der höchste Sauerstoff-Fluss (6.2 ml min^{-1} cm^{-2} bei 1000 °C) in einer CO_2-haltigen Atmosphäre erreicht werden.

Die Oberflächenaustauschreaktionen wurden durch das Oberflächenätzverfahren verändert. Ziel war es, die Rauheit der Oberflächen zu erhöhen, was durch eine Behandlung mit H_2SO_4 erfolgreich durchgeführt wurde. Das beste Ergebnis konnte erzielt werden, wenn sowohl die Innen- als auch die Außenseite für 180 min mit H_2SO_4 behandelt wurden. Der Fluss stieg um 86 % im Vergleich zu einer makellosen Hohlfaser. Darüber hinaus wurden beide permeationslimitierenden Schritte modifiziert, indem asymmetrische Hohlfasern mit einem porösen Träger aus LCCF und einer dünnen dichten Schicht aus LCCF hergestellt wurden. Es konnte eine dichte Schicht von 22 µm erreicht werden. Der O_2-Fluss gegenüber einer dichten Hohlfasermembran (179 µm) wurde um 68.6 % verbessert.

Zum Schluss wurde die Anwendbarkeit der plasmainduzierten CO_2-Umwandlung analysiert. Der O_2-Fluss von LCCF Hohlfasermembranen in verschiedenen Plasmen (Luft und CO_2) wurde mit dem ofenbeheizten System verglichen. Das Luftplasma wies bei ähnlicher Temperatur einen 60.6 % höheren Sauerstoff-Fluss auf, was auf die spezielle Plasmaatmosphäre zurückzuführen ist. Im CO_2-Plasma konnte die Machbarkeit der Umwandlung von CO_2 in Sauerstoff und CO nachgewiesen werden und der erzeugte Sauerstoff durch die LCCF-Hohlfasermembranen abgetrennt werden. Bei einer Mikrowellenleistung von 1 kW konnte ein O_2-Fluss von 4.96 ml min^{-1} cm^{-2} in einem CO_2-Plasma erreicht werden.

Schlagwörter: Plasma, CO_2 Konversion, MIEC Hohlfasermembran, Sauerstoffpermeation

Table of Content

List of Figures

List of Acronyms

Acronym

A	First cation species at A-position
A'	Second cation species at A-position
a^3	Atomic volume
A_M	Effective membrane area
APS	Atmospheric plasma systems
B	First cation species at B-position
B'	Second cation species at B-position
c	Concentration
d	Membrane thickness
D*	Self-diffusion coefficient
D_i	Inner diameter
D_o	Outer diameter
D_K	Diffusivity (Knudsen)
E_A	Activation energy
EDXS	Energy dispersive X-ray spectroscopy
EES	Energy storage systems
F_B	Bending strength
G_m	Gibbs free energy
GHG	Greenhouse gases
H	Enthalpy
J	Permeation flux
K	Equilibrium constant
L_c	Critical membrane thickness
LCCF	$(La_{0.6}Ca_{0.4})(Co_{0.8}Fe_{0.2})O_{3-\delta}$
M	Molar mass
MIEC	Mixed ionic electronic conductor
n	Fitting parameter (Wagner equation)
NIPS	Non solvent induced phase inversion
NEP	N-ethyl-2-pyrrolidone
p	Pressure

PEI	Polyetherimide
PiCK	Plasma induced CO_2-conversion
PVP	Polyvinylpyrrolidone
r	Radius
S	Entropy
SEM	Scanning electron microscopy
t	Time
t_G	Goldschmidt´s tolerance factor
T	Temperature
T_S	Sintering temperature
TEM	Transmission electron microscopy
$\dot{V}_{Feed}$	Feed flow
$\dot{V}_{Gas}$	Gas flow
$\dot{V}_{Sweep}$	Sweep flow
XRD	X-Ray diffraction

Greek letter

δ	Amount of oxygen vacancies
γ	Surface energy
η	Dynamic viscosity
μ	Chemical potential
σ_{el}	Electric conductivity
σ_{ion}	Ionic conductivity

Units

K	Kelvin
J	Joule
mol	Amount of substance
s	Second
min	Minute
cm	Centimeter
g	Gramm
ppm	Parts per Million

h	Hour
N	Newton
µm	Micrometer

Constants

F	Faraday constant with $9.649 \cdot 10^4$ A s mol^{-1}
g	Gravity with 9.81 m s^{-2}
K	Boltzmann constant with $1.381 \cdot 10^{-23}$ J K^{-1}
R	Universal gas constant with 8.314 J mol^{-1} K^{-1}

1. Introduction

1.1. Motivation

1.5 °C. This was and still is the common goal of the Paris agreement which was signed by 196 countries in 2015 [1, 2]. The limitation of the global warming compared to the pre-industrial era to 1.5 °C should be achieved until 2050. To reach the target, the emissions of greenhouse gases need to be reduced. However, most countries are far away from fulfilling this goal.

In the pre-industrial era the CO_2 content in the atmosphere was relatively low (280 ppm) and the carbon cycle was in good balance [3, 4]. With the beginning of the industrial revolution, large reservoirs of carbon based fossil resources were utilized to reach a new age of technological and economic growth, productivity and quality of life. By burning fossil fuels, the carbon cycle is changed because carbon, which was stored for millions of years, is released to the atmosphere in form of CO_2. Between 2009 and 2018 the total CO_2 emission was 11 GtC yr^{-1} (gigatonnes of carbons per year) caused by fossil CO_2 emission (9.5 GtC yr^{-1}) and land use change emissions (1.5 GtC yr^{-1}), while ocean and terrestrial sinks absorbed 5.7 GtC yr^{-1} and the atmospheric CO_2 amount increased by 4.9 GtC yr^{-1} [4]. The negative imbalance means the emissions are underestimated and/or the sinks are too big. The effect of this perturbations leads to ocean acidification and surface warming due to a higher CO_2 amount in the atmosphere and in the ocean. In 1990 the Intergovernmental Panel on Climate Change predicted the negative consequences of the human made greenhouse effect, like the melting of the glacier, rising sea levels and the melting of the permafrost [5].

Although the effects are well known many countries are still hesitating to tackle them consequently [3]. The main goal of all governments is economic growth to improve the living conditions for their citizens. In general, the economic growth is strongly related with energy demand. In 2016 the primary world energy demand was 13.8 Gtoe (gigatonnes of oil equivalent) with a growing tendency. The energy demand is satisfied by 27.1 % coal, 22.1 % natural gas, 31. 9 % petroleum, 4.9 % nuclear, 9.8 % biofuel and waste, 2.5 % hydro and 1.7 % other fuels [6]. In 2015 the energy sector produced 74 % of the greenhouse gases (GHG). This figures the importance of controlling the global energy related emissions to stabilize the anthropogenic sources of GHG emissions. In the last few years many countries decided to phase out of nuclear energy due to accidents like the one at the Fukushima Daiichi plant in 2011. Furthermore, the European Union plans a coal exit around 2030. A precise date is not yet known. Therefore, new and low-emission technologies are urgently needed [7, 8]. Promising candidates are renewable energies, especially the electrical energy generation from wind and sun. The worldwide growth

of both technologies from 2009 (182 GW) to 2015 (660 GW) is remarkable [7]. The possibilities of the renewable energies are enormous. By far the biggest resource has the sun. The sunlight strikes the earth with more energy per day (10300 EJ [9]) than is currently consumed on the planet per year (576 EJ [10]). The integration of such energy into established infrastructures implicates some challenges in terms of stability, efficiency and reliability, as most renewable sources are intermittent by nature [11, 12]. Therefore, the boost of the renewable energies should be accompanied by the improvement of energy storage systems (EES) [7]. EESs convert energy from one form to another, depending of the storage system. The storage systems can be categorised by response time, storage duration and function [13, 14]. The common method to categories the technologies is by the form of the stored energy [7]. It can be classified in thermochemical, chemical, thermal, electric and mechanical storage systems [15-18]. From 2010 to 2017 the capacity of the EESs increased by 24 % up to 171 GW [7]. The storage technologies are still in their infancy and many new approaches were made in the last decades. A very promising approach seems the utilization of CO_2 as chemical energy storage as well as carbon source for platform chemicals and the further processing to high quality chemical base materials like hydrocarbons. To be sustainable the energy must be provided by renewable energies. Figure 1 shows an elegant solution to utilize CO_2. The idea of the project is related to the principal of the photosynthesis. The photosynthesis converts energy from the sun to chemical energy to dissociate CO_2 to more valuable organic substances [19].

In the plasma induced CO_2 conversion (PiCK) project a plasma process is used to dissociate the CO_2 to oxygen and CO. The energy to operate the plasma process should be delivered by regenerative energy sources in the form of surplus solar or wind energy. Therefore, the process is cost effective and resource saving. To avoid back reaction of CO and oxygen to CO_2, the idea is to separate oxygen by ceramic membranes. The product CO could be used in synthesis processes like the Fischer-Tropsch-Synthesis, by which a liquid chemical storage is possible.
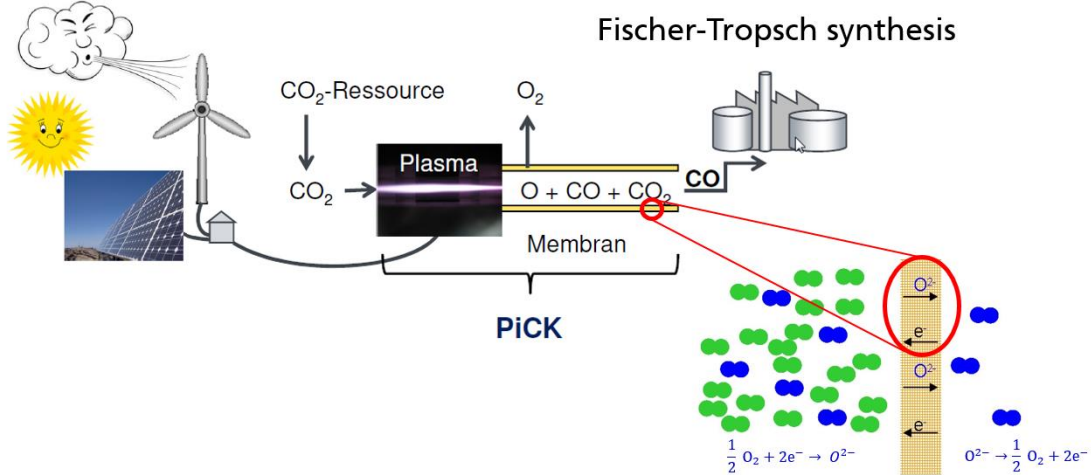
Figure 1: Schematic image of the plasma induced CO_2 conversion (PiCK) mechanism. © IGVP / Fraunhofer IGB

Important for the process is a large dissociation of the CO_2. Therefore, the thermodynamic of the CO_2 splitting needs to be considered [20]. Based on enthalpy and entropy changes of the thermal decomposition of carbon dioxide the temperature T can be calculated according to:

$$G = \Delta H - T\Delta S \qquad [1.1]$$

with ΔH as enthalpy change, ΔS as entropy change, T as temperature and G as Gibbs free energy. If 50 % of the CO_2 molecules dissociated, the physical properties are $\Delta H = 530$ kJ mol^{-1} and $\Delta S = 147$ J mol^{-1}. According to

$$T = \frac{\Delta H}{\Delta S} \qquad [1.2]$$

a temperature of 3600 K results [21, 22]. Thermal decomposition of the CO_2 can only be measured above 2400 K, at 7000 K CO_2 is almost completely dissociated. In the center of a CO_2 microwave torch, temperatures of slightly above 6500 K are present [23, 24]. The calculation of the equilibrium constant K of the thermal decomposition of $CO_2 \rightarrow CO + \frac{1}{2}O_2$, according to

$$\Delta_R G = -RT \ln K \qquad [1.3]$$

results in the CO_2 conversion [%] as a function of temperature [25]. If the system $CO_2 \rightarrow CO + \frac{1}{2}O_2$ were in thermodynamic equilibrium at 1273 K, oxygen would only be present in trace amounts. The advantage of the plasma process compared to the pure thermal splitting of CO_2 is that at relative low temperature a higher amount of oxygen is present [26]. This can be explained by the used plasma technology. For this purpose, an electrode-less microwave excited atmospheric plasma system (APS) is an excellent option due to the high ion, electron and radical densities and the reduced electric field [27-29]. Furthermore, the APS favours the excitation of the asymmetric mode vibrational levels of CO_2 [26, 29]. In addition, the fast cooling (quenching) maintains a higher oxygen partial pressure in the cooled plasma gas compared to the thermodynamic equilibrium value at 1273 K. The condition for this is, on the one hand, rapid kinetics for the thermal decomposition of $CO_2 \rightarrow CO + \frac{1}{2}O_2$ in the plasma and, at the same time, quenching, so that the recombination of $CO + \frac{1}{2}O_2 \rightarrow CO_2$ is hindered. Therefore, a relative high amount of oxygen is present at lower temperature (<1473 K).

Both, the membrane and the separation process, are important for the overall process. They have a high potential to reduce the effort to separate the products. The oxygen partial pressure between the oxygen rich and oxygen lean side is the driving force for the oxygen transport through the membrane [30]. Important for the process is a high selectivity towards oxygen, which cannot be achieved by porous ceramic or polymer membranes, because of the small size difference of the species present in the plasma [31]. On the other hand, a high permeability and a good thermal stability are necessary for the separation process. Therefore, polymeric membranes cannot be used because of a lack in thermal stability.

Promising candidates are the oxygen conductive, dense ceramic membranes with high oxygen permeability and a high selectivity [32-34]. In the past decades oxygen separation membranes were intensively researched for oxygen production as an alternative for the cryogenic air decomposition and for the Oxyfuel process to operate power plants with pure oxygen [35, 36]. Current research uses these membranes for solid oxide fuel cells and for thermochemical conversion of water and CO_2 [37, 38].

For this application ceramics, which crystalize in the cubic structure of the perovskite, are suitable. High performance materials like $Ba_{0.5}Sr_{0.5}Co_{0.8}Fe_{0.2}O_{3-\delta}$ [39] or $BaCo_xFe_yZr_zO_{3-\delta}$ [40] are very promising perovskites for oxygen separation from air. Unfortunately the performance decreases in CO_2 atmosphere due to the formation of carbonates [41]. In this work $(La_{0.6}Ca_{0.4})(Co_{0.8}Fe_{0.2})O_{3-\delta}$ (LCCF) was used due to the good CO_2 stability [42, 43]. The membranes were manufactured as hollow fibers as this geometry has a high specific separation

area [40, 44]. The separation mechanism of dense ceramic membranes differs fundamentally from the mechanism of polymeric membranes and have a higher selectivity towards oxygen. The membranes can be used directly in areas of high temperature due to the separation mechanism, which is based on temperature activated solid diffusion.

1.2. Aim of the work

The focus of this work is the manufacturing and optimization of LCCF hollow fiber membranes. It is part of the PiCK-Project with the overall aim to dissociate CO_2 in a plasma membrane reactor with subsequent separation of the products (CO and oxygen). The requirements for the membranes are very high due to the challenging conditions. Three key requirements are pointed out:

- **Thermal shock resistance:**
  After ignition of the plasma, the temperature not slowly increases like in the conventional permeation cell. The temperature increases in few seconds from room temperature up to 1200 °C at the fiber position. Therefore, the fiber needs to be stable enough to resists this stress.

- **CO_2 stability:**
  Many perovskite materials have the tendency to form carbonates in the presence of CO_2. As the plasma does not convert all the CO_2 to CO and oxygen, a significant amount of CO_2 can be expected in the plasma. Therefore, a good CO_2 stability is needed.

- **Oxygen Permeation:**
  To decrease the amount of fibers in a possible membrane module, the oxygen permeation of each fiber is important. Not only process parameters but also morphological parameters can influence the oxygen permeation.

To satisfy the different requirements, first of all gastight LCCF hollow fiber membranes are manufactured due to the higher surface area compared to other geometries (Chapter 3). Furthermore, the integration of the hollow fiber in the plasma membrane reactor is investigated. Together with the project partners from the IGVP the feasibility of the plasma membrane reactor is examined.

In the following chapter (Chapter 4), the influencing factors of the bulk diffusion are studied via different manufacturing parameters like spinneret, geometry and sintering temperature. The

fifth chapter focuses on further oxygen permeation improvements via two methods. On the on hand, the surface is modified by etching with H_2SO_4 to improve surface exchange reactions via higher surface area. On the other hand, porous hollow fibers with dense layer are developed to improve the surface exchange reactions as well as the bulk diffusion.

Chapter 6 focuses on the project goal: The in situ extraction of oxygen from a CO_2 plasma. Furthermore, different influencing parameters of the CO_2 plasma like temperature, exchange length and the comparability to the conventional permeation mess cell are examined.

Based on the results the potential of the in-situ separation of oxygen and CO from a CO_2 plasma is analysed.

2. State of the art

2.1. Membrane separation technology

In recent decades membrane separation processes have proven to be a promising and attractive field of technological research [45, 46]. In general, membranes can be characterized as a barrier that separates or limits partly or totally the passage of specific components or characteristic species [32]. By means of the definition of membranes they can be classified in various ways, which are shown in Figure 2.
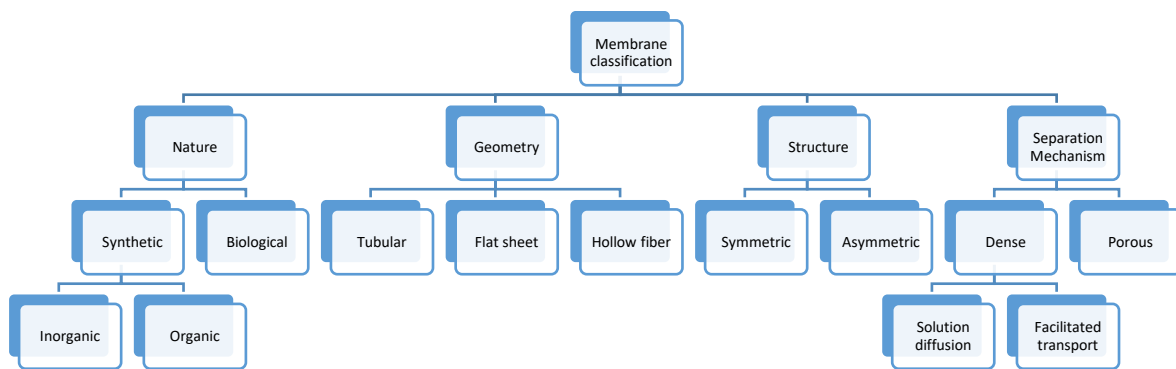
Figure 2: Classification of membranes, derived from [46].

The different classification do not provide the area of application. It represents the variety of membranes [46]. The area of application of membranes is determined by the pore size and the level of selectivity. Depending on the size, a distinction can be made between macropores (> 50 nm), mesopores (2 - 50 nm) and micropores (0.2 - 2 nm). Figure 3 gives an overview of different membrane technologies with corresponding pore sizes and application examples. In today´s separation technology synthetic polymer membranes are most common because of the low cost and the easy handling [46, 47]. They have a wide range of application and can be found in many areas such as medical technology [48, 49] water treatment [50, 51] and gas separation [47, 52].

Figure 3: Field of applications of membranes, derived from [53].
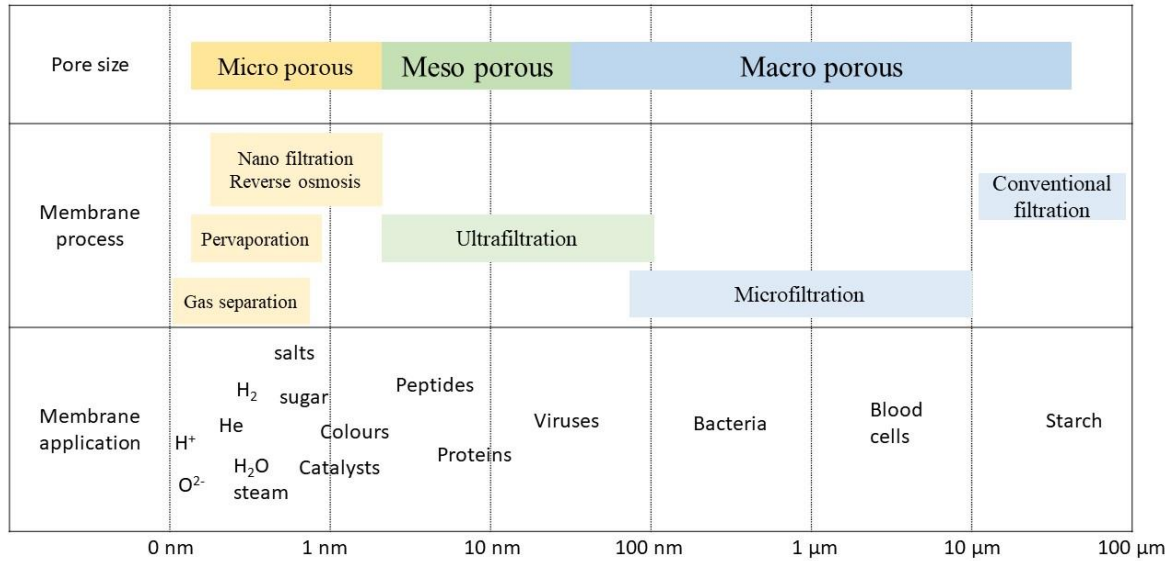
Gas separation through porous membranes is in principle possible using three different mechanisms, which are presented in Figure 4. The fourth mechanism is only possible through dense membranes [46, 54, 55].

If the pore size is bigger than 100 nm the gases permeate the membrane by convective flow (I) and no separation occurs. For pore sizes in the range of 10 - 100 nm the gas permeation is governed by the Knudsen diffusion (II) [46]. The rate of diffusion of different gases (r_1 and r_2) under similar conditions of pressure and temperature are inversely proportional to square root of their molar masses (M_1 and M_2) [56]. This relation is called Graham´s law of diffusion.

$$\frac{r_1}{r_2} = \sqrt{\frac{M_2}{M_1}} \qquad\qquad [2.1]$$

The selectivity of separation due to the Knudsen diffusion is in general relatively low. For example, the separation factor for N_2/O_2 is 1.07 [55]. The actual separation factors are smaller due to the back diffusion, concentration polarisation, non-separative diffusion and the occurrence of viscous flow [55].

With further decrease of the pore size (0.5 - 10 nm) the effect of the molecular sieve (III) occurs [16]. The separation is based on the size exclusion principle. Gases with larger radii than the pore sizes cannot pass, whereas gases with smaller radii can diffuse unhindered through the

pores [46]. The separation factor for the molecular sieve is higher than for the Knudsen diffusion. The factor could be improved for N_2/O_2 up to 30 [57, 58]

The previous described mechanisms (I - III) only occur in porous membranes.

The fourth mechanism, the solution diffusion, occurs in dense membranes [46, 55]. The mechanism is subjected to the Fick´s law and can be divided in three steps. The adsorption on the surface the bulk transport through the membrane and desorption on the opposite surface. Dependent on the structure and the material different diffusion processes can occur. Typical for solution diffusion are dense polymeric membranes or mixed matrix membranes. The big advantage compared to other technology like adsorption and cryogenic distillation is the easy handling and the low energy cost [59].

However, in some processes the conditions are unfavourable for polymer membranes [32, 60]. Such conditions are for example very high temperatures or acidic environment. For these conditions ceramic membranes are a good alternative. While ceramic membranes with pore sizes above one nm are already commercially available and used in some areas, gas separation membranes with pore sizes below 0.4 nm and dense membranes are still in the development stage [46, 53, 61].
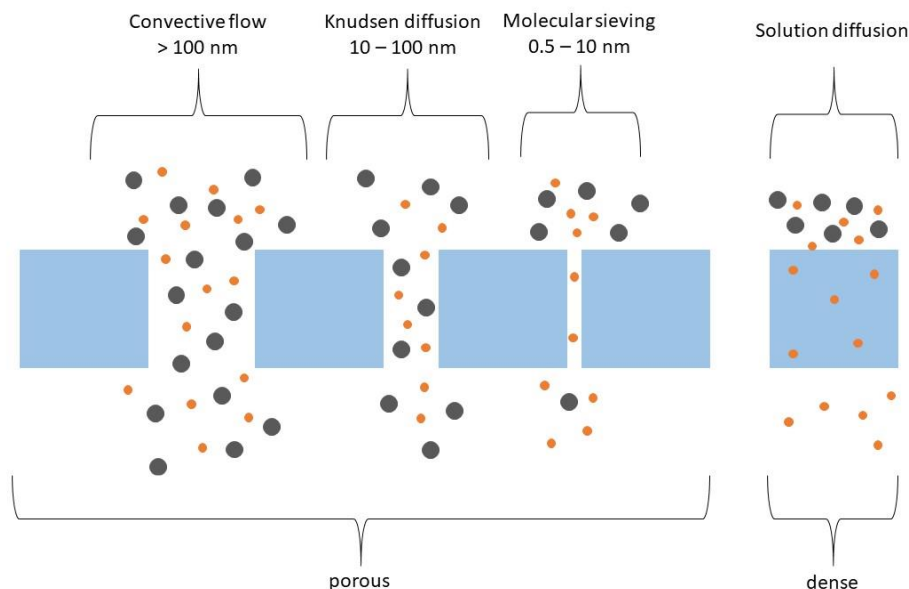

Figure 4: Gas separation mechanism: (I) Convective flow, (II) Knudsen diffusion, (III) Molecular sieving, (IV) Solution diffusion, derived from [55].

2.2. Dense ceramic structures for oxygen permeation

A Ceramic is defined as a non-metallic, inorganic solid whose structure consists of polycrystalline areas [62, 63]. The symmetry of the crystal lattice shows the bonding nature of the individual atoms. Big differences occur in the physical and chemical properties of ceramics, depending on whether ionic, covalent or metallic bonds dominate in the material. In oxide ceramics mainly ionic bonds are present. The major structures can be classified in six groups:

- Brownmillerite-type (general formula $A_2B_2O_5$) [64]

- Fluorite-type (general formula AO_2) [65]

- Cubic perovskite-type (general formula ABO_3) [66]

- Pyrochlore-type (general formula $A_2B_2O_7$) [67]

- Double perovskite type (general formula $A_2B_2O_6$) [68]

- K_2NiF_4-type (general formula K_2NiF_4) [69]

Among these oxide ceramic systems, cubic perovskites-type structures attracted attention in the field of gas separation [32, 66].

2.2.1. Perovskite

Perovskites can be associated to the field of technical ceramics [63]. The magnetic properties vary between ferromagnetic, antiferro- and paramagnetic, while the electrical properties of conductive materials reach from semiconductors to insulators [70]. Therefore, perovskite materials have a broad operational area such as in microelectronics or mechatronics.

The crystal structure of perovskites derives from the mineral $CaTiO_3$ [71-73]. The spatial arrangement of perovskites oxides follows the empirical formula ABO_3. Positions A and B are occupied by cations. Alkali and alkaline earth elements are usually implemented in the A position which are the larger cations. Transition metals with smaller ionic radii are preferably incorporated in the B position. The A cations are cubically surrounded by the B cations, which in turn are octahedral coordinated by six oxygen ions. A schematic representation of the ideal crystal structure of perovskites is shown in Figure 5.
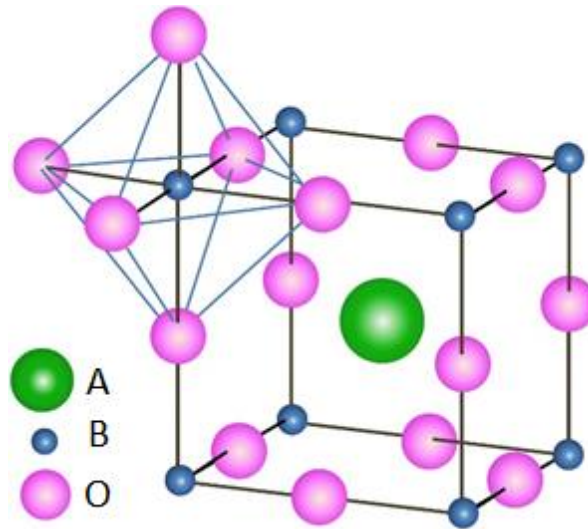
Figure 5: Ideal cubic perovskite structure, derived from [74].

The stability of the perovskite crystal structure is determined by the relative atomic size of the A- and B-cations and by the electric configuration of the B-cations [33, 75]. It can be described by the so-called Goldschmidt´s tolerance factor [76]:

$$t_G = \frac{1}{\sqrt{2}} \cdot \frac{r_A + r_O}{r_B + r_O}$$

[2.2]

r_A	atomic radii of the A-site cations
r_B	atomic radii of the B-site cations
r_O	atomic radii of the oxygen ion
t_G	tolerance factor

For perovskites, the tolerance factor is in the range between 0.8 and 1.0. If the tolerance factor is outside the range distortion of the lattice and different structures can occur.

An ideal perovskite structure, as shown in Figure 5, is not conductive for oxygen ions. Therefore, defects in the crystal structures are necessary. Depending on the dimension of the defects, they can be divided into four categories: Point defects (zero dimensional), line defects (one dimensional), planar defects (two dimensional) and bulk defects (three dimensional).

In general, three point defects occur in perovskites: Vacancies, interstitials and substitutions. Vacancies are lattice positions, which are not occupied in the ideal crystal. Interstitial defects occur if atoms (or ions) occupy irregular or not ordinarily places in the lattice structure. Substitutions are replaced atoms (or ions) by other atoms (or ions) and can lead to distortion of the lattice.

Vacancies appear in combination with other defects. The most common defects involving vacancies are the Schottky and Frenkel defects [77-79]. The Schottky defect is defined as an ion that has been substituted by the vacancy on the surface of the crystal. In contrast, the Frenkel defect is described as an ion, which is located in an interstitial space. Both defects are shown in Figure 6 and are always present in any crystal at a finite temperature in equilibrium. This can be explained with the Gibbs-Helmholtz equation [77].

$$G = H - T \cdot S \qquad\qquad [2.3]$$

with G as Gibbs-free energy, H as enthalpy, T as temperature and S as entropy.
With increasing amount of defects the enthalpy increases but it causes disorder. Increasing disorder leads to an increase of the entropy. At a sufficiently high temperature, the entropy dominates the formation of vacancies because the enthalpy can be more than compensated by the decrease of $-TS$.
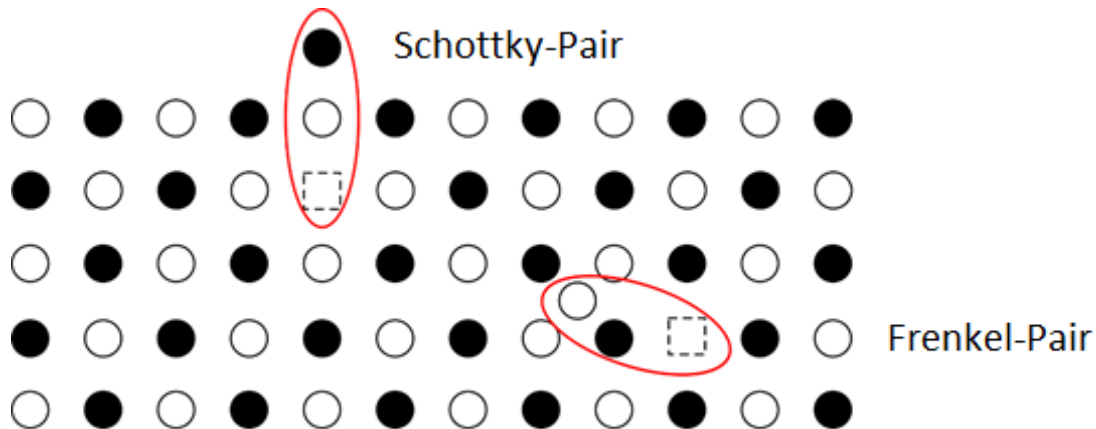
Figure 6: Schottky defect and Frenkel defect in an ionic crystal, derived from [80].

In perovskites the amount of oxygen vacancies have a significant impact on the oxygen permeation [81, 82]. Therefore, materials are selected which are doped with low valence B-cations. With an increase of the temperature the oxidation state of the B-cations changes and leads to an unbalance of the charge. This in turn, leads to a removal of oxygen atoms from the lattice to rebalance the charge. This results in the following equation:

$$ABO_3 \ \rightarrow \ ABO_{3-\delta} + \frac{\delta}{2}O_2 \qquad\qquad [2.4]$$

with δ as the amount of oxygen ion vacancies.

Larger amounts of ion vacancies lead to a better transport of ions through the crystal lattice, which results in a higher ionic conductivity. But if the critical oxygen vacancy concentration is reached, the crystal lattice can be transformed. This leads to a reduction of the ionic conductivity [83].

By doping the A-cation side as well as the B-cation side many different perovskite materials can be obtained for different applications [84-86]. The resulting structure is $A_xA'_{1-x}B_yB'_{1-y}O_{3-\delta}$. The ions are selected depending on which structural properties are desired. In mixed ionic and electronic conductor (MIEC) perovskites the defects provide a pathway for oxygen ionic diffusion and the transition metals (B-cations) contribute to the electronic conductivity [80, 87, 88]. This is possible due to the different oxidation states of the transition metals. The transport mechanism of MIEC perovskites will be discussed in detail in the following chapter.

2.3. Oxygen transport mechanism in MIEC membranes

The characteristic of a mixed ionic electronic conductor is the ability to transport not only electrons but also ions through the bulk [32, 80, 87, 89]. As already mentioned in chapter 2.2.1, oxygen ions can diffuse through lattice vacancies. The formation of lattice vacancies at higher temperatures ($> 700°C$) is accompanied by electron transfer, which is formed by the reduction of the transition metals. The driving force of the oxygen transport is a potential difference between the feed side (μ_1) and the permeate side (μ_2), which can be triggered by different partial pressures. The oxygen transport occurs in five steps, which are shown schematically in Figure 7.

(1) First, oxygen molecules diffuse to the membrane surface and adsorb. This results in a concentration decrease at the boundary layer of the feed side (concentration polarization on the feed side). (2) Dissociation and reduction of the oxygen molecules according to the following reaction equation:

$$O_2(g) + 4\,e^- \rightarrow 2\,O^{2-} \tag{2.5}$$

The oxygen atoms are reduced to two O^{2-} ions by consumption of four electrons. Then the oxygen ions are incorporated into the perovskite crystal lattice. This process is called surface exchange reaction on the feed side. (3) After incorporation, the oxygen ions diffuse via vacancies through the crystal lattice to the permeate side. At the same time, electrons are transported to the feed side. This process is known as bulk diffusion. (4) After the removal of

the oxygen ions from the crystal lattice, two oxygen ions recombine by giving up electrons to form an oxygen molecule according to:

$$2\,O^{2-} \rightarrow O_2(g) + 4\,e^-$$

[2.6]

This reaction corresponds to the surface exchange reaction on the permeate side. (5) After recombination, desorption and diffusion of the oxygen molecule away from the boundary layer a concentration gradient occurs.
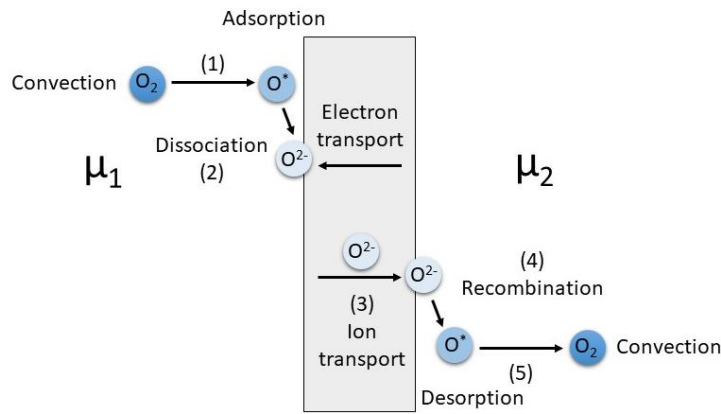

Figure 7: Oxygen transport mechanism through MIEC membrane, derived from [90].

In general, the transition resistance between the membrane and the gas phase are small and negligible [80, 91]. Therefore, only the bulk diffusion and the surface exchange reaction need to be considered for developing transport mechanism. The mechanism of the bulk diffusion as well as the surface exchange reaction will be discussed in the following chapters.

2.3.1. Bulk diffusion

Wagner´s transport theory in metal oxide layers can be used to describe the oxygen transport through the bulk [80, 91, 92]. As already mentioned, the oxygen transport proceeds in the form of ions under a counter flow of electrons. As a result, the oxygen permeation is dependent on the electronic conductivity σ_{el} and the ionic conductivity σ_{ion}. Furthermore, the oxygen permeation depends on the gradient of the oxygen potential $\nabla\mu_{O2}$, whereby the following correlation applies:

$$J_{O2} \propto -\frac{\sigma_{el}\,\sigma_{ion}}{\sigma_{el} + \sigma_{ion}}\,\nabla\mu_{O2}$$

[2.7]

The electronic conductivity (σ_{el}) is usually considerably larger than the ionic conductivity (σ_{ion}) because the mobility of electronic carriers is greater than the one of ionic carriers in MIEC membranes ($\sigma_{el} \gg \sigma_{ion}$). Therefore, the following simplification can be made:

$$\frac{\sigma_{el}\,\sigma_{ion}}{\sigma_{el} + \sigma_{ion}} \approx \sigma_{ion} \qquad\qquad [2.8]$$

with the following assumptions [32, 90]:
- The dissociation and recombination of the oxygen molecules are in equilibrium
- The surface exchange reactions of the oxygen ions for incorporation and removal are in equilibrium
- No influence between the electronic and ionic flow and the membrane is electrically neutral to the outside
- The gradient of the oxygen potential $\nabla\mu_{O2}$ can be described by the gradient of oxygen partial pressure ratio
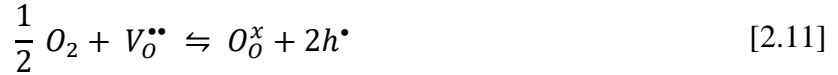- The ionic conductivity is constant along the membrane thickness

The Wagner equation can be written as:

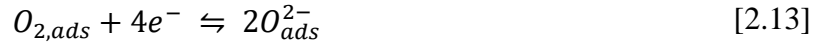$$J_{O2} = -\frac{R\,T\,\sigma_{ion}}{4^2\,F^2\,d}\,ln\frac{p_1}{p_2} \qquad\qquad [2.9]$$

with J_{O2} as the oxygen permeation, R as the gas constant, F as the Faraday constant, d as the membrane thickness, T as the temperature, σ_{ion} as the ionic conductivity at standard conditions, p_1 and p_2 as the oxygen partial pressure at the high pressure side and the low pressure side.

2.3.2. Surface exchange reaction

As already mentioned, it is necessary to dissociate the oxygen molecules at the surface to incorporate the oxygen ions into the crystal lattice [91]. The oxygen transfer from the gas phase to the oxygen vacancies can be described with the Kröger-Vink-Notation [93].

$$\frac{1}{2} O_2 + V_O^{\bullet\bullet} + 2e^- \leftrightharpoons O_O^x \qquad\qquad [2.10]$$

$$\frac{1}{2} O_2 + V_O^{\bullet\bullet} \leftrightharpoons O_O^x + 2h^\bullet \qquad\qquad [2.11]$$

with $V_O^{\bullet\bullet}$ as oxygen vacancy site, O_O^x as oxygen inside the crystal lattice and $h^\bullet$ as electron hole. For a more detailed description of the exchange mechanism between the surface and the bulk the following equilibrium relations were formulated:

$$O_{2,(g)} \leftrightharpoons O_{2,ads} \qquad\qquad [2.12]$$

$$O_{2,ads} + 4e^- \leftrightharpoons 2O_{ads}^{2-} \qquad\qquad [2.13]$$

$$O_{ads}^{2-} + V_O^{\bullet\bullet} \leftrightharpoons O_O^x + 2h^\bullet \qquad\qquad [2.14]$$

Equation [2.12] describes the adsorption of molecular oxygen at the membrane surface. Equation [2.13] expresses the dissociation of the oxygen molecule and equation [2.14] represents the incorporation of the oxygen ion into the crystal lattice.

Considering near-equilibrium conditions, the oxygen flux through the gas/perovskite interface is given by the Onsager equation [94]:

$$J_{O2} = -j_{ex}^0 \frac{\Delta\mu_{O2}'}{RT} = -j_{ex}^0 \frac{\Delta\mu_{O2}''}{RT} \qquad\qquad [2.15]$$

with $\Delta\mu_{O2}'$ and $\Delta\mu_{O2}''$ as the driving force across the two interfacial zones of the membrane and j_{ex}^0 as surface exchange rate of oxygen at equilibrium.

2.3.3. Rate-determining step in oxygen transport

The different transport mechanisms at the surface and through the bulk operate in series. The overall rate of oxygen transport is determined by the slowest step. The rate-determining step can be influenced by different parameters:

- Physical and chemical properties (ionic and electronic conductivity, diffusion and surface exchange coefficients, microstructure or morphology)
- Experimental conditions (oxygen partial pressure, temperature)

The microstructure is a big influencing factor for the oxygen transport. In the literature a controversial exists regarding the grain boundaries in the microstructure [32, 95-98]. On the one hand, the investigation of Diethelm et al. [99] regarding $La_{0.5}Sr_{0.5}FeO_{3-\delta}$ shows that an increase of the grain size leads to an decrease of the permeation. This indicates that the grain boundaries act as fast diffusion paths for oxygen ions. On the other hand, Zeng et al. [100] investigated for $La_{0.6}Sr_{0.4}Co_{0.2}Fe_{0.8}O_{3-\delta}$ the opposite effect. Therefore, grain boundaries can act as fast diffusion paths or as diffusion barrier. This in turn can influence the bulk diffusion as well as the surface exchange reactions.

To estimate the rate determining step Bouwmeester et al. [84] defined a so called "critical thickness" L_c [84, 90]. Figure 8 shows the dependency of the oxygen permeation from the critical thickness. In the first section, when the wall thickness is larger than the critical thickness $(d > L_c)$, the oxygen permeation is governed by the bulk diffusion. In the second section, the so called mixed regime, the bulk diffusion as well as the surface exchange reactions have a significant influence to the oxygen permeation. In this section, the wall thickness is close to the critical thickness. In the third section, when the wall thickness is smaller than the critical thickness, the surface exchange reactions governs the oxygen permeation.
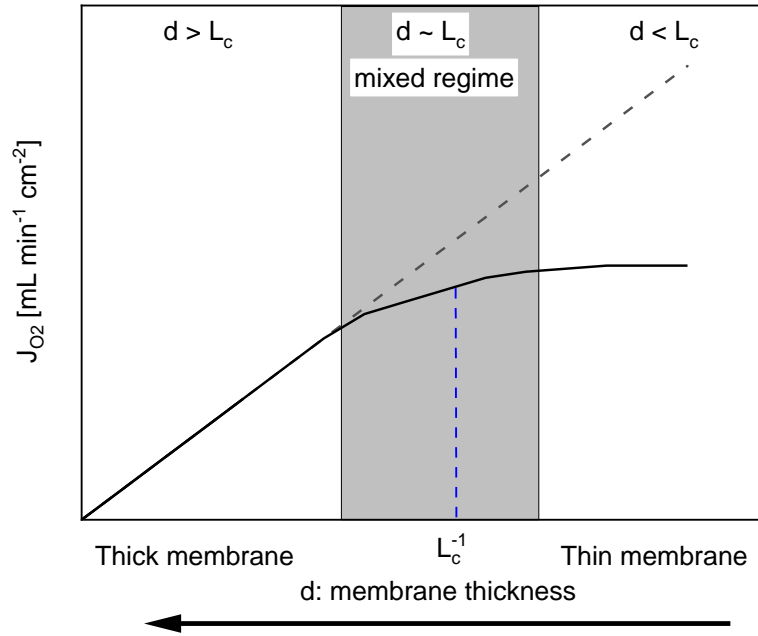
Figure 8: Rate determining step for oxygen transport through the membrane in relation to the characteristic thickness, derived from [90].

By assuming that the electronic conductivity is much higher than the ionic conductivity, the dominating transport mechanism for hollow fibers can be calculated by the modified Wagner equation [30]:

$$J_{O2} = \frac{\sigma_i^0 RT}{16F^2\, n\, d}(p_1^n - p_2^n) \qquad [2.16]$$

with p_1^n and p_2^n as the oxygen partial pressure at the high pressure side and the low pressure side and n as the fitting parameter, which can be derived from experimental data.

With the value of n, the rate-limiting step of oxygen transport can be estimated. For $n < 0$, bulk diffusion is rate limiting; for $n \geq 0.5$, the surface exchange reactions dominates the oxygen flux and for $0 < n < 0.5$, the oxygen permeation is influenced by a mixed regime.

Whenever the oxygen permeation is governed by surface exchange reactions or bulk diffusion, this equation can model the oxygen permeation flux dependence of the oxygen partial pressure. In the literature different models, besides the Wagner equation, were investigated to describe the oxygen permeation flux through a membrane with partial or complete limitation through surface exchange kinetics. Since these models are not used in this work, appropriate literature is referred [80, 89, 90, 101].

2.4. Basic aspects of hollow fiber membrane manufacturing

2.4.1. Non-solvent induced phase separation

The first publication regarding the phase inversion process was published by Loeb et al. in 1963 [102]. Since then, the phase inversion process has been the most often used technology to produce porous flat and hollow fiber membranes.

The phase inversion refers to the transformation of a thermodynamic stable liquid to a solid state [31, 103, 104]. The phase separation can be induced by temperature change or by contact with a non-solvent. In the following the non-solvent induced phase separation (NIPS) process will be discussed in detail. A precondition for the NIPS process is a polymer with a good solubility in an organic solvent but insoluble in another liquid (non-solvent). The NIPS process can be described by the ternary phase diagram according to Gibbs (Figure 9).

The corner points of the diagram represent the pure components of polymer, solvent and non-solvent. The diagram is separated into two regions, the one phase and the two phase region, by the binodal boundary. In the one phase region, all components are soluble and a homogeneous phase is present. In the two phase region a miscibility gap indicates the phase separation.
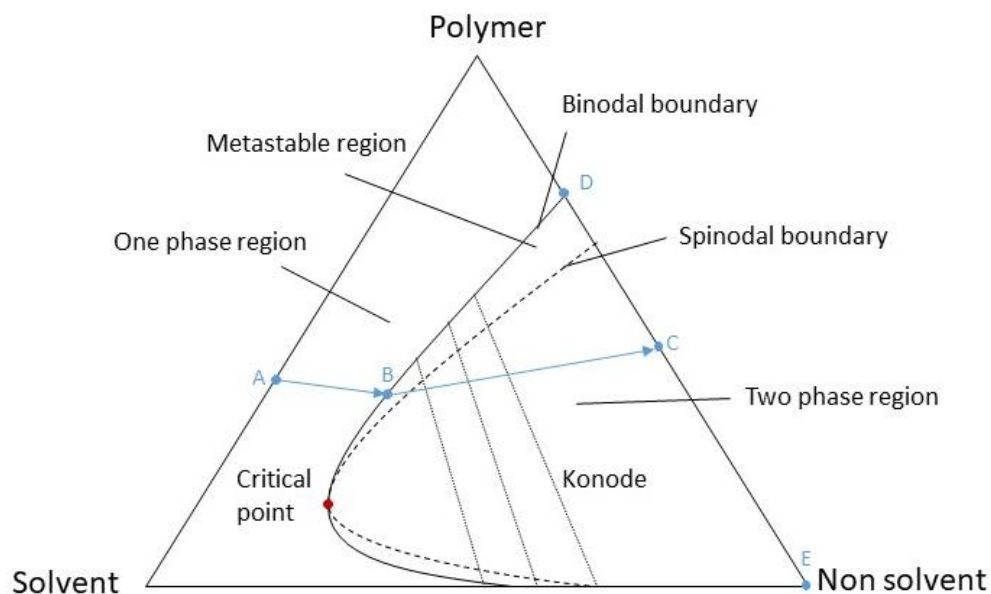

Figure 9: Ternary phase diagram with the course of the phase inversion process, derived from [103]

In Figure 9 the course of precipitation is shown by means of the blue line. Point A represents a homogeneous polymer solution. Through contact with the non-solvent the exchange of solvent and non-solvent starts until the binodal boundary is reached (B). After crossing the binodal

boundary the polymer solution precipitates along the konode. A solid polymer rich and a liquid polymer lean phase is formed. The precipitation continues until the non-solvent almost completely exchanged the solvent (C) which results in two separate phases. The polymer rich (D) and the polymer lean (E) phase.

The morphology of the membrane is strongly dependent on the thermodynamic of the system [103]. The crossing to the miscibility gap can lead to different precipitation and therefore to different morphologies. If the pathway runs mainly through the metastable region, nucleation and growth dominate the membrane structure. This is called binodal demixing. If the pathway leads nearly direct into the two phase region the so-called spinodal decomposition takes place. This results in the formation of an open-celled polymer structure.

Furthermore other factors can influence the morphology like [31, 105]:

- Solvent
- Non-solvent
- Precipitation of the polymer
- Polymer material
- Viscosity
- Diffusion
- Kinetic effects
- Composition of the polymer solution
- Composition of the precipitation bath
- Temperature of the polymer solution and the precipitation bath.

With the NIPS process hollow fiber membranes can be manufactured in different geometries and wall thicknesses by using different spinnerets. As already mentioned the hollow fiber geometry is favoured due to the higher specific surface and the lower material consumption compared to other geometries [106].

The NIPS process can also be adapted for ceramic membranes [40, 95]. For this purpose, ceramic particles are dispersed in the spinning solution. When the polymer precipitates, the particles are embedded in the polymer matrix, and a flexible green fiber is obtained.

2.4.2. Sintering mechanism

The term sintering describes the solidification and continuous densification of a powder or a porous body by thermal treatment [107, 108]. This process can be divided into five different categories: liquid phase sintering, reactive sintering, viscous sintering, vitrification and solid state sintering. The endeavour of a system is to reach the state of the lowest free enthalpy. The driving force to reach the lowest free enthalpy includes the reduction of the surface free energy, chemical reactions of different components and pressure.

In this work, the MIEC membranes were manufactured by the solid state sintering. For this process, high temperatures are necessary to enable the material transport. In the literature [108] a relation between the sintering temperature T_{sint} and the melting temperature T_s for oxidic materials exists:

$$T_{sint} \approx 0.8\, T_s \qquad\qquad [2.17]$$

This relation can only be used as a rough orientation, since the sintering activity is strongly related to the properties of the material, like particle size. If the sintering temperature can be reached, different sintering mechanisms can occur: vapour transport, surface diffusion, lattice diffusion, grain boundary diffusion and dislocation motion. A distinction is made between densifying and non-densifying mechanisms. Figure 10 shows the different sintering mechanisms by the example of a two particle system.

The different mechanisms do not operate independently [109]. The mechanisms 1 - 3 lead to coarsening of the particle with first neck growth and without densification. These can lead to a significant reduction in the densification rate. Mechanism 4 and 5 are the most important densifying mechanisms. Diffusion from the grain boundaries to the pores support the neck growth and the shrinkage. The plastic flow by dislocation motion can also cause neck growth and densification through deformation of the particles. Depending on the dominating mechanism (coarsening or densification), the sintering result can be modified to porous or dense membranes.

Non-densifying mechanisms:
1. Vapour transport
2. Surface diffusion
3. Lattice diffusion (from the surface)

Densifying mechanisms:
4. Grain boundary diffusion
5. Lattice diffusion (from the grain boundary)
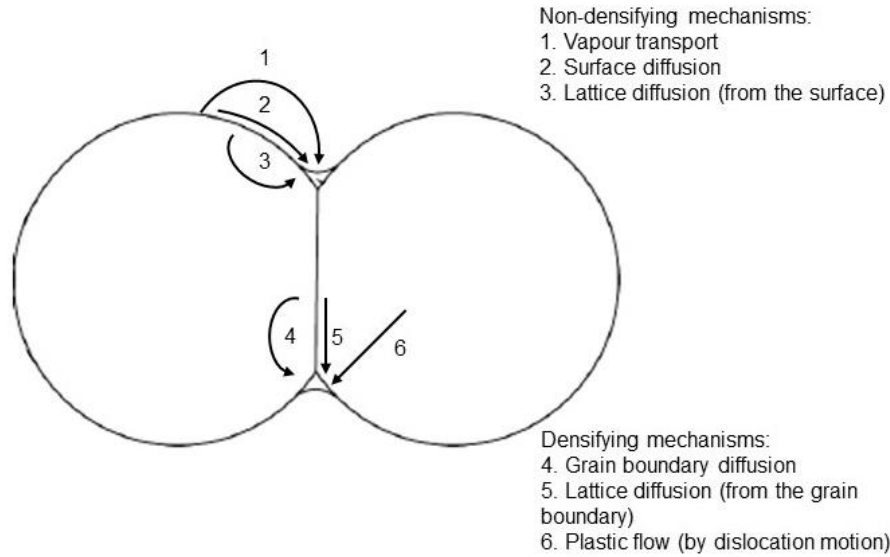6. Plastic flow (by dislocation motion)

Figure 10: Schematic representation of the sintering mechanisms for a system of two particles, derived from [109].

The densification and growth process can be expressed by the following equation [107]:

$$\frac{x}{r} = \left(\frac{40 \cdot \gamma \cdot a^3 \cdot D^*}{k \cdot T}\right)^{\frac{1}{5}} \cdot r^{-\frac{3}{5}} \cdot t^{\frac{1}{5}} \qquad [2.18]$$

with x as radius of the contact area between the grains (height of the sinter neck), r as the grain radius, γ as surface energy, a^3 as atomic volume und D^* as self-diffusion coefficient, t as time, T as temperature and k as Boltzmann constant.

Equation [2.18] indicates a decrease of the growth rate by an increase of the grain size and passing time. Furthermore, a volume change can be seen with increasing densification, which in turn leads to a shrinkage of the sinter. The shrinkage behaviour of the sinter material is well known and can be classified in three stages [32, 108, 110]:

Stage 1:   Initial stage

During this stage transition of the microstructure occur, whereby new grain boundaries are formed. Furthermore, the densification is accompanied by neck growth and the large initial differences in surface curvature are removed. There is no obvious change in volume, density or grain size. If the goal of the sintering process is to reach high density, the temperature should be increased quickly because the coarsening reduce the driving force of the densification.

Stage 2:   Intermediate Stage

With further increase of the temperature the distance between the grains decreases and the sintering necks become larger. Furthermore, a pore network is formed throughout the body by a decreasing amount of open pores so that only isolated pores are left. As a result, the volume decreases accompanied by the increase of density. The intermediate stage ends when the theoretical density reaches 90 %.

Stage 3:   Final stage

In the final stage the isolated pores shrink continuously and may disappear altogether. Furthermore, some of the grains grow at the expense of other grains, what results in a coarse grained system. A theoretical density of 95 - 98 % can be reached.

In the literature many different heating schedules were published in consideration of the different stages and for different porosities [109]. Figure 11 shows a general heating schedule with different temperature stages.

On the first stage the remaining solvent and volatile components are removed. During the second stage the thermal decomposition of organic components takes place. At the third stage, the highest temperature stage, the different transport mechanisms ensure the sintering process, the characteristic microstructure and the desired densification. The fourth stage, the cool down, is included to relieve internal stresses.
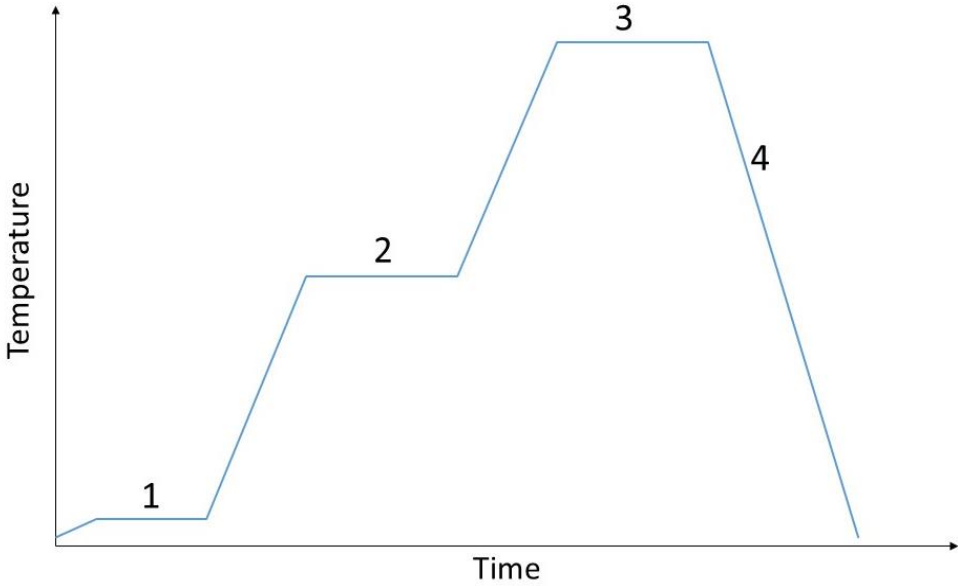
Figure 11: Generalized heating schedule, derived from [109].

2.5. References

[1] S. Dyatlov, N. Didenko, E. Ivanova, E. Soshneva, S. Kulik, Prospects for alternative energy sources in global energy sector, in: IOP Conference Series: Earth and Environmental Science, IOP Publishing, 2020, 012014.

[2] A. Grubler, C. Wilson, N. Bento, B. Boza-Kiss, V. Krey, D.L. McCollum, N.D. Rao, K. Riahi, J. Rogelj, S. De Stercke, A low energy demand scenario for meeting the 1.5°C target and sustainable development goals without negative emission technologies, Nature energy, 3 (2018) 515-527.

[3] IEA, CO2 Emissions from Fuel Combustion: Overview, IEA, (2020) https://www.iea.org/reports/co2-emissions-from-fuel-combustion-overview.

[4] P. Friedlingstein, M.W. Jones, M. O'sullivan, R.M. Andrew, J. Hauck, G.P. Peters, W. Peters, J. Pongratz, S. Sitch, C.L. Quéré, Global carbon budget 2019, Earth System Science Data, 11 (2019) 1783-1838.

[5] I.P.O.C. Change, Climate change: The IPCC scientific assessment, Mass, Cambridge, (1990).

[6] M.M. Tumbaz, M. Ipek, Energy Demand Forecasting: Avoiding Multi-collinearity, Arabian Journal for Science and Engineering, 46 (2021) 1663-1675.

[7] M.M. Rahman, A.O. Oni, E. Gemechu, A. Kumar, Assessment of energy storage technologies: A review, Energy Conversion and Management, 223 (2020) 113295.

[8] R. Vakulchuk, I. Overland, D. Scholten, Renewable energy and geopolitics: A review, Renewable and Sustainable Energy Reviews, 122 (2020) 109547.

[9] N.S. Lewis, D.G. Nocera, Powering the planet: Chemical challenges in solar energy utilization, Proceedings of the National Academy of Sciences, 103 (2006) 15729-15735.

[10] IEA, Key Wolrd Energy Statistics 2020, (2020).

[11] M. Bajaj, A.K. Singh, Grid integrated renewable DG systems: A review of power quality challenges and state-of-the-art mitigation techniques, International Journal of Energy Research, 44 (2020) 26-69.

[12] S.R. Sinsel, R.L. Riemke, V.H. Hoffmann, Challenges and solution technologies for the integration of variable renewable energy sources- A review, Renewable Energy, 145 (2020) 2271-2285.

[13] H. Chen, T.N. Cong, W. Yang, C. Tan, Y. Li, Y. Ding, Progress in electrical energy storage system: A critical review, Progress in Natural Science, 19 (2009) 291-312.

[14] M.G. Molina, Dynamic modelling and control design of advanced energy storage for power system applications, Dynamic Modelling, (2010) 300.

[15] X. Luo, J. Wang, M. Dooner, J. Clarke, Overview of current development in electrical energy storage technologies and the application potential in power system operation, Applied Energy, 137 (2015) 511-536.

[16] H. Zhao, Q. Wu, S. Hu, H. Xu, C.N. Rasmussen, Review of energy storage system for wind power integration support, Applied Energy, 137 (2015) 545-553.

[17] A. Evans, V. Strezov, T.J. Evans, Assessment of utility energy storage options for increased renewable energy penetration, Renewable and Sustainable Energy Reviews, 16 (2012) 4141-4147.

[18] G. Li, Y. Hwang, R. Radermacher, H.-H. Chun, Review of cold storage materials for subzero applications, Energy, 51 (2013) 1-17.

[19] E.I. Rabinowitch, Photosynthesis and related processes, LWW, 1951.

[20] D.R. Lide, CRC handbook of chemistry and physics, CRC Press, 2004.

[21] H.S. Kwak, H.S. Uhm, Y.C. Hong, E.H. Choi, Disintegration of carbon dioxide molecules in a microwave plasma torch, Scientific Reports, 5 (2015) 1-13.

[22] S.M. Chun, D.H. Shin, S.H. Ma, G.W. Yang, Y.C. Hong, CO_2 microwave plasma—catalytic reactor for efficient reforming of methane to syngas, Catalysts, 9 (2019) 292.

[23] B.O. Ogungbesan, R. Kumar, M. Sassi, Optical Characterization of a Microwave Plasma Torch for Hydrogen Production, International Journal of Industrial and Manufacturing Engineering, 6 (2012) 2543-2549.

[24] K.M. Green, M.C. Borras, P.P. Woskov, G.J. Flores, K. Hadidi, P. Thomas, Electronic excitation temperature profiles in an air microwave plasma torch, IEEE transactions on Plasma Science, 29 (2001) 399-406.

[25] R. Snoeckx, A. Bogaerts, Plasma technology- A novel solution for CO_2 conversion?, Chemical Society Reviews, 46 (2017) 5805-5863.

[26] A. Bogaerts, T. Kozák, K. Van Laer, R. Snoeckx, Plasma-based conversion of CO_2: Current status and future challenges, Faraday Discussions, 183 (2015) 217-232.

[27] M. Leins, K.M. Baumgärtner, M. Walker, A. Schulz, U. Schumacher, U. Stroth, Studies on a Microwave-Heated Atmospheric Plasma Torch, Plasma Processes and Polymers, 4 (2007) S493-S497.

[28] C. Tendero, C. Tixier, P. Tristant, J. Desmaison, P. Leprince, Atmospheric pressure plasmas: A review, Spectrochimica Acta Part B: Atomic Spectroscopy, 61 (2006) 2-30.

[29] V. Rusanov, A. Fridman, G. Sholin, The physics of a chemically active plasma with nonequilibrium vibrational excitation of molecules, Soviet Physics Uspekhi, 24 (1981) 447.

[30] H.J. Bouwmeester, A.J. Burggraaf, Dense ceramic membranes for oxygen separation, Membrane Science and Technology, Elsevier, 1996, 435-528.

[31] M. Mulder, J. Mulder, Basic principles of membrane technology, Springer Science & Business Media, 1996.

[32] X. Zhu, W. Yang, Mixed conducting ceramic membranes, Green Chemistry and Sustainable Technology, (2017).

[33] D.D. Athayde, D.F. Souza, A.M. Silva, D. Vasconcelos, E.H. Nunes, J.C.D. da Costa, W.L. Vasconcelos, Review of perovskite ceramic synthesis and membrane preparation methods, Ceramics International, 42 (2016) 6555-6571.

[34] C. Zhang, J. Sunarso, S. Liu, Designing CO_2-resistant oxygen-selective mixed ionic–electronic conducting membranes: Guidelines, recent advances, and forward directions, Chemical Society Reviews, 46 (2017) 2941-3005.

[35] E. Pfaff, M. Zwick, Oxyfuel combustion using perovskite membranes, Mechanical Properities and Performance of Engineering Ceramics and Composites III, Ceramic Engineering and Science Proceedings, 28 (2007) 23-31.

[36] H. Stadler, F. Beggel, M. Habermehl, B. Persigehl, R. Kneer, M. Modigell, P. Jeschke, Oxyfuel coal combustion by efficient integration of oxygen transport membranes, International Journal of Greenhouse Gas Control, 5 (2011) 7-15.

[37] W. Liang, Z. Cao, G. He, J.r. Caro, H. Jiang, Oxygen transport membrane for thermochemical conversion of water and carbon dioxide into synthesis gas, ACS Sustainable Chemistry & Engineering, 5 (2017) 8657-8662.

[38] D. Cui, Y. Ji, C. Chang, Z. Wang, X. Xiao, Influence of fuel flow rate on the performance of micro tubular solid oxide fuel cell, International Journal of Hydrogen Energy, 45 (2020) 13459-13468.

[39] S. Baumann, F. Schulze-Küppers, S. Roitsch, M. Betz, M. Zwick, E. Pfaff, W. Meulenberg, J. Mayer, D. Stöver, Influence of sintering conditions on microstructure and oxygen permeation of $Ba_{0.5}Sr_{0.5}Co_{0.8}Fe_{0.2}O_{3-\delta}$ (BSCF) oxygen transport membranes, Journal of Membrane Science, 359 (2010) 102-109.

[40] T. Schiestel, M. Kilgus, S. Peter, K. Caspary, H. Wang, J. Caro, Hollow fibre perovskite membranes for oxygen separation, Journal of Membrane Science, 258 (2005) 1-4.

[41] O. Czuprat, M. Arnold, S. Schirrmeister, T. Schiestel, J. Caro, Influence of CO_2 on the oxygen permeation performance of perovskite-type $BaCo_xFe_yZr_zO_{3-\delta}$ hollow fiber membranes, Journal of Membrane Science, 364 (2010) 132-137.

[42] K. Efimov, T. Klande, N. Juditzki, A. Feldhoff, Ca-containing CO_2-tolerant perovskite materials for oxygen separation, Journal of Membrane Science, 389 (2012) 205-215.

[43] G. Chen, W. Liu, M. Widenmeyer, P. Ying, M. Dou, W. Xie, C. Bubeck, L. Wang, M. Fyta, A. Feldhoff, High flux and CO_2-resistance of $La_{0.6}Ca_{0.4}Co_{1-x}Fe_xO_{3-\delta}$ oxygen-transporting membranes, Journal of Membrane Science, 590 (2019) 117082.

[44] S. Liu, G.R. Gavalas, Oxygen selective ceramic hollow fiber membranes, Journal of Membrane Science, 246 (2005) 103-108.

[45] M.K. Purkait, R. Singh, Membrane technology in separation science, CRC Press, 2018.

[46] R.W. Baker, Membrane technology and applications, John Wiley & Sons, 2012.

[47] H.W. Rösler, Membrantechnolgie in der Prozessindustrie–Polymere Membranwerkstoffe, Chemie Ingenieur Technik, 77 (2005) 487-503.

[48] M. Sun, K. Han, R. Hu, D. Liu, W. Fu, W. Liu, Advances in Micro/Nanoporous Membranes for Biomedical Engineering, Advanced Healthcare Materials, 10 (2021) 2001545.

[49] T. Wei, L. Gu, M. Zhou, Y. Zhou, H. Yang, M. Li, Impact of Shock-Induced Cavitation Bubble Collapse on the Damage of Cell Membranes with Different Lipid Peroxidation Levels, The Journal of Physical Chemistry B, (2021).

[50] Z. Yang, Y. Zhou, Z. Feng, X. Rui, T. Zhang, Z. Zhang, A review on reverse osmosis and nanofiltration membranes for water purification, Polymers, 11 (2019) 1252.

[51] T. Ahmad, C. Guria, A. Mandal, A review of oily wastewater treatment using ultrafiltration membrane: A parametric study to enhance the membrane performance, Journal of Water Process Engineering, 36 (2020) 101289.

[52] C.Z. Liang, T.-S. Chung, J.-Y. Lai, A review of polymeric composite membranes for gas separation and energy production, Progress in Polymer Science, 97 (2019) 101141.

[53] W.A. Meulenberg, S. Baumann, W. Deibert, T. Van Gestel, F. Schulze-Küppers, Keramische Membranen: Materialien–Bauteile–potenzielle Anwendungen, Chemie-Ingenieur-Technik, 91 (2019) 1091-1100.

[54] S. Gruener, P. Huber, Knudsen diffusion in silicon nanochannels, Physical Review Letters, 100 (2008) 064502.

[55] P. Pandey, R. Chauhan, Membranes for gas separation, Progress in Polymer Science, 26 (2001) 853-893.

[56] T. Graham, LV. On the absorption and dialytic separation of gases by colloid septa, The London, Edinburgh, and Dublin Philosophical Magazine and Journal of Science, 32 (1866) 401-420.

[57] M.B. Shiflett, H.C. Foley, Ultrasonic deposition of high-selectivity nanoporous carbon membranes, Science, 285 (1999) 1902-1905.

[58] P. Bernardo, E. Drioli, G. Golemme, Membrane gas separation: A review/state of the art, Industrial & Engineering Chemistry Research, 48 (2009) 4638-4663.

[59] L.M. Robeson, The upper bound revisited, Journal of Membrane Science, 320 (2008) 390-400.

[60] T. Zsirai, A. Al-Jaml, H. Qiblawey, M. Al-Marri, A. Ahmed, S. Bach, S. Watson, S. Judd, Ceramic membrane filtration of produced water: Impact of membrane module, Separation and Purification Technology, 165 (2016) 214-221.

[61] A.J. Burggraaf, L. Cot, Fundamentals of inorganic membrane science and technology, Elsevier, 1996.

[62] H.-D. Tietz, Technische Keramik: Aufbau, Eigenschaften, Herstellung, Bearbeitung, Prüfung, Springer-Verlag, 2013.

[63] W. Kollenberg, Technische Keramik: Grundlagen, Werkstoffe, Verfahrenstechnik, Vulkan-Verlag GmbH, 2004.

[64] V. Kharton, I. Marozau, N. Vyshatko, A. Shaula, A. Viskup, E. Naumovich, F. Marques, Oxygen ionic conduction in brownmillerite $CaAl_{0.5}Fe_{0.5}O_{2.5+\delta}$, Materials Research Bulletin, 38 (2003) 773-782.

[65] D. Hohnke, Ionic conduction in doped oxides with the fluorite structure, Solid State Ionics, 5 (1981) 531-534.

[66] Y. Teraoka, H. Zhang, K. Okamoto, N. Yamazoe, Mixed ionic-electronic conductivity of $La_{1-x}Sr_xCo_{1-y}Fe_yO_{3-\delta}$ perovskite-type oxides, Materials Research Bulletin, 23 (1988) 51-58.

[67] K. Ohgushi, J.-i. Yamaura, M. Ichihara, Y. Kiuchi, T. Tayama, T. Sakakibara, H. Gotou, T. Yagi, Y. Ueda, Structural and electronic properties of pyrochlore-type $A_2Re_2O_7$ (A= Ca, Cd, and Pb), Physical Review B, 83 (2011) 125103.

[68] S. Jacobo, Novel method of synthesis for double-perovskite $Sr_2FeMo_{O.6}$, Journal of Materials Science, 40 (2005) 417-421.

[69] V. Eyert, K.-H. Hock, Electronic structure, itinerant magnetism and orbital ordering of K_2NiF_4-type compounds, Journal of Physics: Condensed Matter, 5 (1993) 2987.

[70] H. Worch, W. Pompe, W. Schatt, Werkstoffwissenschaft, John Wiley & Sons, 2011.

[71] J. Hojo, Materials Chemistry of Ceramics, Springer, 2019.

[72] T. Ishihara, Inorganic perovskite oxides, Springer Handbook of Electronic and Photonic Materials, Springer, 2017, 1-1.

[73] W. Kleber, H.-J. Bautsch, J. Bohm, D. Klimm, Einführung in die Kristallographie, Oldenbourg Verlag, 2010.

[74] I. Hussain, H.P. Tran, J. Jaksik, J. Moore, N. Islam, M.J. Uddin, Functional materials, device architecture, and flexibility of perovskite solar cell, Emergent Materials, 1 (2018) 133-154.

[75] M. Pena, J. Fierro, Chemical structures and performance of perovskite oxides, Chemical Reviews, 101 (2001) 1981-2018.

[76] V.M. Goldschmidt, Die Gesetze der Krystallochemie, Naturwissenschaften, 14 (1926) 477-485.

[77] J.D. Patterson, B.C. Bailey, Solid-state physics: Introduction to the theory, Springer Science & Business Media, 2007.

[78] J. Frenkel, Über die Wärmebewegung in festen und flüssigen Körpern, Zeitschrift für Physik, 35 (1926) 652-669.

[79] W. Schottky, Über den Mechanismus der Ionenbewegung in festen Elektrolyten, Zeitschrift für Physikalische Chemie, 29 (1935) 335-355.

[80] C. Li, J.J. Chew, A. Mahmoud, S. Liu, J. Sunarso, Modelling of oxygen transport through mixed ionic-electronic conducting (MIEC) ceramic-based membranes: An overview, Journal of Membrane Science, 567 (2018) 228-260.

[81] P. Knauth, H.L. Tuller, Solid-state ionics: Roots, status, and future prospects, Journal of the American Ceramic Society, 85 (2002) 1654-1680.

[82] H. Böhm, Einführung in die Metallkunde, Bibliogr. Inst., 1968.

[83] J. Maier, J. Jamnik, M. Leonhardt, Kinetics of oxygen stoichiometry changes, Solid State Ionics, 129 (2000) 25-32.

[84] H.J. Bouwmeester, Dense ceramic membranes for methane conversion, Catalysis today, 82 (2003) 141-150.

[85] X.-Y. Wu, A.F. Ghoniem, Mixed ionic-electronic conducting (MIEC) membranes for thermochemical reduction of CO_2: A review, Progress in Energy and Combustion Science, 74 (2019) 1-30.

[86] S.K. Burnwal, S. Bharadwaj, P. Kistaiah, Review on MIEC cathode materials for solid oxide fuel cells, Journal of Molecular and Engineering Materials, 4 (2016) 1630001.

[87] A. Feldhoff, J. Martynczuk, M. Arnold, M. Myndyk, I. Bergmann, V. Šepelák, W. Gruner, U. Vogt, A. Hähnel, J. Woltersdorf, Spin-state transition of iron in $(Ba_{0.5}Sr_{0.5})(Fe_{0.8}Zn_{0.2})O_{3-\delta}$ perovskite, Journal of Solid State Chemistry, 182 (2009) 2961-2971.

[88] M. Arnold, Q. Xu, F.D. Tichelaar, A. Feldhoff, Local charge disproportion in a high-performance perovskite, Chemistry of Materials, 21 (2009) 635-640.

[89] X. Zhu, H. Liu, Y. Cong, W. Yang, Permeation model and experimental investigation of mixed conducting membranes, AIChE Journal, 58 (2012) 1744-1754.

[90] P.-M. Geffroy, E. Blond, N. Richet, T. Chartier, Understanding and identifying the oxygen transport mechanisms through a mixed-conductor membrane, Chemical Engineering Science, 162 (2017) 245-261.

[91] K. Li, Ceramic membranes for separation and reaction, John Wiley & Sons, 2007.

[92] C. Wagner, Equations for transport in solid oxides and sulfides of transition metals, Progress in Solid State Chemistry, 10 (1975) 3-16.

[93] F. Kröger, H. Vink, Relations between the concentrations of imperfections in crystalline solids, Solid State Physics, 3 (1956) 307-435.

[94] H.J. Bouwmeester, H. Kruidhof, A. Burggraaf, Importance of the surface exchange kinetics as rate limiting step in oxygen permeation through mixed-conducting oxides, Solid State Ionics, 72 (1994) 185-194.

[95] J. Caro, H. Wang, C. Tablet, A. Kleinert, A. Feldhoff, T. Schiestel, M. Kilgus, P. Kölsch, S. Werth, Evaluation of perovskites in hollow fibre and disk geometry in catalytic membrane reactors and in oxygen separators, Catalysis Today, 118 (2006) 128-135.

[96] S. Saher, M. Meffert, H. Störmer, D. Gerthsen, H.J. Bouwmeester, Grain-size dependence of the deterioration of oxygen transport for pure and 3 mol% Zr-doped $Ba_{0.5}Sr_{0.5}Co_{0.8}Fe_{0.2}O_{3-\delta}$ induced by thermal annealing, Journal of Materials Chemistry A, 5 (2017) 4982-4990.

[97] V. Kharton, V. Tikhonovich, L. Shuangbao, E. Naumovich, A. Kovalevsky, A. Viskup, I. Bashmakov, A. Yaremchenko, Ceramic microstructure and oxygen permeability of $SrCo(FeM)O_{3-\delta}$ (M= Cu or Cr) perovskite membranes, Journal of the Electrochemical Society, 145 (1998) 1363-1373.

[98] M. Reichmann, P.-M. Geffroy, N. Richet, T. Chartier, Impact of microstructure on oxygen semi-permeation performance of perovskite membranes: Understanding of oxygen transport mechanisms, Journal of Power Sources, 324 (2016) 774-779.

[99] S. Diethelm, J. Sfeir, P. Buffat, Correlation between oxygen transport properties and microstructure in $La_{0.5}Sr_{0.5}FeO_{3-\delta}$, Journal of the European Ceramic Society, 25 (2005) 2191-2196.

[100] P. Zeng, R. Ran, Z. Chen, H. Gu, Z. Shao, J.D. da Costa, S. Liu, Significant effects of sintering temperature on the performance of $La_{0.6}Sr_{0.4}Co_{0.2}Fe_{0.8}O_{3-\delta}$ oxygen selective membranes, Journal of Membrane Science, 302 (2007) 171-179.

[101] S.J. Xu, W.J. Thomson, Oxygen permeation rates through ion-conducting perovskite membranes, Chemical Engineering Science, 54 (1999) 3839-3850.

[102] S. Loeb, S. Sourirajan, Sea water demineralization by means of an osmotic membrane, ACS Publications, 1963.

[103] P. Vandezande, L.E. Gevers, I.F. Vankelecom, Solvent resistant nanofiltration: Separating on a molecular level, Chemical Society Reviews, 37 (2008) 365-405.

[104] J.T. Jung, J.F. Kim, H.H. Wang, E. Di Nicolo, E. Drioli, Y.M. Lee, Understanding the non-solvent induced phase separation (NIPS) effect during the fabrication of microporous PVDF membranes via thermally induced phase separation (TIPS), Journal of Membrane Science, 514 (2016) 250-263.

[105] S. Deshmukh, K. Li, Effect of ethanol composition in water coagulation bath on morphology of PVDF hollow fibre membranes, Journal of Membrane Science, 150 (1998) 75-85.

[106] C.F. Wan, T. Yang, G.G. Lipscomb, D.J. Stookey, T.-S. Chung, Design and fabrication of hollow fiber membrane modules, Hollow Fiber Membranes, (2021) 225-252.

[107] W.D. Kingery, H.K. Bowen, D.R. Uhlmann, Introduction to ceramics, John Wiley & Sons, 1976.

[108] H. Salmang, H. Scholze, Keramik, Springer-Verlag, 2006.

[109] L.C. De Jonghe, M.N. Rahaman, 4.1 Sintering of ceramics, Handbook of Advanced Ceramics: Materials, Applications, Processing and Properties, 2 (2003) 187.

[110] M.N. Rahaman, Ceramic processing and sintering, CRC Press, 2017.

3. LCCF hollow fiber manufacturing and application in a microwave air plasma reactor

3.1. Summary

Dense ceramic oxygen-separating membranes used in practical applications should not only possess good oxygen permeability, but also good CO_2 stability. The main efforts in this chapter were devoted to the manufacturing of hollow fiber membranes from the perovskite LCCF and the first experiments regarding oxygen permeation in CO_2 containing atmosphere as well as first experiments in an air plasma to prove the thermal shock resistance of the hollow fiber membranes.

In the paper, the manufacturing of gas tight hollow fibers from LCCF by the phase inversion and sintering process was investigated. The study has shown the negative influence of sulphur containing polymer binder on the permeation. Hollow fiber membranes with a sulphur free binder has a good CO_2 resistance, which can be seen by the long-term permeation test at 900 °C. The oxygen permeation is constant at 1.03 ml min^{-1} cm^{-2} after initial fluctuations for more than 200 h.

The measurements in the air plasma showed that the general applicability is given and that oxygen can be separated from an air plasma with values up to 2.26 ml min^{-1} cm^{-2}. In contrast to the conventional oven, the thermal stress for the hollow fiber is much higher due to the fast heating. The temperature reaches values up to 1000 °C within seconds. This shows the good thermal shock resistance of the LCCF hollow fiber.

3.2. Einsatz von perowskitischen Hohlfasermembranen in einem Mikrowellenplasma

Frederic Buck, Irina Kistner, Christoph Rösler, Andreas Schulz, Matthias Walker, Günter E.M. Tovar, Thomas Schiestel

Use of perovskite hollow fiber membranes in a microwave plasma

Einsatz von perowskitischen Hohlfasermembranen in einem Mikrowellenplasma

Frederic Buck[1], Irina Kistner[2], Christoph Rösler[1], Andreas Schulz[2], Matthias Walker[2], Günther Tovar[2], Thomas Schiestel[1]

Abstract

For the first time the combination of a separation process with a plasma process was successfully tested. In this case, the oxygen is separated by a mixed-conducting perovskite membrane. At 1 kW a permeation of 2.24 ml min^{-1} cm^{-2} could be achieved. Corresponding perovskite membranes have been manufactured as hollow fibers with a very good CO_2 stability. The hollow fibers showed a constant permeation over more than 200 h. Furthermore, a spinning process with a sulphur-free polymer binder has been established.

Key words: gas separation, hollow fiber, membrane, plasma

[1]Fraunhofer Institute for Interfacial Engineering and Biotechnology IGB, 70569 Stuttgart, Germany

[2]Institute of Interfacial Process Engineering and Plasma Technology, Universität Stuttgart, 70569 Stuttgart, Germany

1. **Introduction**

Certain perovskite ceramics are capable of highly selective separation of oxygen from gas mixtures in the presence of a partial pressure gradient [1, 2]. The high selectivity of the separation is based on the use of mixed ionic-electronic conducting materials. At elevated temperatures (usually at $T > 700\ °C$), not only electrons are conducted through the membrane, but oxygen ions diffuse in the opposite direction via vacancies in the crystal lattice [3, 4].

The membranes can be used in this process in different geometries, with flat and tubular membranes commonly used [2]. An interesting possibility to combine the special material properties with an effective specific membrane surface is the use of a hollow fiber geometry with an outer diameter in the millimeter range [5]. Such membranes have a high specific separation area with a very low material consumption at the same time.

However, no industrial application of such membranes has yet been achieved. This is due, among other things, to their limited chemical and thermochemical stability [6]. For example, high performance materials such as $Ba_xSr_xCo_yFe_zO_{3-\delta}$ decompose to carbonates in the presence of CO_2 [3, 7]. However, initial materials have been developed that exhibit good CO_2 stability [1, 6, 8-10]. $La_wCa_xCo_yFe_zO_{3-\delta}$ (LCCF) has shown great promise in this regard, as it exhibits high stability to CO_2 and CO, as well as good thermal shock resistance. In the literature [1, 6], the material has already been investigated as a flat membrane. The focus of this work is to develop a fabrication process for LCCF hollow fibers and to investigate permeation in a CO_2 atmosphere. In addition, attempts to use such membranes in a microwave plasma for the separation of oxygen are described here for the first time.

2. **Experimental**

   2.1. **Manufacturing of perovskite hollow fibers**

The manufacturing process of ceramic hollow fibers consists of several individual steps: spinning dope manufacturing, wet spinning and sintering (Figure 1) [3, 11]. In the wet spinning process, the production is carried out by the non-solvent induced phase inversion process (in short: NIPS) [3, 12]. Starting from a homogenized spinning dope, the solid hollow fiber is formed by contact with a non-solvent. Subsequently, an exchange of solvent and non-solvent takes place, which are miscible with each other and phase separation is induced. A solid polymer-rich phase enclosing the ceramic particles and a polymer-poor liquid phase are formed. After washing the hollow fibers, the sintering process at temperatures above $1000\ °C$ follows.

In this process, the organic binder is first burned off and then the membrane is sintered together to form a gastight wall.

Each individual sub-step has an influence on the subsequent properties of the hollow fibers. During wet spinning, the geometry of the hollow fiber can be influenced by varying the spinneret and spinning parameters. In the sintering process, the tightness and the texture of the material structure of the membrane are controlled.
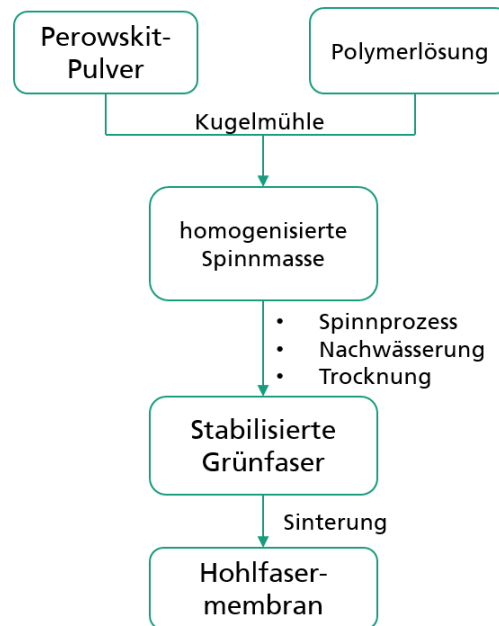
Figure 1: Manufacturing principle of ceramic hollow fibers.

The used LCCF was purchased from the company Cerpotech. This powder was mixed with a polymeric binder and N-ethyl-2-pyrrolidone and homogenized for 34 h using a ball mill. The slurry was then spun into stabilized LCCF green fibers. The final green fibers were cut to 0.6 m and sintered horizontally at 1120 °C for 16 h. During the sintering process, the fibers shrunk by 30% in diameter and 23% in length (Figure 2). By means of the four-point bending test, a high mechanical stability of 277 MPa was determined. The fibers were gas-tight up to a pressure of 5 bar.

Figure 2: Light microscopic and scanning electron microscopic images of gas-tight LCCF capillaries

2.2. Setup of the permeation testing device

To study the oxygen permeability of the capillary membranes, the permeation measurement device was used, as schematically shown in Figure 3. Special T-joints are used at the inlet and outlet of the reactor to allow complete sealing of the capillaries. In the laboratory setup, the feed gas (N_2 and O_2) is fed into the capillary and the sweep gas (N_2), outside the capillary. The outgoing oxygen flows from each side are recorded using an oxygen meter (Zirox SGM7). Since there is a temperature drop along the length of the furnace, only a short active fiber length inside the furnace is used. This allows an accurate determination of the permeation data. The oxygen permeation JO_2 in (ml cm^{-2} min^{-1}) is calculated as follows [3]:

$$J_{O2} = \frac{c_{O2} \cdot \dot{V}_s}{A_{Membran}} \tag{1}$$

Where c_{O2} is the oxygen concentration on the permeate side (in vol%), $\dot{V}_s$ is the sweep flow (in ml/min) and $A_{Membran}$ the membrane area (in cm^2). To calculate the membrane area, the logarithmic mean is used for hollow fibers:

$$A_{Membran} = \frac{\pi \cdot L \cdot (D_a - D_i)}{ln\left(\frac{D_a}{D_i}\right)} \tag{2}$$

With D_a as outer and D_i as inner diameter of the hollow fiber and the effective membrane length L.
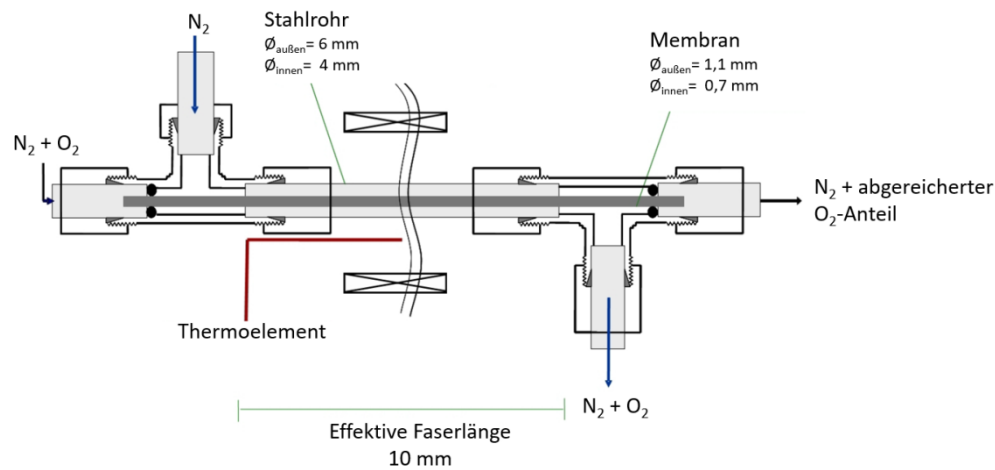
Figure 3: Schematic setup of the permeation testing device.

2.3. <u>Principle of the plasma torch</u>

A microwave plasma torch at atmospheric pressure is used as the plasma source [13, 14]. Figure 4 a) shows a schematic diagram of the plasma torch setup. It mainly consists of a broadband cylindrical resonator and a narrowband coaxial resonator. If a microwave with a frequency of 2.45 GHz is guided into the resonator via a waveguide and the length l_{KR} of the coaxial resonator corresponds exactly to a quarter of the wavelength of the microwave, resonance occurs. This results in very high field strengths at the tip of the coaxial inner conductor and the plasma is ignited. After ignition, the plasma enters the cylinder mode and is operated there. The gas can be supplied via four tangential gas inlets and one axial gas inlet. The inflow via the tangential gas inlets leads to an enveloping rotational flow which encloses the plasma in the center of the quartz glass tube. Thus, the plasma torch allows self-ignition and operation with a free-standing plasma (see Figure 4 b), which ensures almost maintenance-free operation.
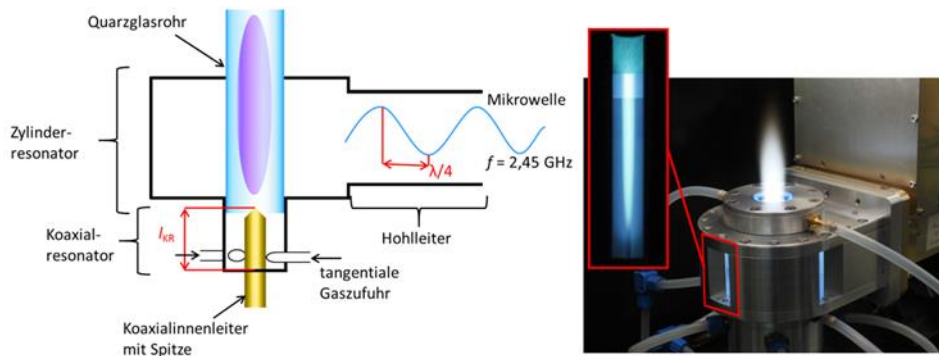
Figure 4: a) Schematic diagram of the plasma torch; b) Plasma torch in operation with a free-standing air plasma.

3. Results

3.1. Influence of the polymer binder on the permeation

In the manufacturing of the hollow fibers, polysulfone was first used as a binder, since this is a commonly used material in literature [5, 7, 11]. Figure 5 shows the result of a long-term test of an LCCF hollow fiber made with polysulfone. The test was conducted in a 50 % CO_2 atmosphere. A significant decrease in permeation over time can be seen. From SEM images (Figure 6a), a layer can be seen on the outside of the hollow fiber, which was detected as a sulfur-containing deposit by EDX measurement (Figure 6b). Therefore, for the subsequent tests, the polymer binder was changed to polyetherimide, as this is sulfur-free.
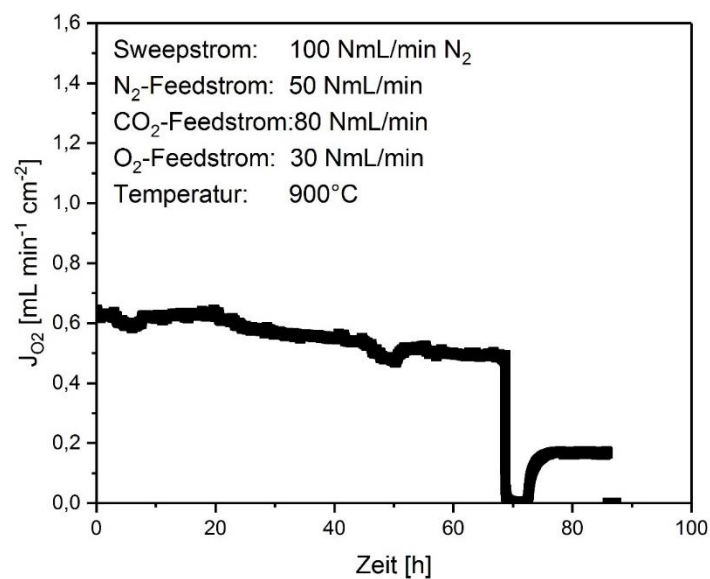
Figure 5: Permeation test over time in a 50% CO_2-atmosphere.
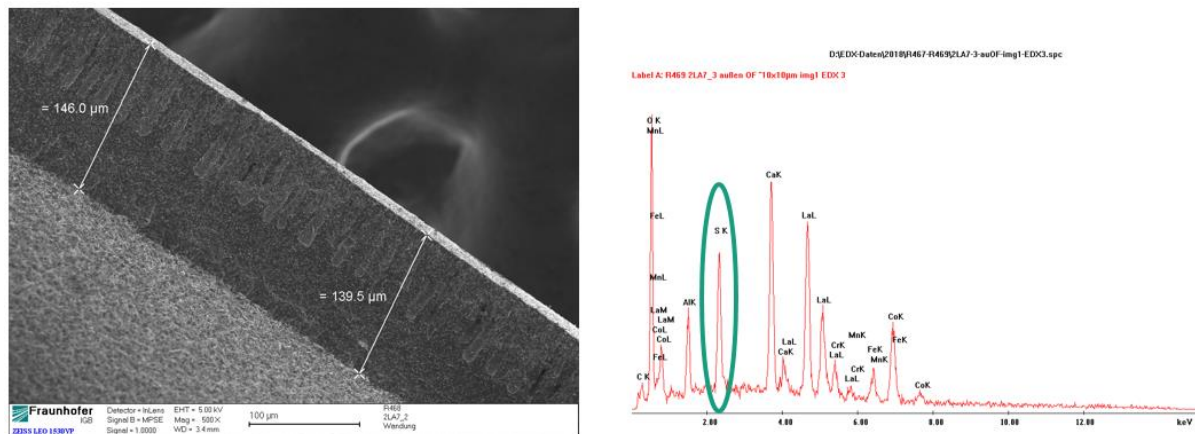
Figure 6: a) SEM image of the cross section of a LCCF hollow fiber b) EDX image of a LCCF hollow fiber.

Figure 7 shows the curves of two hollow fibers as a function of temperature, which were produced with different polymer binders. The black squares are the measurement results of the hollow fiber with polysulfone and the blue triangles with polyetherimide. The experimental conditions are summarized in Figure 7. Each measurement point in the diagram was obtained from seven individual measurements, and the measurement error is in the range of the symbol size. Measurements were made from high to low temperatures. The geometry of the individual fibers is also shown in Figure 7. They have a homogeneous round shape. The wall thicknesses of the fibers nearly identical (220 µm). Due to the same wall thicknesses, a good comparability is given. The oxygen permeations increase exponentially with increasing temperature for both hollow fibers. At a temperature of 950 °C, a permeation of 2.71 ml min^{-1} cm^{-2} is achieved with polyetherimide as binder. In comparison, a permeation of 1.43 ml min^{-1} cm^{-2} is achieved at 950 °C with polysulfone as binder. This illustrates that polyetherimide as a binder is more suitable for the LCCF since this has no sulfur compounds, and thus has no negative effect on the permeation. In the literature, maximum permeation values of 0.43 ml min^{-1} cm^{-2} at 950 °C have been previously achieved for the LCCF material [6]. The high permeation values can be explained by the hollow fiber geometry, as they have a thinner wall (220 µm) and thus lower resistance. In the literature, only pellets have been used so far (wall thickness 1mm) [6]. Even at 1000 °C, the material exhibits good resistance and a high permeation (4.02 ml min^{-1} cm^{-2}). Stability at high temperatures is very important for the capillaries to remain stable in plasma.
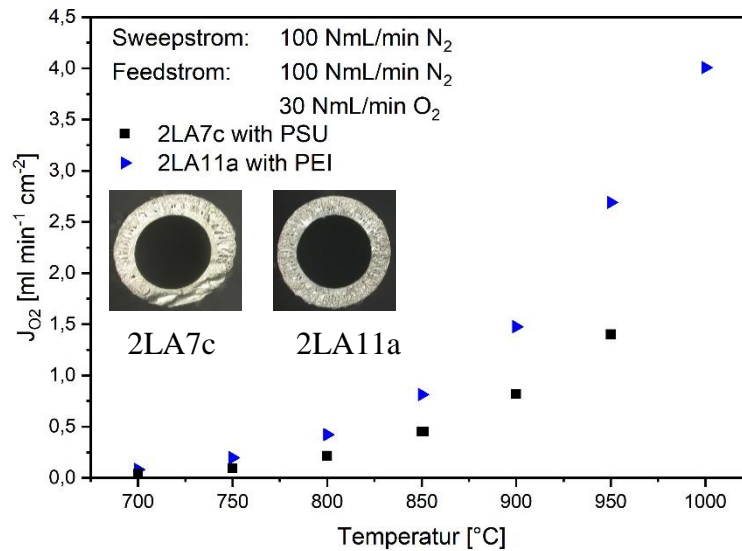
Figure 7: Comparison of two hollow fibers with different polymer binder. (blue triangles: with polyetherimide; black squares: with polysulfone).

3.2. Long term stability in CO_2

Another important criterion for the use of the material is its resistance in a CO_2 atmosphere. As already shown in Figure 5, problems occurred which are related to the polymer binder. Therefore, the long-term test (Figure 8) was repeated with polyetherimide as binder. In this test, a LCCF hollow fiber has been tested for more than 200 h in an O_2/N_2 atmosphere containing 50 % CO_2. The permeation is plotted here against time. The test was performed at 900 °C. For clarity, the experimental conditions are also shown in Figure 8. With the help of the dashed line, the median of the measured values (1.04 ml min^{-1} cm^{-2}) has been plotted. This clearly shows that there is no significant decrease in permeation over the entire period. After a running-in period of approx. 30 h, the permeation stabilizes and then remains constant. The strong deviations at approx. 75 h and 190 h are due to the feed flow, which is not constant at times. However, it is clear that there is a deviation of about 0.4 ml min^{-1} cm^{-2} in the comparison between the measurement point at 900 °C in Figure 6 and the results of Figure 7, which can be attributed to the presence of CO_2. The deviation could be due to the fact that the CO_2 inhibits the adsorption of the oxygen atoms on the membrane surface.
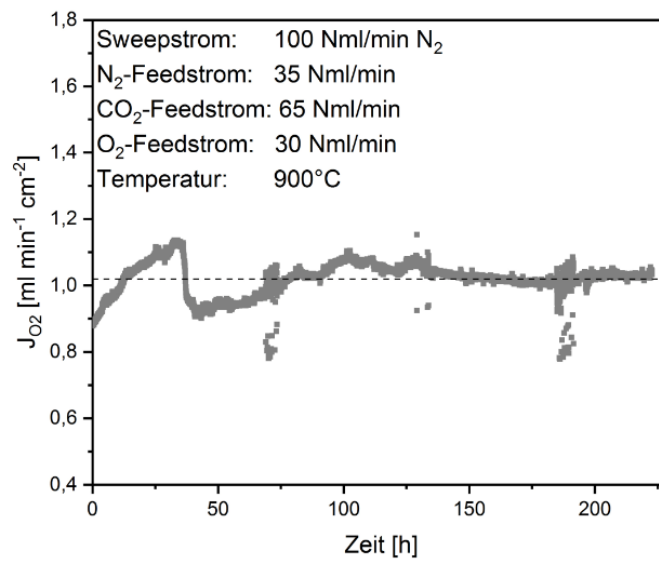
Figure 8: Oxygen permeation of a LCCF hollow fiber in 50 % CO_2 at 900 °C over time.

3.3. <u>Measurements in plasma</u>

To calculate the permeance in the plasma, knowledge of the active membrane area is required (see formula 2). For this purpose, a temperature profile of the plasma at the location of the capillary as a function of power was recorded by means of a thermos couple. Figure 9 shows the temperature for different microwave powers as a function of x-position. A temperature of $T > 800°C$ is only given at powers of $P \geq 0.8$ kW. The active permeation length of the hollow fibers is here about 2 cm.
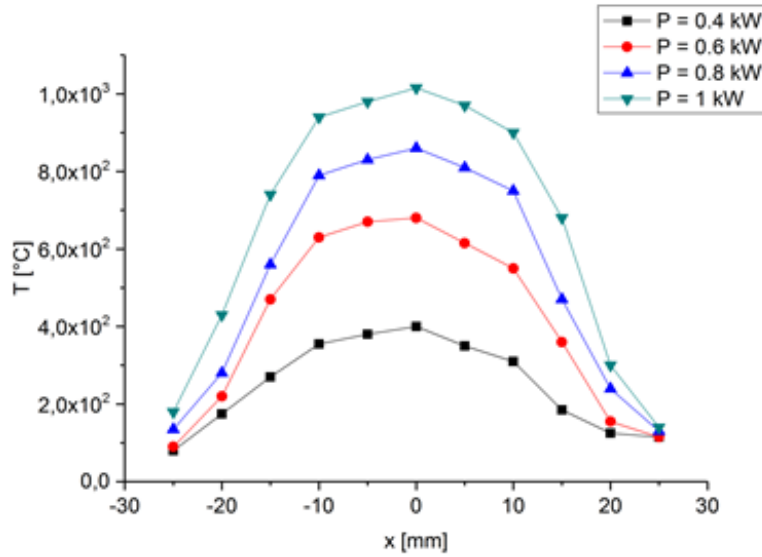
Figure 9: Temperature profile of an air plasma for different powers at a flow of 25 l min^{-1}.

The oxygen permeance of the LCCF hollow fibers were measured in an air plasma. Figure 10 shows an example of the oxygen permeation as a function of microwave power for an air flow rate of 25 l min^{-1} and a carrier gas flow rate of 140 ml min^{-1}. It is clear that the permeation increases with increasing power. A permeation of 2.24 ml min^{-1} cm^{-2} is achieved at a microwave power of 1kW. Which corresponds to a temperature of about 980 °C. At lower powers (0.6 kW), no permeation can be measured, since the temperature required to activate the membrane is not present. However, it is clear that a combination of plasma process and separation process is in principle possible.
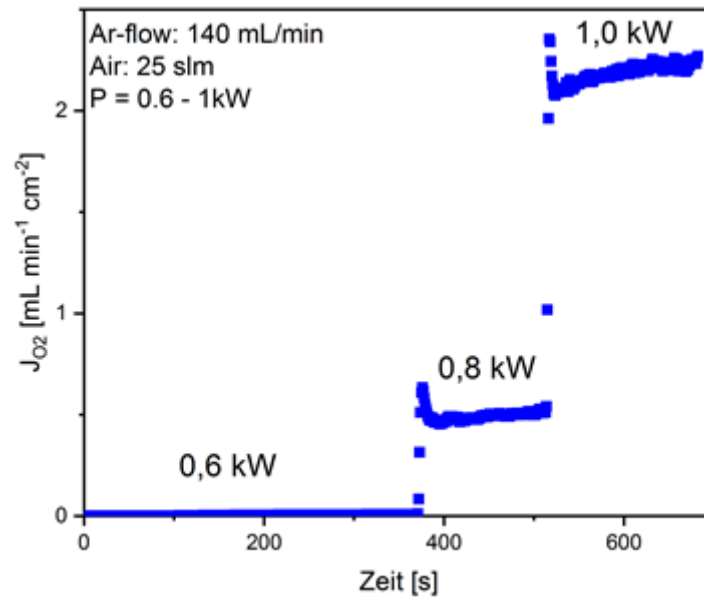
Abbildung 10: Oxygen permeation of a LCCF hollow fiber in an air plasma at different microwave powers.

Comparing oxygen transport in a plasma atmosphere at 1 kW (2.24 ml min^{-1} cm^{-2}) with the oxygen transport in a normal furnace at 950 °C (2.71 ml min^{-1} cm^{-2}), only minor differences are observed. Since the determination of the active surface in plasma is associated with a relatively large error, the observed differences are not significant.

4. <u>Summary</u>

Gas-tight ceramic hollow fibers could be fabricated from the perovskite material La$_w$Ca$_x$Co$_y$Fe$_z$O$_{3-\delta}$ (LCCF) by an economically advantageous spinning process, and in addition, the spinning process could be established with a new sulfur-free polymer binder. After burning off the polymer binder and sintering, the perovskite hollow fibers can be applied to the separation of oxygen from various gas compositions and in a plasma. Furthermore, they possess nearly infinite selectivity for oxygen. Due to the hollow fiber geometry, the fibers have a small wall thickness (220 µm) which allows the oxygen flux to increase in orders of magnitude up to 4 ml min^{-1} cm^{-2}.

The fabricated hollow fiber membranes of LCCF also exhibit stable oxygen permeation in a CO_2 atmosphere at 900 °C. Over the 200 h, the oxygen permeation is stable at an average value of 1.04 ml min^{-1} cm^{-2}.

In addition, it was shown that the combination of plasma and separation technology is in principle possible. Despite the difficult conditions in the plasma, the hollow fibers show no signs of degradation and permeations of up to 2.24 ml min^{-1} cm^{-2} can be achieved.

Literature

1. Salehi, M., et al., *Oxygen permeation and stability study of $(La_{0.6}Ca_{0.4})_{0.98}(Co_{0.8}Fe_{0.2})$ $O_{3-\delta}$ membranes.* Journal of Membrane Science, 2017. **542**: p. 245-253.

2. Caro, J., et al., *Perowskit-Hohlfasermembranen für die katalytische Partialoxidation von Methan zu Synthesegas.* Chemie Ingenieur Technik, 2007. **79**(6): p. 831-842.

3. Zipperle, M., *Gemischtleitende Hohlfasermembranen des Systems $BaCo_xFe_yZr_zO_{3-d}$ für die Sauerstoffseparation.* 2012: Fraunhofer Verlag.

4. Hashim, S.M., A.R. Mohamed, and S. Bhatia, *Current status of ceramic-based membranes for oxygen separation from air.* Advances in Colloid and interface Science, 2010. **160**(1-2): p. 88-100.

5. Schiestel, T., et al., *Hollow fibre perovskite membranes for oxygen separation.* Journal of Membrane Science, 2005. **258**(1-2): p. 1-4.

6. Efimov, K., et al., *Ca-containing CO_2-tolerant perovskite materials for oxygen separation.* Journal of membrane science, 2012. **389**: p. 205-215.

7. Arnold, M., H. Wang, and A. Feldhoff, *Influence of CO_2 on the oxygen permeation performance and the microstructure of perovskite-type $(Ba_{0.5}Sr_{0.5})(Co_{0.8}Fe_{0.2})$ $O_{3-\delta}$ membranes.* Journal of Membrane Science, 2007. **293**(1-2): p. 44-52.

8. Stevenson, J., et al., *Electrochemical properties of mixed conducting perovskites $La_{1-x}M_xCo_{1-y}Fe_yO_{3-\delta}$ (m= Sr, Ba, Ca).* Journal of the Electrochemical Society, 1996. **143**(9): p. 2722-2729.

9. Teraoka, Y., T. Nobunaga, and N. Yamazoe, *Effect of cation substitution on the oxygen semipermeability of perovskite-type oxides.* Chemistry Letters, 1988. **17**(3): p. 503-506.

10. Zhang, C., J. Sunarso, and S. Liu, *Designing CO_2-resistant oxygen-selective mixed ionic–electronic conducting membranes: guidelines, recent advances, and forward directions.* Chemical Society Reviews, 2017. **46**(10): p. 2941-3005.

11. Wang, H., et al., *Perovskite hollow-fiber membranes for the production of oxygen-enriched air.* Angewandte Chemie International Edition, 2005. **44**(42): p. 6906-6909.

12. Lalia, B.S., et al., *A review on membrane fabrication: Structure, properties and performance relationship.* Desalination, 2013. **326**: p. 77-95.

13. Leins, M., et al., *How to ignite an atmospheric pressure microwave plasma torch without any additional igniters.* Journal of visualized experiments: JoVE, 2015(98).

14. Bongers, W., et al., *Plasma-driven dissociation of CO_2 for fuel synthesis.* Plasma processes and polymers, 2017. **14**(6): p. 1600126.

4. Bulk diffusion optimization of LCCF hollow fiber membrane

4.1. Summary

Based on the good results of the previous chapter, the optimization of the bulk diffusion of the LCCF hollow fiber membrane with regard to the oxygen permeation is discussed in this chapter. Firstly, the publication shows the possibility to manufacture hollow fiber with different geometries and different particle sizes. Hollow fibers with outer diameter between 0.76 mm and 1.60 mm were manufactured by using different spinnerets.

The microstructure of the fibers were analysed by SEM, TEM, EDXS and XRD. The LCCF phase contains different amounts of brownmillerite and a spinel-type cobalt oxide phase as foreign phase, depending on the sintering temperatures. The different sintering temperatures (varying between 1070 °C and 1245 °C) result in different particle areas of the hollow fibers. With increasing temperatures the particle area increases from 0.41 μm^2 (1070 °C) to 19.49 μm^2 (1245 °C). The oxygen permeation increases with increasing sintering temperature. Therefore, it can be considered that the grain boundaries act as barriers for the oxygen transport through the bulk.

The reduction of the wall thickness from 244 µm to 81 µm leads to an increase of the oxygen permeation by 111.2 % at 1000 °C. This shows the dependency of the oxygen permeation from the bulk diffusion. On the other hand, the results were analysed by a Wagner plot and showed that the oxygen permeation is still dominated by both transport mechanisms, the surface exchange reactions and the bulk diffusion.

4.2. Permeation improvement of LCCF hollow fiber membranes by spinning and sintering optimization

Frederic Buck, Armin Feldhoff, Jürgen Caro, Thomas Schiestel

Permeation improvement of LCCF hollow fiber membranes by spinning and sintering optimization

Frederic Buck [a,b], Armin Feldhoff [b], Jürgen Caro [b], Thomas Schiestel [a,*]

[a] Fraunhofer Institut für Grenzflächen- und Bioverfahrenstechnik, Nobelstraße 12, 70569 Stuttgart, Germany
[b] Institut für Physikalische Chemie und Elektrochemie, Leibniz Universität Hannover, Callinstraße 3-3A, D-30167 Hannover, Germany

ABSTRACT

The effects of grain size and wall thickness on the oxygen transport mechanism of $(La_{0.6}Ca_{0.4})(Co_{0.8}Fe_{0.2})O_{3-\delta}$ hollow fiber membranes were investigated. For this purpose, hollow fiber membranes of different geometry were prepared with different spinnerets via phase inversion spinning and subsequently sintered at different temperatures. The influence of the manufacturing conditions on the LCCF microstructure were analysed by SEM, XRD and TEM. With increasing sintering temperature, the grain size increased from 0.4 μm^2 at 1070 °C to 19.5 μm^2 at 1245 °C. With bigger grain sizes and lower wall thickness, the oxygen flux shows an increase up to 6.2 ml min^{-1} cm^{-2} (at 1000 °C) in a 50% CO$_2$ atmosphere. This finding implies that the grain boundaries act as oxygen diffusion barriers.

1. Introduction

In the coming decades, one of the biggest challenges is to slow down or to stop global warming [1]. Therefore, it is important to increase the efficiency of renewable energy sources like solar or wind energy. One possibility is to use or to store the energy surplus of these technologies. Chen et al.[2] presented a new concept for using excess electric energy applying mixed ionic and electronic (MIEC) hollow fiber membranes in a so-called plasma-membrane reactor to separate oxygen from CO, which are both formed by thermal CO$_2$ splitting in a microwave plasma [2]. Beside the decomposition of CO$_2$, a further advantage is the use of the remaining CO to produce platform chemicals. Therefore, such membranes must have a very high CO$_2$ stability, a good temperature shock resistance and, furthermore, a high oxygen permeation. In addition, a high surface area is required which can be placed in the plasma to efficiently separate the generated oxygen.

For this CO$_2$ splitting in the microwave reactor we have developed hollow fiber membranes made from the perovskite-type $(La_{0.6}Ca_{0.4})$ $(Co_{0.8}Fe_{0.2})O_{3-\delta}$ (LCCF) and successfully tested in first experiments [3]. Teraoka et al. [4] first mentioned the material LCCF and showed its potential as MIEC membrane [4]. In further publications the excellent CO$_2$ stability and the good temperature turnover resistance was proved [3,5–8]. The membranes can be used in different geometries: flat or tubular membranes are mostly utilized. For a combination of the specific material properties and a high specific surface area, the hollow fiber provides a geometry with the highest potential [9].

In recent decades, many publications dealt with the transport mechanism and the factors influencing the oxygen flux [10–17]. Oxygen transport through an MIEC membrane is dominated either by bulk diffusion or by surface exchange kinetics. To estimate the dominating oxygen transport mechanism, Bouwmeester et al. [10] defined a so-called characteristic thickness L$_c$ for a membrane. They described three constellations [10]:

- If L > 10 L$_c$, the bulk diffusion dominates the transport mechanism
- If 10 L < L$_c$, the surface exchange kinetics dominates the transport mechanism
- If L ~ L$_c$, a mixed regime exists.

By using hollow fibers, wall thicknesses close to the calculated characteristic wall thickness are possible. As the mechanical stability of the hollow fibers will decrease with decreasing wall thickness, a compromise between stability and wall thickness has to be found.

Assuming that the ionic conductivity is much lower than the electronic conductivity, the dominating transport mechanism for hollow fibers can be calculated by Wagner's equation [18]:

$$J_{O2} = \frac{\sigma_i^0 RT}{16 F^2 nL} (p_1^n - p_2^n) \tag{1}$$

Table 1

Parameters of the preparation of LCCF hollow fiber membranes for oxygen permeation studies.

Experimental parameters	Values	
Dimensions of spinneret:		
• D_o	1.0, 2.0, 3.0	mm
• D_i	0.5, 1.2, 2.4	mm
Bore liquid	DI water/NEP (25 v%/75 v%)	
Flow rate of the bore liquid	7.5	$cm^3\ min^{-1}$
External coagulant	DI water	
Air gap	0	cm
Sintering conditions		
• Temperature	1070, 1120, 1170, 1220, 1245	°C
• Time	16	h

with J_{O2} as the oxygen permeation, R as the gas constant, F as the Faraday constant, L as the membrane thickness, T as the temperature, σ_i^0 the ionic conductivity at standard conditions, p_1^n and p_2^n as the oxygen partial pressure at the high pressure side and the low pressure side and n as the fit parameter which can be derived from the experimental data.

With the value of n, the rate-limiting step of oxygen, transport can be estimated. For $n < 0$, bulk diffusion is rate-limiting; for $n \geq 0.5$, the surface exchange kinetics dominates the oxygen flux and for $0 < n < 0.5$, the oxygen permeation is influenced by a mixed regime.

In this paper, oxygen permeation mode has been described by the Wagner equations. However, there are numerous more recent models such as the Xu-Thomson Modell or the Zhu Modell [17,19,20].

The microstructure of such a membrane depends largely on the preparation method and the sintering procedure [9,21–24]. However, in literature a controversy exists regarding the impact of the grain size on the oxygen permeation [25]. For instance, Diethelm et al. [26] investigated the influence of the grain size on oxygen permeation by varying the sintering temperature for the material $La_{0.5}Sr_{0.5}FeO_{3-\delta}$. They observed an increase of permeation with a decrease of the grain size [26]. On the other hand, Zeng et al. [27] studied the influence of the sintering temperature for $La_{0.6}Sr_{0.4}Co_{0.2}Fe_{0.8}O_{3-\delta}$ and figured out that the permeation increases with an increase of the grain size [27]. Consequently, grain boundaries can act as diffusion obstacle or as fast diffusion paths for the oxygen ions [21]. During the sintering process solute segregation as well as impurity enrichment occur. These processes at the grain boundaries can led to an abrupt change of the oxygen exchange at the membrane surface and oxygen transport along and across the grain boundaries. Therefore, it is necessary to find the dominating influence for each material.

The aim of this paper is to investigate the impact of preparation-controlled properties like wall thickness and microstructure on the oxygen permeation through LCCF hollow fiber membranes. The material LCCF combines an excellent stability in a CO_2 atmosphere with a good oxygen permeation. Besides use in a CO_2 plasma, these properties are also important for other applications. The findings of this work can be used to further optimize the performance of LCCF membranes with regard to permeance, and mechanical and chemical stability.

2. Material and methods

The perovskite powder $(La_{0.6}Ca_{0.4})(Co_{0.8}Fe_{0.2})O_{3-\delta}$ (LCCF6482) was prepared by Cerpotech (Tiller, Norway) using a spray pyrolysis process. The hollow fibers were manufactured by a phase inversion and sintering technique which was described elsewhere [3]. In this study, the spinning solution consisted of 58.02% LCCF powder, 7.57% Polyetherimide (Merck KGaA, Darmstadt, Germany) and 34.41% N-Ethyl-2-Pyrollidon (NEP, $\geq$ 98%, Carl Roth GmbH + Co KG, Karlsruhe, Germany). The bore fluid for the spinning process was a mixture of deionised (DI) water/NEP (25%/75%) while DI water was used as the external coagulant. The standard hollow fibers used in the oxygen permeation tests were produced with a spinneret of D_o/D_i 2.0/1.2 mm and sintered at a

temperature of 1220 °C. Table 1 shows all manufacturing parameters for the hollow fibers.

The morphological features of the prepared membranes were examined using a scanning electronic microscope (SEM). Specimens for SEM were polished in cross-section on an Allied High Tech Techprep/ Multiprep system using polymer-embedded diamond lapping films down to 0.5 μm finish. SEM investigations were made on a field-emission instrument of the type JEOL JSM-6700F at 5 kV or 20 kV in secondary electron contrast. The microscope was equipped with an Oxford INCA 300 energy-dispersive x-ray spectrometer (EDXS). The Cameo module of INCA 300 was used to convert spectral information into a rainbow-color image. This tool spreads the color scale of the image over the pixel-by-pixel mapped x-ray spectrum in a way that red color is at low x-ray energy and blue color is at high x-ray energy. Then the corresponding x-ray intensity represents the intensity of the respective color channels. Based on the SEM micrographs, the grain size distribution was statistically calculated by manual measurement of the size of individual grains. For each fiber the size of 100 particles were measured. The mechanical stability was measured by the four-point bending test (Zwick/Roell Z0005, Ulm Germany). For testing the gas tightness each hollow fiber was sealed with polymer resin at one end. Than the hollow fiber was connected to a pressure hose which is used to set a pressure of 4 bar. Finally, the membrane was immersed into water under pressure. If the membrane leaks, bubbles will form on the membrane surface.

For transmission electron microscope (TEM), specimen was polished on polymer embed diamond lapping films from both sides to a final thickness of 10 μm and then 3 kV argon-ion polished to electron transparency in a precision ion polishing systems (PIPS, Gatan model). TEM investigations were made on a filed-emission instrument of the type JEOL JEM-2100F-UHR. The microscope was used for bright-field (BF) imaging, scanning transmission electron microscopy (STEM) and selected area electron diffraction (SAED). The microscope was equipped with a Gatan Imaging Filter (GIF2001), which allowed for electron energy-loss spectroscopy (EELS).

The oxygen permeation properties of the membranes were measured in a high-temperature permeation device which was described in detail elsewhere [28]. O_2, N_2 and CO_2 were injected to the feed side and N_2 were injected to the sweep side. For all measurements the sweep side had a constant flow of 100 Nml min^{-1}. The flow rate at the feed side was varied. For the temperature measurements and the measurement with and without CO_2 the feed flow was 130 Nml min^{-1} with a mixture of 50% CO_2, 23% O_2 and 27% N_2. For the measurement without CO_2 the mixture was 77% N_2 and 23% O_2. To validate the Wagner equation the feed flow was set to 100 Nml min^{-1} with varying composition of O_2 and CO_2. The pressure at the feed side was 2 bar and at the sweep side 1 bar. For the temperature measurements the temperature were decreased in 50 K steps starting at 1000 °C. For the other measurements the temperature was kept constant at 900 °C. The oxygen concentrations for the sweep and the feed flow were measured with an oxygen analyser (Zirox SGM 7). To ensure isothermal conditions, the hollow fibers were coated with gold paste on both ends and sintered at 800 °C for 2 h to obtain a defined 3 cm long permeation zone in the middle of the furnace. The oxygen permeation J_{O2} (ml cm^{-2} min^{-1}) can be calculated with the following equation [28]:

$$J_{O2} = \frac{c_{O2} \cdot \dot{V}_s}{A_{Membrane}} \qquad (2)$$

With c_{O2} as the oxygen concentration on the sweep side (Vol.%), $\dot{V}_s$ sweep flow (ml/min) and $A_{Membran}$ the membrane area (cm^2). To calculate the membrane area the logarithmic mean of the hollow fiber was used:

$$A_{Membrane} = \frac{\pi \cdot L \cdot (D_o - D_i)}{ln\left(\frac{D_o}{D_i}\right)} \qquad (3)$$

Table 2
Resulting geometries of the LCCF hollow fibers for different manufacturing conditions, sintering time 16 h.

Spinneret $D_{outside}$ [mm]	Sintering temperature [°C]	D_o [mm]	D_i [mm]	Wall thickness [μm]	Shrinkage [%]	Average grain size [μm^2]
1	1220	0.76 ± 0.01	0.60 ± 0.01	81 ± 6	36.2	6.43
2	1070	1.23 ± 0.01	0.83 ± 0.01	200 ± 10	34.0	0.41
	1120	1.12 ± 0.02	0.78 ± 0.01	170 ± 12	39.8	0.45
	1170	1.16 ± 0.02	0.80 ± 0.01	180 ± 9	36.9	1.18
	1220	1.20 ± 0.03	0.85 ± 0.01	180 ± 10	37.4	6.34
	1245	1.20 ± 0.04	0.84 ± 0.03	180 ± 11	35.4	19.49
3	1220	1.60 ± 0.03	1.12 ± 0.01	244 ± 25	35.9	6.88
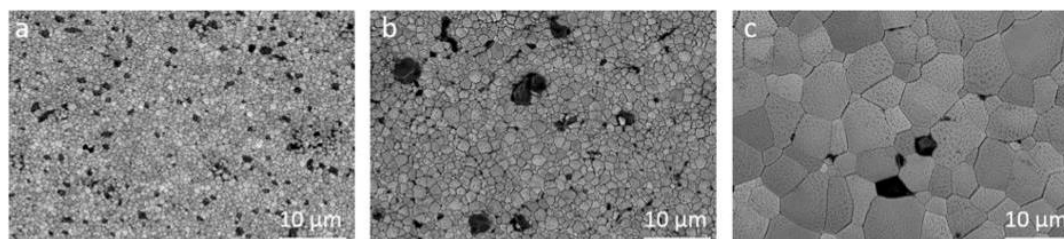
Fig. 1. SEM micrographs of LCCF hollow fiber outer surface spun with the $D_o = 2.0$ mm spinneret and sintered at (a) 1120 °C (b) 1170 °C and (c) 1245 °C.

With D_o as outer and D_i as inner diameter of the hollow fiber and the effective membrane length L.

3. Results and discussion

3.1. Morphology and microstructure

In the preparation of the LCCF hollow fibers, all processing parameters, with exception of the spinneret and the sintering temperature, were fixed. Therefore, change of wall thickness, microstructure and other properties is mainly attributed to the variation of the spinneret and the sintering temperature. The influence of the different parameter on the geometry is shown in Table 2. As shrinkage is in the same range (34.0–39.8%) for all membranes, the resulting geometry is mainly determined by the initial geometry of the green fibers and, therefore, by the dimensions of the spinneret. By using different spinnerets, the wall thickness of the hollow fibers can be adjusted from 80 to 240 μm. On the other hand, the sintering temperature seems to have only a weak influence on the fiber geometry. With an increase of the sintering temperature by about 175 °C, the wall thickness decreases by only 10% from 200 μm to 180 μm.

Furthermore, the average grain sizes of membranes prepared by different manufacturing conditions are shown in Table 2. The grain sizes are derived from SEM images (Fig. 1) by a particle analysis. Obviously, the sintering temperature has a significant effect on the grain sizes of the membranes. The average grain size increases from 0.41 μm^2 at a sintering temperature of 1070 °C to 19.49 μm^2 at 1245 °C. The grain size of the fiber manufactured with different spinnerets and the same sintering conditions shows similar particle sizes (Table 2).

Fig. 2 shows LCCF hollow fibers spun with a spinneret of $D_o = 2$ mm and sintered at different temperatures. The hollow fiber spun with the 2 mm spinneret and sintered at 1220 °C, which is used as standard material in the oxygen permeation studies (Fig. 2b, d, f, h), has an outer diameter of approximately 1.2 mm and an inner diameter of approximately 0.85 mm. The wall thickness varies between 170 μm and 190 μm. The cross-sections of the hollow fibers are not completely dense but show some radially aligned elongated pores of up to 40 μm in length (Fig. 2c, d), which is typical for hollow fibers obtained from phase inversion spinning. The secondary electron contrast in Fig. 2e, f exhibits a multiphase composition of the LCCF-6482 ceramic, which is shown more distinctly by EDXS in Fig. 2g, h. The green areas correspond to a

perovskite phase with La:Ca > 2:3 and the red areas to a brownmillerite phase with La:Ca < 2:3. The blue areas correspond to a spinel-type cobalt oxide (Co_3O_4). The Co:Fe ratio is more or less identical in rhombohedral perovskite and orthorhombic brownmillerite.

Obviously, there is no perovskite of the exact nominal composition LCCF6482 (La:Ca = 2:3), but a rhombohedral perovskite enriched in lanthanum and a brownmillerite enriched in calcium, as compared to the nominal composition, have formed in the ceramic. In addition, cubic Co_3O_4 is present. The results are in good agreement with Efimov et al. [8]. Stevenson et al. [5] have investigated synthesis, oxygen content, electrical conductivity and oxygen permeation of various La-containing perovskite-based ceramics including LCCF6482 [5]. Phase purity, based on X-ray diffraction (XRD), is tabulated and by-phases are mentioned: $Ca_2Fe_2O_5$ (brownmillerite), $Ca_2Co_2O_5$ (brownmillerite), $CaFe_3O_5$, CoO (rock-salt type).

Efimov et al. [8] have reconsidered LCCF as alternative materials for oxygen separation membranes operated in CO_2 containing atmosphere [8]. They emphasize that optimizing sintering condition is crucial to prevent the formation of non-perovskite phases. Furthermore, they have shown that LCCF with nominal compositions $(La_{1-x}Ca_x)(Co_{0.8}Fe_{0.2})O_{3-\delta}$ are multiphase composites, which consist mainly of three phases: Perovskite (rhombohedral), brownmillerite (orthorhombic), spinel-type Co_3O_4 (cubic). Interestingly, in the hollow fiber sintered at 1220 °C for 16 h, brownmillerite (red) is found to enwrap the cobalt oxide inclusions (blue).

Because the specimen sintered at 1120 °C for 16 h did contain all phases in some amount, it was chosen for phase analysis using TEM and XRD. From the two areas in the TEM bright-field micrograph of Fig. 3a (approximately 120 nm in diameter), SAED pattern were obtained. For the perovskite, the 1 0 0$_p$ reflection was obtained at 2.67 Å (see Fig. 3c). For the brownmillerite, the $[0\,1\,1]_b$ zone axis pattern was obtained (see Fig. 3d). It shows sets of strong and weak reflections. It is worth mentioning that the 200$_b$ reflection (2.57 Å) is around 4% smaller than for rhombohedral LaCo$_{0.8}$Fe$_{0.2}$O$_{3-\delta}$ (ICSD 190099, [29]), but the $0\,2\,\overline{2}_b$ (4.44 Å) and $14\overline{4}_b$ (2.06 Å) reflections match this reference structure [29]. Obviously, the lattice planes (1 0 0)$_p$ of the perovskite and $(0\,2\,\overline{2})_b$ of the brownmillerite are parallel to each other.

Core-loss EEL spectra of perovskite and brownmillerite show almost identical intensity ratios for Co-L$_{2,3}$:Fe-L$_{2,3}$, but the intensity of the La-M$_{4,5}$ ionization edges is distinctly lower in the brownmillerite. Note that the Ca-L$_{2,3}$ ionization edge (350 eV) is out of display. The O-K near-edge
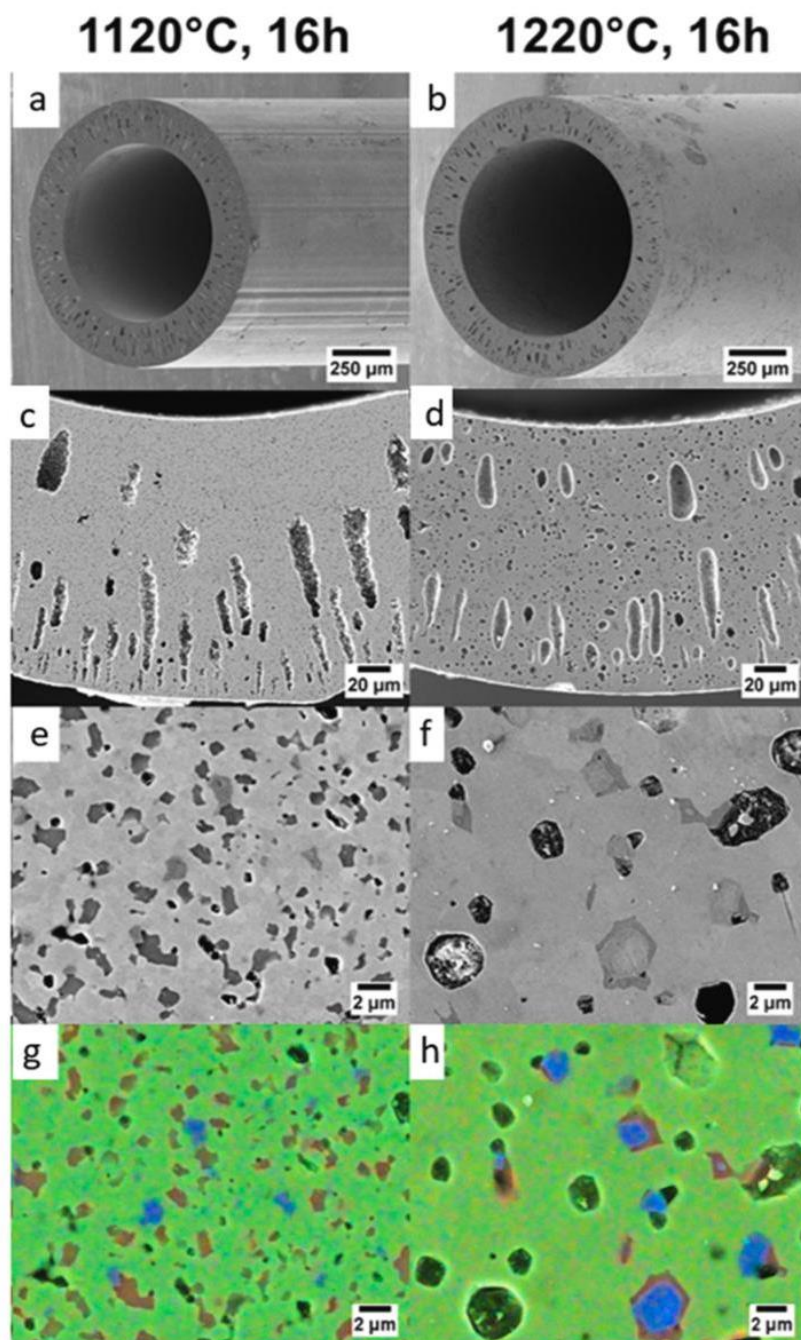
Fig. 2. SEM micrographs of LCCF hollow fiber spun with the $D_o = 2.0$ mm spinneret and sintered at different temperatures with polished cross-section (see Table 2). (a, b) Perspective views with secondary electrons at 2 kV, (c–f) top views on polished cross-section with secondary electrons at 20 kV. Black areas correspond to residual pores in which partly the pore wall is visible below the polished surface. (g, h) rainbow-colored overlay of secondary electron micrograph with elemental information as obtained from EDXS excited at 20 kV. Perovskite phase is dominated by green (La-Lα). Brownmillerite phase is dominated by red (Ca Kα). Spinel-type cobalt oxide phase is dominated by blue (Co Kα). (For interpretation of the references to color in this figure legend, the reader is referred to the web version of this article.)

fine structure is different from perovskite to brownmillerite with the features being consistent with the findings of Efimov et al. [8]. In addition, by EELS a signature of cobalt oxide was found, with an O-K near-edge fine structure typical for spinel-type Co_3O_4 [30] which is also consistent with Ref. [8].

For the perovskite, standardless quantification of EDX spectra acquired in the TEM gave atomic ratios La:Ca = 2.28 and Co:Fe = 4.02, which results in an approximate stoichiometry $La_{0.7}Ca_{0.3}Co_{0.8}Fe_{0.2}O_{3-\delta}$. For the brownmillerite, atomic ratios La:Ca = 0.223 and Co:Fe = 3.47 were observed, which correspond to an approximate stoichiometry $La_{0.2}Ca_{0.8}Co_{0.78}Fe_{0.22}O_{2.5\pm\delta}$. According to EDXS, these values are assumed to be within 2% accuracy. Stoichiometries were added to Table 3. The cobalt and iron composition is very similar in perovskite and brownmillerite, but there is substantial interdiffusion of lanthanum
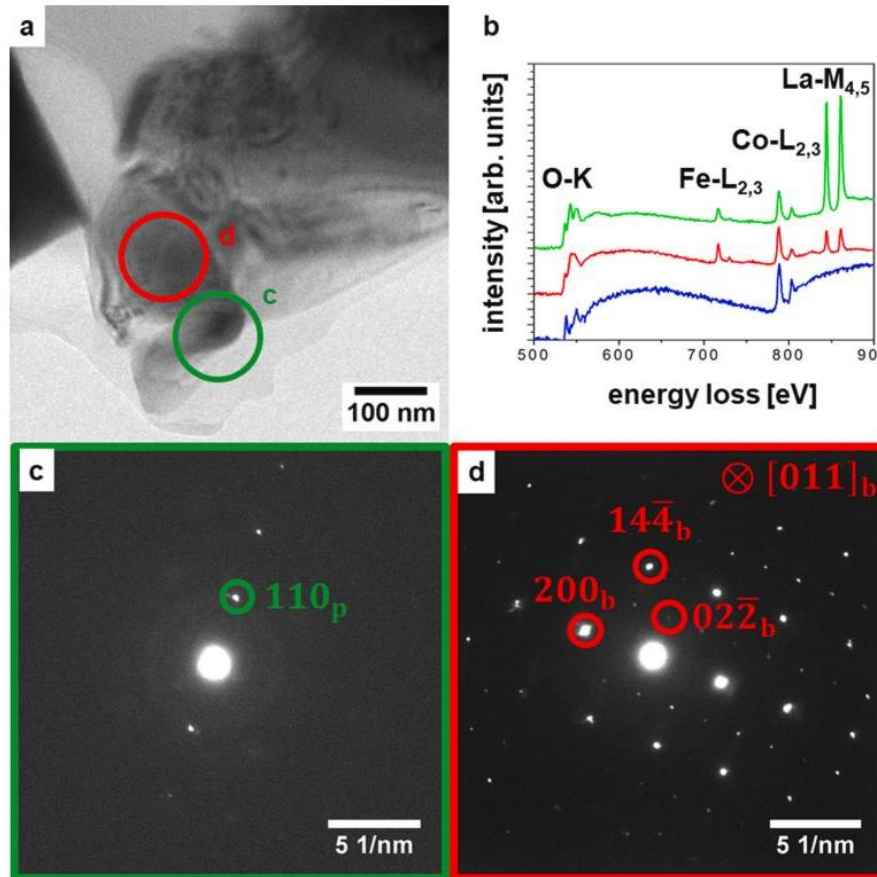
Fig. 3. TEM analysis of crushed hollow-fiber sintered at 1120 °C for 16 h. (a) TEM bright-field micrograph, (b) EEL spectra of perovskite (green), brownmillerite (red) and cobalt oxide (blue). (c, d) SAED pattern of the 120 nm circular areas indicated in a. (For interpretation of the references to color in this figure legend, the reader is referred to the web version of this article.)

Table 3
Details of Pawley analysis of crushed hollow-fiber sintered at 1120 °C for 16 h. The analysis resulted in a reliability factor $R_{wp} = 1.22$ and a goodness of fit $GOF = 1.94$.

Phase	Perovskite	Brownmillerite
stoichiometry (from TEM EDXS)	$La_{0.7}Ca_{0.3}Co_{0.8}Fe_{0.2}O_{3-\delta}$	$La_{0.2}Ca_{0.8}Co_{0.78}Fe_{0.22}O_{2.5\pm\delta}$
symmetry	rhombohedral	orthorhombic
space group	$R\bar{3}c$ (No. 167), hexagonal axes	Pbcm (No. 57)
lattice parameter a [Å]	5.4182863	5.1390904
lattice parameter b [Å]	5.4182863	11.0460268
lattice parameter c [Å]	13.2126101	14.8641002

and calcium between the two phases.

The cobalt oxide was too small in amount to be detected in XRD, but perovskite and brownmillerite are confirmed by this method. The experimental XRD shown in Fig. 4 as the black curve was analyzed by the Pawley method. It is composed of contributions of rhombohedral perovskite (green) and orthorhombic brownmillerite (red). For the analysis, the structural data as given in ICSD 190099 [29] (rhombohedral $LaCo_{0.8}Fe_{0.2}O_{3-\delta}$) and ICSD 169346 [31] (orthorhombic $Ca_2Fe_{1.07}Co_{0.93}O_5$) were taken as starting points. Despite the

interdiffusion of La and Ca between perovskite and brownmillerite as observed by EDXS and EELS in the TEM, the choice of these starting points was motivated by the effective ionic radii of La^{3+} (136 pm, [32]) and Ca^{2+} (134 pm, [32]) being almost identical in 12-fold coordination. In addition, the cobalt and iron contents of the starting structures are similar or close to the phases under study. However, for input lattice parameter a of the brownmillerite, a slightly smaller value was chosen according to the SAED observation (see Fig. 3). The Pawley analysis converged to the values given in Table 3. Efimov et al. [8] have shown that LCCF perovskite undergoes a phase transition from rhombohedral to cubic symmetry above 800 °C in air. Furthermore, Efimov et al. [8] show in a high temperature XRD measurement the reversible transformation of the rhomohedral to the cubic modification took place above 1173 K without a significant change of the volume per each formula unit. The cubic perovskite phase is relevant to the operational conditions of the hollow fiber membrane. Additionally, Efimov et al. [8] did experiments in an atmosphere containing 50 vol% N_2 and 50 vol% CO_2. The LCCF oxide remained stable at these conditions. This result is evidence of the high tolerance of the Ca containing perovskite materials against CO_2, as well as the desirable stability of LCCF at low oxygen partial pressures and temperatures between 303 and 1273 K.
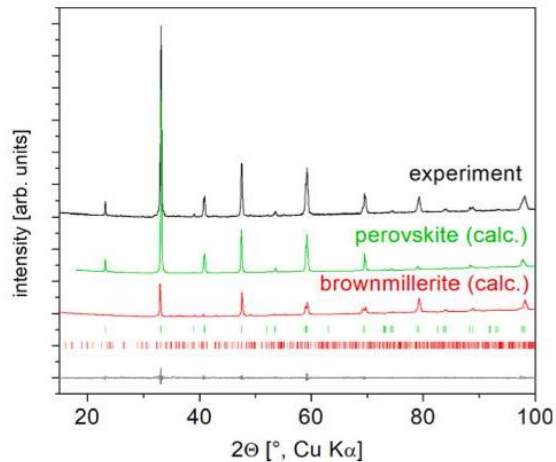
5

Fig. 4. Room-temperature XRD pattern and Pawley analysis from crushed hollow-fiber sintered at 1120 °C for 16 h. The observed (black) and calculated intensities of rhombohedral perovskite (green) and orthorhombic brownmillerite (red) together with the difference (gray) between the observed and calculated pattern as well as the possible reflection positions (tick marks) are given. Maximum of experimental main reflection is at about 115,000 counts. Curves are shifted vertically for clarity. (For interpretation of the references to color in this figure legend, the reader is referred to the web version of this article.)
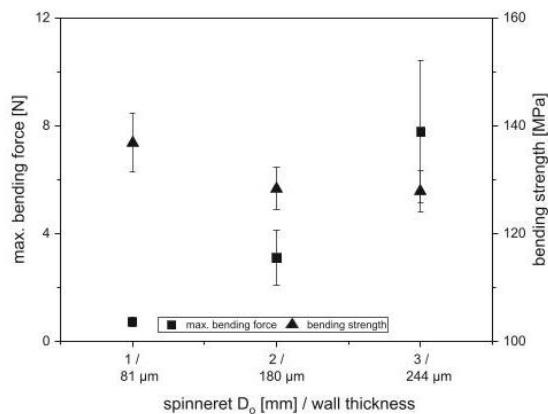
Fig. 5. Bending force and bending strength for LCCF fibers spun with different spinnerets.

3.2. Mechanical properties

The mechanical strength of the hollow fiber membranes manufactured with different spinnerets is shown in Fig. 5. Here, the maximum bending force and the bending strength are shown for the different membrane geometries. As expected, the hollow fibers with the thinnest wall (81 µm) has the lowest bending force (0.71 N), while the fibers with the thickest wall (244 µm) are the most stable (7.77 N). However, the bending strength of the thinnest hollow fiber (136.9 MPa) is slightly higher than the other two (128.3 MPa for 190 µm fiber, 127.9 MPa for the 244 µm fiber).

The mechanical strength of the fibers sintered at different temperatures is shown in Fig. 6. The lowest strength can be found for a sintering temperature of 1070 °C. At this temperature, the hollow fiber is still not gas-tight, which means that there is still some open porosity in the
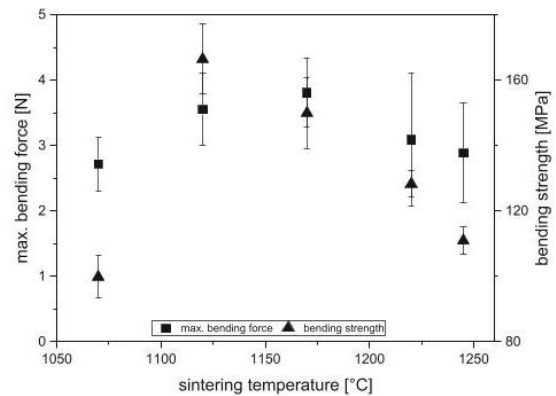
Fig. 6. Bending force and bending strength for LCCF-fibers at different sintering temperatures. All the fibers were spun with the spinneret $D_o = 2$ mm.
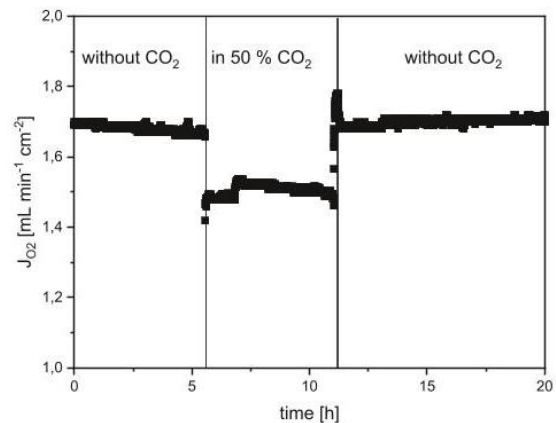
Fig. 7. Permeation of LCCF hollow fiber sintered at 1220 °C and spun with the spinneret $D_o = 2$ mm in CO_2 containing feed flow and without CO_2 containing feed flow. Conditions of the test: Sweep flow: 100 Nml min^{-1} N_2; Total Feed flow: 130 Nml min^{-1}, containing 30 Nml min^{-1} O_2. Pressure feed side: 2 bar, pressure sweep side: 1 bar. Temperature: 900 °C.

membrane which results in a lower mechanical strength. The highest bending strength is found at a sintering temperature of 1120 °C (166.5 MPa). With increasing sintering temperature, the bending strength decreases, which can be attributed to an increase of the grain size leading to an easier crack propagation.

3.3. Permeation results

The oxygen permeation of the LCCF hollow fiber sintered at 1220 °C and spun with the spinneret $D_o = 2$ mm at 900 °C is shown in Fig. 7. The difference between CO_2 containing feed and without CO_2 can be clearly seen. The permeation flux without CO_2 is 12% higher than with CO_2 containing feed. This decrease of the permeation was already described by Chen et al. [6]. It can be attributed to chemically adsorbed CO_2 at the oxygen vacancy sites of the membrane surface [6].

As mentioned above, the permeation through an MIEC membrane can depend on two rate limiting steps: the bulk diffusion and the surface exchange kinetics. To investigate the dominating step of oxygen transport through the LCCF hollow fiber membranes, fibers with different wall thicknesses were prepared. In Fig. 8, the permeation as a function of the different wall thicknesses is shown. The tested hollow fibers have

51
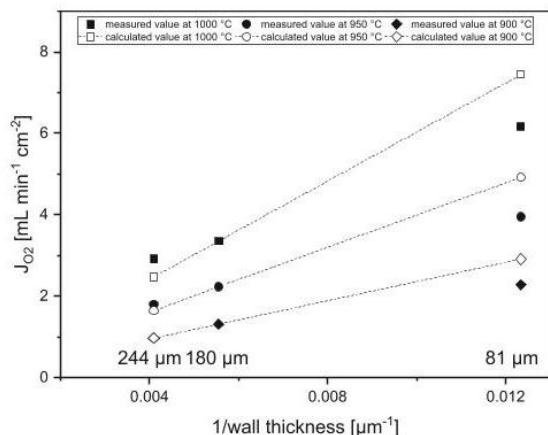
Fig. 8. Permeation of LCCF hollow fibers sintered at 1220 °C in dependence of the wall thickness at different temperatures (900 °C, 950 °C, 1000 °C). Additionally, the calculated values for a linear course in dependence of the 190 μm fiber. Conditions of the test: Sweep flow: 100 Nml min^{-1} N$_2$; Feed flow: 35 Nml min^{-1} N$_2$, 65 Nml min^{-1} CO$_2$, 30 Nml min^{-1} O$_2$. Pressure feed side: 2 bar, pressure sweep side: 1 bar.

Fig. 10. Arrhenius plot of the LCCF fibers sintered at 1220 °C with different wall thicknesses. The various symbols show the different wall thicknesses. Conditions of the test: Sweep flow 100 Nml min^{-1} N$_2$; Feed flow: 35 Nml min^{-1} N$_2$, 65 Nml min^{-1} CO$_2$, 30 Nml min^{-1} O$_2$. Pressure feed side: 2 bar, pressure sweep side: 1 bar.
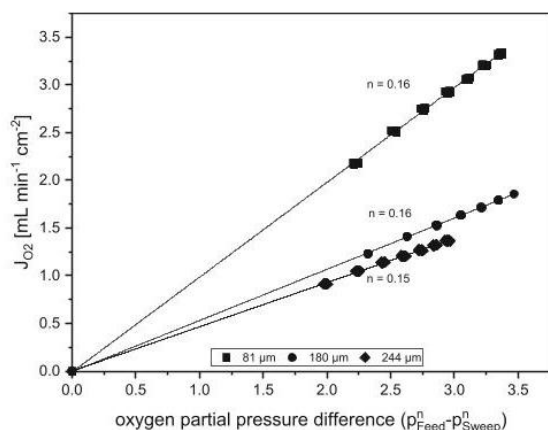
Fig. 9. Wagner plot for different wall thicknesses. In addition, the n values are calculated for the different wall thicknesses. Conditions of the test: Sweep flow 100 Nml min^{-1} N$_2$; temperature: 900 °C. Total feed flow: 100 Nml min^{-1}.

Fig. 11. Oxygen permeation flux as function of the sintering temperature. Measurements at different temperatures (900 °C, 950 °C and 1000 °C) in a 50% CO$_2$ atmosphere. Conditions of the test: Sweep flow 100 Nml min^{-1} N$_2$; Feed flow: 35 Nml min^{-1} N$_2$, 65 Nml min^{-1} CO$_2$, 30 Nml min^{-1} O$_2$. Pressure feed side: 2 bar, pressure sweep side: 1 bar.

wall thicknesses of 81 μm, 190 μm and 244 μm. The permeation was measured at 900 °C, 950 °C and 1000 °C in a 50% CO$_2$ atmosphere. As expected, the oxygen permeation increased with increasing temperature for all three hollow fibers. The permeation of the fiber with a wall thickness of 81 μm increases from 2.28 ml min^{-1} cm^{-2} (900 °C) up to 6.16 ml min^{-1} cm^{-2} (1000 °C).

Compared to literature data, this is the highest permeation in a CO$_2$ atmosphere ever measured. Before our findings, the highest permeation in a CO$_2$ atmosphere was measured by Kathiraser et al. [33] for La$_{0.6}$Sr$_{0.4}$Co$_{0.8}$Ga$_{0.2}$O$_{3-\delta}$ (LSCG) hollow fibers (2.4 ml min^{-1} cm^{-2}) at 950 °C [33]. The LCCF hollow fiber (81 μm wall thickness) measured in this study shows a significantly higher permeation of 3.94 ml min^{-1} cm^{-2} at 950 °C. Compared with other publications on LCCF membranes, our oxygen permeation is the highest. Salehi et al. [7] measured an oxygen permeation of 2.06 ml min^{-1} cm^{-2} for LCCF membranes in air at 900 °C [7]. Furthermore, an increase of the permeation with a decrease of the wall thickness can be noted. At 1000 °C, the permeation increases

by 179.3% with a decrease of the wall thickness from 244 μm to 81 μm. This finding suggests that the bulk diffusion has a significant influence on the permeation rate.

If bulk diffusion is the main influence on permeation, a linear dependency of permeation on the reciprocal wall thickness is to be expected. In Fig. 8, the theoretical values of the permeation in dependence of the measured value at 190 μm (unfilled marks) are calculated using this functionality. While the theoretical values fit quite well for the thicker wall (244 μm), there is a significant deviation for the thinner wall (81 μm). At 1000 °C, the theoretical oxygen permeation is about 27.6% larger than the measured one.

This mismatch can be explained by Fig. 9, where the Wagner plot for the different wall thicknesses is presented at 900 °C. In all three cases, the n value acc. to Eq. (1) is 0.15 and, therefore, n lies between 0 and 0.5. This means that the permeation is dominated by a mixed regime of bulk diffusion and surface exchange kinetics.

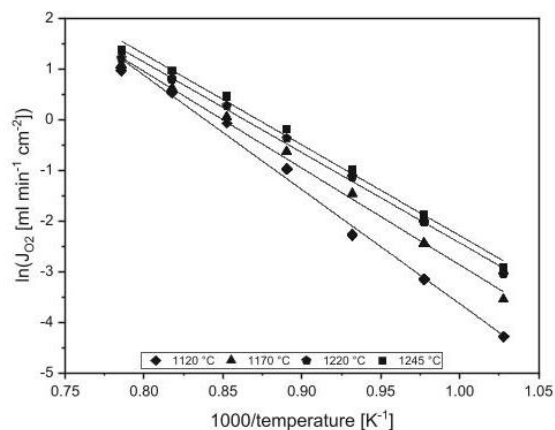The activation energies of the LCCF hollow fiber membranes were

Fig. 12. Arrhenius plot of the oxygen fluxes through LCCF fibers sintered at different temperatures. Conditions of the test: Sweep flow 100 Nml min^{-1} N$_2$; Feed flow: 35 Nml min^{-1} N$_2$, 65 Nml min^{-1} CO$_2$, 30 Nml min^{-1} O$_2$. Pressure feed side: 2 bar, pressure sweep side: 1 bar.

determined from an Arrhenius plot, as given in Fig. 10. The thinnest fiber (81 µm) has an activation energy of 140.3 kJ mol^{-1}, the fiber with 190 µm 148.3 kJ mol^{-1} and the thickest fiber (244 µm) 160.4 kJ mol^{-1}. The smaller wall thickness has a positive influence to the activation energy. Efimov et al. [8] and Salehi et al. [7] also found higher activation energies for LCCF membranes with a higher thickness comparing membranes with thicknesses between 1 mm and 10 µm [7,8]. They reported values of the activation energy of 137 kJ mol^{-1} (1 mm) and 65 kJ mol^{-1} (10 µm). The big difference in the activation energy was explained by the change of the rate limiting step from bulk diffusion to surface exchange kinetics. Furthermore, Stevenson et al. [5] reported an activation energy of 180 kJ mol^{-1} for 1 mm thick LCCF membranes [5]. The discrepancy of the activation energy compared to the literature can be explained by the different measurement conditions. In this work, a 50% CO$_2$ atmosphere is used as feed gas, a larger temperature range (700–1000 °C) is used and the geometry of the membrane is different (hollow fiber).

The oxygen permeation measurements of membranes sintered at different temperatures are shown in Fig. 11. The membrane sintered at 1120 °C exhibited the lowest permeation flux of 2.61 ml min^{-1} cm^{-2} at 1000 °C. With an increase of the sintering temperature, the permeation rate linearly increases up to 3.92 ml min^{-1} cm^{-2} for a sintering temperature of 1245 °C. This is an increase of 33.4%. For LCCF hollow fibers, the oxygen flux is governed by oxygen diffusion through the membrane bulk. The grain boundaries act as oxygen diffusion barriers.

Values of the activation energy of LCCF hollow fiber membranes sintered at different temperatures were determined from an Arrhenius plot, as given in Fig. 12. The activation energy decreases with increasing sintering temperatures from 187 kJ mol^{-1} to 148 kJ mol^{-1}.

4. Conclusions

In this work, the perovskite LCCF6482 (La$_{0.4}$Ca$_{0.6}$Co$_{0.8}$Fe$_{0.2}$O$_{3-\delta}$), which is well known to be CO$_2$ tolerant, was used to manufacture hollow fiber membranes. By a variation of spinning and sintering conditions, the performance of these membranes was optimized.

Hollow fibers with wall thicknesses in a range of 81–244 µm were developed by using different spinneret geometries. Furthermore, the grain size of the sintered fibers could be controlled by varying the sintering temperature.

Microstructure analysis by SEM, TEM and XRD show that the LCCF phase contains different amounts of brownmillerite and a spinel-type

cobalt oxide phase as foreign phases, depending on the sintering temperatures. With increasing sintering temperatures, above 1200 °C the brownmillerite phase enwraps the cobalt oxide inclusions.

By decreasing the wall thickness to 81 µm, the oxygen permeation increased up to 6.16 ml min^{-1} cm^{-2} at 1000 °C. This is the highest value ever published for LCCF membranes and for hollow fibers measured in a 50% CO$_2$ containing feed atmosphere.

Since the oxygen permeation increases with increasing grain size, this finding leads to the conclusion that the oxygen flux is influenced by oxygen diffusion through the membrane bulk. An increase in grain size is accompanied by a decrease in grain boundaries. Therefore, grain boundaries in LCCF membranes act as barriers for the oxygen diffusion and thus for the oxygen permeation.

However, both the n-value of the Wagner plot and a plot of permeation as a function of the inverse wall thickness indicate that oxygen transport is affected by both bulk diffusion and surface exchange kinetics.

As the mechanical strength also plays an important role in the application of such membranes, an improvement of permeation by a further decrease of wall thickness is limited. For further improvement, the surface exchange kinetics has to be optimized.

With this study, optimized perovskite hollow fiber membranes are available combining high oxygen permeation with a high CO$_2$-tolerance.

CRediT authorship contribution statement

Frederic Buck: Conceptualization, Investigation, Methodology, Writing - original draft, Validation. **Armin Feldhoff:** Investigation, Writing - review & editing. **Jürgen Caro:** Writing - review & editing, Supervision. **Thomas Schiestel:** Conceptualization, Resources, Writing - review & editing, Supervision, Project administration, Funding acquisition.

Declaration of Competing Interest

The authors declare that they have no known competing financial interests or personal relationships that could have appeared to influence the work reported in this paper.

Acknowledgments

References

[1] F. Schüth, R.A. Eichel, Energiespeicher für die Zukunft, Phys. J. 13 (2014) 31–36.
[2] G. Chen, et al., A novel plasma-assisted hollow fiber membrane concept for efficiently separating oxygen from CO in a CO$_2$ plasma, Chem. Eng. J. 392 (2019) 123699, https://doi.org/10.1016/j.cej.2019.123699.
[3] F. Buck, et al., Einsatz von perowskitischen Hohlfasermembranen in einem Mikrowellenplasma. Use of Perovskite hollow fiber membranes in a microwave plasma, Chemie Ingenieur Technik 91 (2019) 1117–1122, https://doi.org/10.1002/cite.201900048.
[4] Y. Teraoka, T. Nobunaga, N. Yamazoe, Effect of cation substitution on the oxygen semipermeability of perovskite-type oxides, Chem. Lett. 17 (1988) 503–506, https://doi.org/10.1246/cl.1988.503.
[5] J. Stevenson, et al., Electrochemical properties of mixed conducting perovskites La$_{1-x}$ M$_x$Co$_{1-y}$ Fe$_y$O$_{3-\delta}$ (M=Sr, Ba, Ca), J. Electrochem. Soc. 143 (1996) 2722, https://doi.org/10.1149/1.1837098.
[6] G. Chen, et al., High flux and CO$_2$-resistance of La$_{0.6}$Ca$_{0.4}$Co$_{1-x}$Fe$_x$O$_{3-\delta}$ oxygen-transporting membranes, J. Membr. Sci. 590 (2019) 117082, https://doi.org/10.1016/j.memsci.2019.05.007.
[7] M. Salehi, et al., Oxygen permeation and stability study of (La$_{0.6}$Ca$_{0.4}$)$_{0.98}$(Co$_{0.8}$Fe$_{0.2}$)O$_{3-\delta}$ membranes, J. Membr. Sci. 542 (2017) 245–253, https://doi.org/10.1016/j.memsci.2017.07.050.
[8] K. Efimov, et al., Ca-containing CO$_2$-tolerant perovskite materials for oxygen separation, J. Membr. Sci. 389 (2012) 205–215, https://doi.org/10.1016/j.memsci.2011.10.030.

[9] J. Caro, et al., Evaluation of perovskites in hollow fibre and disk geometry in catalytic membrane reactors and in oxygen separators, Catal. Today 118 (2006) 128–135, https://doi.org/10.1016/j.cattod.2005.12.015.

[10] H.J. Bouwmeester, H. Kruidhof, A. Burggraaf, Importance of the surface exchange kinetics as rate limiting step in oxygen permeation through mixed-conducting oxides, Solid State Ionics 72 (1994) 185–194, https://doi.org/10.1016/0167-2738 (94)90145-7.

[11] H.J. Bouwmeester, et al., Oxygen semipermeability of erbia-stabilized bismuth oxide, Solid State Ionics 53 (1992) 460–468, https://doi.org/10.1016/0167-2738 (92)90416-M.

[12] S. Carter, et al., Oxygen transport in selected nonstoichiometric perovskite-structure oxides, Solid State Ionics 53 (1992) 597–605, https://doi.org/10.1016/ 0167-2738(92)90435-R.

[13] J.F. Vente, W.G. Haije, Z.S. Rak, Performance of functional perovskite membranes for oxygen production, J. Membr. Sci. 276 (2006) 178–184, https://doi.org/ 10.1016/j.memsci.2005.09.046.

[14] P.-M. Geffroy, et al., Understanding and identifying the oxygen transport mechanisms through a mixed-conductor membrane, Chem. Eng. Sci. 162 (2017) 245–261, https://doi.org/10.1016/j.ces.2017.01.006.

[15] P.-M. Geffroy, et al., Rational selection of MIEC materials in energy production processes, Chem. Eng. Sci. 87 (2013) 408–433, https://doi.org/10.1016/j. ces.2012.10.027.

[16] P.-M. Geffroy, et al., The impact of experimental factors on oxygen semi-permeation measurements, J. Electrochem. Soc. 160 (2012) F60, https://doi.org/ 10.1149/2.068301jes.

[17] C. Li, et al., Modelling of oxygen transport through mixed ionic-electronic conducting (MIEC) ceramic-based membranes: an overview, J. Membr. Sci. 567 (2018) 228–260, https://doi.org/10.1016/j.memsci.2018.09.016.

[18] H.J. Bouwmeester, A.J. Burggraaf, Dense ceramic membranes for oxygen separation, Membr. Sci. Technol. 4 (1996) 435–528, https://doi.org/10.1016/ S0927-5193(96)80013-1.

[19] X. Zhu, et al., Permeation model and experimental investigation of mixed conducting membranes, AIChE J. 58 (2012) 1744–1754, https://doi.org/10.1002/ aic.12710.

[20] S.J. Xu, W.J. Thomson, Oxygen permeation rates through ion-conducting perovskite membranes, Chem. Eng. Sci. 54 (1999) 3839–3850, https://doi.org/ 10.1016/S0009-2509(99)00015-9.

[21] X. Zhu and W. Yang, Mixed conducting ceramic membranes, Springer, Germany, 2017. https://doi.org/10.1007/978-3-662-53534-9 https://doi.org/10.1002/ aic.12710.

[22] S. Saher, et al., Grain-size dependence of the deterioration of oxygen transport for pure and 3 mol% Zr-doped $Ba_{0.5}Sr_{0.5}Co_{0.8}Fe_{0.2}O_{3-\delta}$ induced by thermal annealing, J. Mater. Chem. A 5 (2017) 4982–4990, https://doi.org/10.1039/C6TA10454A.

[23] V. Kharton, et al., Ceramic microstructure and oxygen permeability of SrCo (Fe, M) $O_{3-\delta}$ (M= Cu or Cr) perovskite membranes, J. Electrochem. Soc. 145 (1998) 1363–1373, https://doi.org/10.1149/1.1838467.

[24] J. Martynczuk, M. Arnold, A. Feldhoff, Influence of grain size on the oxygen permeation performance of perovskite-type $(Ba_{0.5}Sr_{0.5})(Fe_{0.8}Zn_{0.2}) O_{3-}$ δmembranes, J. Membrane Sci. 322 (2008) 375–382, https://doi.org/10.1016/j. memsci.2008.05.064.

[25] M. Reichmann, et al., Impact of microstructure on oxygen semi-permeation performance of perovskite membranes: understanding of oxygen transport mechanisms, J. Power Sources 324 (2016) 774–779, https://doi.org/10.1016/j. jpowsour.2016.06.009.

[26] S. Diethelm, J. Sfeir, P. Buffat, Correlation between oxygen transport properties and microstructure in $La_{0.5}Sr_{0.5}FeO_{3-\delta}$, J. Eur. Ceram. Soc. 25 (2005) 2191–2196, https://doi.org/10.1016/j.jeurceramsoc.2005.03.028.

[27] P. Zeng, et al., Significant effects of sintering temperature on the performance of $La_{0.6}Sr_{0.4}Co_{0.2}Fe_{0.8}O_{3-\delta}$ oxygen selective membranes, J. Membr. Sci. 302 (2007) 171–179, https://doi.org/10.1016/j.memsci.2007.06.047.

[28] T. Schiestel, et al., Hollow fibre perovskite membranes for oxygen separation, J. Membr. Sci. 258 (2005) 1–4, https://doi.org/10.1016/j.memsci.2005.03.035.

[29] N. Proskurina, et al., Phase equilibria and structure of solid solutions in the La–Co–Fe–O system at 1100 C, Inorg. Mater. 40 (2004) 955–959, https://doi.org/ 10.1023/B:INMA.0000041328.85504.3d.

[30] M. Bittner, et al., Porous $Ca_3Co_4O_9$ with enhanced thermoelectric properties derived from Sol-Gel synthesis, J. Eur. Ceram. Soc. 37 (2017) 3909–3915, https:// doi.org/10.1016/j.jeurceramsoc.2017.04.059.

[31] F. Ramezanipour, et al., Intralayer cation ordering in a brownmillerite superstructure: synthesis, crystal, and magnetic structures of Ca_2FeCoO_5, Chem. Mater. 22 (2010) 6008–6020, https://doi.org/10.1021/cm1023025.

[32] R.D. Shannon, Revised effective ionic radii and systematic studies of interatomic distances in halides and chalcogenides, Acta Crystall. Sect. A: Crystal Phys., Diffract., Theor. General Crystall. 32 (1976) 751–767, https://doi.org/10.1107/ S0567739476001551.

[33] Y. Kathiraser, et al., Oxygen permeation and stability study of $La_{0.6}Sr_{0.4}Co_{0.8}Ga_{0.2}O_{3-\delta}$ (LSCG) hollow fiber membrane with exposure to CO_2, CH_4 and He, J. Membr. Sci. 427 (2013) 240–249, https://doi.org/10.1016/j. memsci.2012.09.014.

54

5. Improvement of the oxygen transport mechanism of LCCF hollow fiber membranes

5.1. Summary

After the optimization of the bulk diffusion in the previous chapter, the focus of this paper is on further improvement of the oxygen permeation through LCCF hollow fiber membranes. The paper focuses on the one hand side on the manufacturing of asymmetric hollow fibers with a porous support and a thin dense layer and on the other hand on a surface modification of dense hollow fibers via surface etching with H_2SO_4.

The sintering temperature of the porous support was varied to find a good compromise between mechanic stability and porosity. The dip coating process, to apply the dense layer to the porous support, was optimized to produce a thin dense layer by varying the coating velocity. The microstructure was analysed by SEM images.

Hollow fiber membranes with an outer diameter of 1.13 mm and a dense layer of 22 µm could be manufactured. The oxygen permeation reached up to 5.10 ml min^{-1} cm^{-2} at 1000 °C. In comparison to dense hollow fibers with different wall thicknesses (179 µm and 73 µm) the dense coated hollow fiber membrane showed an increase of oxygen permeation of 68.6 % (compared to 179 µm) and 4.7 % (compared to 73 µm). The relative low increase of 4.7 % can be explained by the 86.4 % smaller grain areas even though the fiber was sintered at the same temperature. The n-value of the Wagner equation increased with decreasing wall thickness, but is still in the mixed regime.

For the surface modification tests, hollow fiber membranes, sintered at 1220 °C, were etched for different times (20 min, 60 min and 180 min) at different surfaces (inner, outer and both). The acidic solutions were analysed with ICP-MS and ICP-OES to investigate which components were favourably dissolved. The hollow fiber, etched at both surfaces for 180 min, showed the highest oxygen permeation flux (5.9 ml min^{-1} cm^{-2} at 1000 °C).

5.2. High-flux CO_2 stable oxygen-transport membranes through surface engineering

Frederic Buck, Osman Bunjaku, Jürgen Caro, Thomas Schiestel

High-flux CO_2-stable oxygen transport hollow fiber membranes through surface engineering

F. Buck[a,b], O. Bunjaku[a], J. Caro[b], T. Schiestel[a,*]

[a] Fraunhofer Institute for Interfacial Engineering and Biotechnology IGB, 70569 Stuttgart, Germany

[b] Institute of Physical Chemistry and Electrochemistry, Leibniz Universität Hannover, 30167 Hannover, Germany

*Thomas.schiestel@igb.fraunhofer.de

Abstract

The influences of bulk diffusion and surface exchange on oxygen transport of $(La_{0.6}Ca_{0.4})(Co_{0.8}Fe_{0.2})O_{3-\delta}$ (LCCF) hollow fiber membranes were investigated. As an outcome, two strategies for increasing the oxygen permeation were pursued. First, porous LCCF hollow fibers as support were coated with a 22 µm dense LCCF separation layer through dip coating and co-sintering. The oxygen permeation of the porous fiber with dense layer reached up to 5.10 ml min^{-1} cm^{-2} at 1000 °C in a 50 % CO_2 atmosphere. Second, surface etching of dense LCCF hollow fibers with H_2SO_4 was applied. The surface etching of both inner and outer surfaces leads to a permeation improvement up to 86.0 %. This finding implies that the surface exchange reaction plays a key role in oxygen transport through LCCF hollow fibers. A good long-term (> 250 h) stability of the asymmetric hollow fiber in a 50% CO_2 atmosphere was found at 900 °C.

Keywords

Oxygen separation, mixed ionic electronic conductor, surface modification, asymmetric hollow fiber membrane

1. Introduction

Since the Paris agreement in 2015, many efforts to produce green energy from renewable sources were made to prevent a temperature rise larger than 1.5 °C [1]. For example, the installed power of solar cells increased from 23 GW (2009) to 627 GW (2019) [2]. One big challenge is the fluctuation of the renewable energy. Therefore, technologies to store or to convert this excess energy are urgently needed. A possible approach for the energy surplus is a combined plasma-membrane reactor, which was first mentioned by Chen et al. [3]. They showed that with a microwave induced plasma torch, CO_2 can dissociate into oxygen and CO due to $CO_2 \leftrightarrows CO + \frac{1}{2} O_2$. During the plasma process, the oxygen can be separated in situ

through mixed ionic electronic conductor (MIEC) hollow fiber membranes. The remaining CO can be used as a platform chemical for the synthesis of high-value hydrocarbons. The requirements for MIEC membranes in a CO_2 plasma are challenging: A high oxygen permeation in combination with good thermal and CO_2 stability.

In the last decade, the development of MIEC perovskite oxides have attracted much attention [4-8]. An interesting perovskite is $(La_{0.6}Ca_{0.4})(Co_{0.8}Fe_{0.2})O_{3-\delta}$ (LCCF), which was first mentioned by Teraoka et al. [9]. In different publications the long-term stability in CO_2 and the good temperature turnover resistance was shown [10-14]. However, LCCF has relatively low oxygen permeability compared to membranes made from high performance materials like $Ba_{0.5}Sr_{0.5}Co_{0.8}Fe_{0.2}O_{3-\delta}$ [15] or $BaCo_xFe_yZr_zO_{3-\delta}$ [16]. A number of factors such as sweep gas flow, operating temperature and the membrane properties itself, like morphology, geometric form, wall thickness and chemistry of materials, can influence the oxygen permeation [17,18]. The transport through the membrane is dominated either by the surface exchange reactions or by the bulk diffusion [19]. Many publications deal with the optimization of membranes by surface modification to improve the surface exchange reactions or by reducing the wall thickness thus shortening the bulk diffusion length [20-26].

To improve the surface exchange reactions the oxygen adsorption respectively desorption can be optimized by increasing the surface area [27-29]. In some cases, an extra layer of porous material like palladium or other perovskites was added via dip coating or electroless plating [27,30-32]. Another interesting method is the surface etching. Liu et al. [33] first mentioned the surface etching of $La_{0.6}Sr_{0.4}Co_{0.2}Fe_{0.8}O_3$ (LSCF) hollow fibers with sulphuric and hydrochloric acid. The modified structure showed an oxygen flux up to 20 times higher. Wang et al. [34] also used the surface etching method for LSCF hollow fibers with different concentrations of sulphuric acid and hydrochloric acid. The dense surface of the hollow fiber is converted into a porous structure. This new structure not only increases the surface area for an enhanced surface exchange reaction but it can also reduce the thickness of the dense layer and thus the transport resistance for the bulk diffusion.

Another possibility to increase the oxygen permeation is the preparation of asymmetric membranes, which consist of a thin dense layer on a porous support. However, the decrease of the membrane thickness has a negative influence on the mechanical stability and can cause failure during operation. Up to now, many studies have focused on the fabrication of asymmetric disc membranes by different coating methods such as dip coating, spray coating, sputtering or other techniques [5, 28, 35-39]. The thick porous support can improve the mechanical strength as well as the surface exchange reactions by increasing the surface area.

The manufacturing of asymmetric disk membranes is much easier compared to asymmetric hollow fiber membranes. On the other hand, for hollow fibers the scale up is easier and the edge leakage effect is irrelevant [40].

In our latest publication [41], the influence of the wall thickness and the sintering temperature on the oxygen permeation of LCCF hollow fiber membranes was examined. Dense hollow fibers with a wall thickness of 81 µm could be manufactured by wet spinning and sintering. The decrease of the wall thickness showed an increase of the oxygen permeation but it also showed that the oxygen transport is still dominated by both the bulk diffusion as well as the surface exchange reactions. The calculation of the dominating transport mechanism was made by the Wagner equation [19]:

$$J_{O2} = \frac{\sigma_i^0 RT}{16F^2\, n\, L}(p_1^n - p_2^n) \tag{1}$$

with R as the gas constant, J_{O2} as the oxygen permeation, L as the membrane thickness, F as the Faraday constant, T as the temperature, σ_i^0 the ionic conductivity at standard conditions, p_1 as the oxygen partial pressure at the high pressure side and p_2 as the low pressure side and n as the fit parameter which can be derived from the experimental data. For $n \geq 0.5$, the surface exchange reaction limits the oxygen flux; for $n < 0$, bulk diffusion dominates and for $0 < n < 0.5$, the oxygen permeation is influenced by a mixed regime.

The aim of this paper is to optimize the oxygen transport through a LCCF hollow fiber membrane by two different methods. The first method is the preparation of a thin dense LCCF layer on a porous LCCF support to reduce the influence of bulk diffusion. The second method is the surface etching, which primarily increases the roughness of the surface and, therefore, the surface exchange reactions. The findings of this work can be used to further optimize the performance of LCCF membranes with regard to material saving and to increase the permeance, especially for the extraction of oxygen from a CO_2 plasma gas.

2. Material and methods

2.1. Hollow fiber preparation

The perovskite powder $(La_{0.6}Ca_{0.4})(Co_{0.8}Fe_{0.2})O_{3-\delta}$ (LCCF) was prepared by Cerpotech (Tiller, Norway) via a spray pyrolysis process. The manufacturing of the asymmetric hollow fiber can be separated in five steps (Fig. 1): Preparation of the spinning solution, the wet spinning process, the preparation of the coating suspension, the coating, and the sintering.

The following nomenclature is used for the LCCF hollow fibers prepared:

- p-LCCF: Porous LCCF hollow fibers which are prepared by the addition of a porogen (rice starch) to the spinning solution and are sintered at low temperature (1170 °C) to avoid densification.
- c-LCCF: Coated LCCF hollow fibers are prepared by dip coating of p-LCCF green fibers with an LCCF suspension and are sintered at low temperature (1170 °C) to prepare only a thin dense layer on a porous support.
- d-LCCF: Dense LCCF hollow fibers are prepared by wet spinning and are sintered at high temperature (1220 °C) to get a completely dense membrane wall.
- e-LCCF: Etched LCCF hollow fibers are prepared by etching d-LCCF (1220 °C) with sulphuric acid inside and/or outside.

The conditions for the preparation of the different fibers are summarized in Tables 1, 2 and 3.

The spinning solution for the porous hollow fiber consists of 51.5 % LCCF, 5.8 % Polyetherimide (PEI, Merck KGaA, Darmstadt, Germany), 36.7 % N-Ethyl-2-Pyrrolidon (NEP, ≥98 %, Carl Roth GmbH + Co. KG, Karlsruhe, Germany) and 6 % rice starch (Merck KGaA, Darmstadt, Germany) and was ball milled for 48 h at 170 U min^{-1}. The spinning solution for the dense hollow fiber has the same composition except of the rice starch.

The non-solvent induced phase inversion process was used to manufacture stable green fibers by phase inversion spinning which is described in details elsewhere [11]. The external coagulant was deionised (DI) water and a mixture of DI water/NEP (25 vol%/ 75 vol%) was used as bore fluid. The porous hollow fibers were spun with a spinneret of D_o/D_i 2.0/1.2 mm. For the dense hollow fibers (without rice starch) two different fibers were spun with a spinneret of D_o/D_i 2.0/1.2 mm and D_o/D_i 1.0/0.5 mm to manufacture hollow fibers with different wall thicknesses. The coating suspension consists of 31 % LCCF (ball milled for 24 h at 250 U min^{-1}), 2.6 % PVP (Merck KGaA, Darmstadt, Germany) and 66.4 % Ethanol (≥98 %, Th. Geyer GmbH & Co. KG, Renningen, Germany). The suspension was deposited by dip coating on 60 cm long green hollow fibers. The coated green fibers were than sintered at 1170 °C for 16 h. All manufacturing parameters are shown in Table 1.
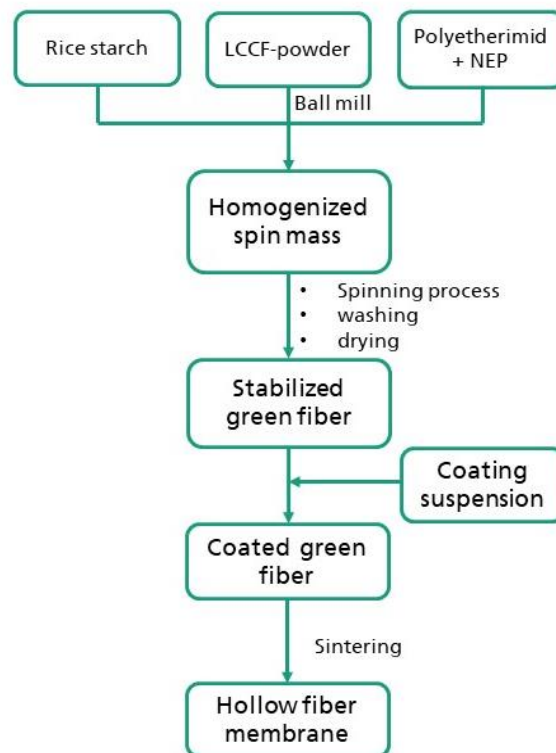
Fig. 1. Manufacturing principle of asymmetric LCCF perovskite hollow fibers.

Table 1**:** Parameters for the wet spinning of LCCF hollow fiber membranes.

Name	p-LCCF	d-LCCF
Spinneret: D_o/D_i [mm]	2.0 / 1.2	1.0 / 0.5 & 2 .0 / 1.2
Dope composition [wt%]:		
• LCCF	51.5	58.0
• PEI	5.8	7.6
• NEP	36.7	34.4
• Rice starch	6.0	0.0
Spinning parameters:		
• Bore liquid – DI water/NEP [vol%]	25 / 75	
• Flow rate of the bore liquid [ml min^{-1}]	7.5	
• External coagulant	DI Water	
• Air gap [cm]	0	
Standard sintering parameters:		
• Temperature [°C]	1170	1220
• Time [h]	16	16

Table 2: Parameters for the coating of p-LCCF hollow fibers to prepare c-LCCF membranes.

Base hollow fiber	p-LCCF (green)
Slurry composition [wt%]: • LCCF • PVP • Ethanol	 31.0 2.6 66.4
Coating parameters: • Velocity [cm s^{-1}] • Dwelling time [s]	 0.5 – 5.0 0
Standard sintering parameters: • Temperature [°C] • Time [h]	 1170 16

2.2. **Surface modification of compact LCCF hollow fibers through surface etching**

The preparation of e-LCCF hollow fibers was achieved through modification of the surface of d-LCCF fibers by chemical etching with sulphuric acid (H_2SO_4, $\geq$ 98 %, Bernd Kraft GmbH, Duisburg, Germany). For the etching of the outer surface, the hollow fibers with a length of 30 cm were sealed with a polymer resin at both ends and then immersed in 25 ml H_2SO_4 in a glass tube for a prescribed time [33]. The reacted fiber was rinsed five times with DI water and dried at 100 °C in an oven. For the etching of the inner surface of the hollow fiber, it was connected to a funnel, filled with H_2SO_4. The acid flow rate was controlled by a valve and by the weight of the collected amount of H_2SO_4 in a beaker. To modify both surfaces, firstly the outer surface was etched and then the inner surface with the previously described methods. The modified surfaces and the etching time of the different e-LCCF hollow fibers are summarized in Table 3.

Table 3: Parameters for the etching of d-LCCF hollow fibers to prepare e-LCCF membranes.

Base hollow fiber	d-LCCF
Etching agent	H_2SO_4, $\geq$ 98 %
Etching parameters: • Temperature • Time [min]	 RT 20 – 180
Etching surfaces	1. Inside 2. Outside 3. Inside & Outside

2.3. **Characterisation of the LCCF hollow fibers**

The morphological features of the prepared membranes were examined using a scanning electronic microscope (SEM) of the type GeminiSEM500 (Carl Zeiss Microscopy Deutschland GmbH, Oberkochen, Germany). The SEM was equipped with two energy dispersive X-ray (EDX) detectors (XFlash and FlatQuad, Fa. Bruker Nano, Berlin, Germany). The grain area distribution was statistically calculated by manual measurements of the area of individual grains, based on the SEM micrographs. For each fiber the area of 150 particles was registered. The mechanical stability was measured with the four point-bending test (Zwick/Roell Z0005, Ulm, Germany). The porosity of the uncoated hollow fiber was calculated with a porometer type IG-FT Porolux 1000 (Porotec GmbH, Hofheim am Taunus, Germany). Furthermore, the composition of the etching solutions was analysed with inductively coupled plasma mass spectrometry (ICP-MS), type Triple Quadrupole 8900 (Agilent Technologies, Santa Clara, USA) and inductively coupled plasma optical emission spectrometry (ICP-OES), type Plasma Quant PQ 9000 Elite (Analytik Jena GmbH, Jena, Germany). Previous to the permeation tests, the gas-tightness of the LCCF fibers needs to be tested. Therefore, the coated hollow fibers were sealed with polymer resin at one end. Then the fiber was connected to a pressure hose. The pressure was set up to 4 bar, then the fiber was immersed into water to check if there are any bubbles as indicator for leakage.

2.4. **Oxygen permeation tests**

A detailed description of the set up to measure the oxygen permeation of LCCF hollow fibers in an oven can be found in details elsewhere [42]. The feed flow, consisting of CO_2, O_2 and N_2, was injected inside the lumen of the hollow fiber. The N_2 sweep flow was outside of the hollow fiber in counter current mode. The sweep flow was kept constant at 100 Nml min^{-1} for all the measurements. In the experiments with temperature variation, the feed flow was constant at 130 Nml min^{-1} with a composition of 50 % CO_2, 23 % O_2 and 27 % N_2. In these experiments, the temperature was reduced in 50 K steps starting at 1000 °C until 700 °C. For the calculation of the dominating transport mechanism, the feed flow was constant at 100 Nml min^{-1} with a varying composition of O_2 and CO_2 and the temperature was kept constant at 900 °C. For all measurements, the pressure on the feed side was 2 bar and 1 bar on the sweep side. The oxygen concentration in the feed as well as in the sweep was measured with an oxygen analyser (Zirox SGM 7). To ensure isothermal conditions, the hollow fibers were coated three times with a gold paste on both ends and sintered at 950 °C for 6 h to obtain a defined 1 cm long permeation zone

in the middle of the oven. The oxygen permeation J_{O2} (ml cm^{-2} min^{-1}) can be calculated with the following equation [42]:

$$J_{O2} = \frac{c_{O2} \cdot \dot{V}_s}{A_{membrane}} \qquad (2)$$

with $\dot{V}_s$ as sweep flow (ml min^{-1}), c_{O2} as the oxygen concentration on the sweep side (vol %), and $A_{membrane}$ as the membrane area (cm^2). To calculate the membrane area, the logarithmic mean of the hollow fiber was used:

$$A_{membrane} = \frac{\pi \cdot L \cdot (D_o - D_i)}{ln\left(\frac{D_o}{D_i}\right)} \qquad (3)$$

with D_i as inner and D_o as outer diameter of the hollow fiber and the effective membrane length L.

3. Results and discussion

3.1. Influence of the sintering temperature on the porous LCCF support

Uncoated green p-LCCF hollow fibers were sintered at different temperatures T_S (1100 °C, 1120 °C and 1170 °C) to study the interplay of mechanical stability, shrinkage, nitrogen permeance and average pore size.

Table 4 summarizes the results for the different sintering temperatures (T_s). The temperature influence on the outer diameter (D_o) of the fibers is negligible small. A bigger influence can be seen regarding the nitrogen permeance, the average pore size (Θ) and the mechanical stability. As expected, with increasing sintering temperature, the nitrogen permeance and the pore size decrease, and contrary the max. bending force (F_B) and the bending strength (σ_B) increase. In this study, the sintering temperature was fixed at 1170 °C as this temperature seems to be the best compromise between high mechanical strength and good porosity. The nitrogen permeance of the porous fibers sintered at 1170 °C is more than 36 times higher than the highest oxygen permeance of a dense LCCF fiber (6.16 ml min^{-1} cm^{-2} at 1000 °C [41]). As described in our previous publication [41], higher sintering temperatures have a positive influence on the oxygen

permeation, but a further increase of the sintering temperature is not advantageous since densification of the LCCF hollow fibers starts.

Table 4: Characteristics of the porous p-LCCF fibers sintered at different temperatures.

T_S	D_o	Shrinkage	$J_{Nitrogen}$	Θ	F_B	σ_B
[°C]	[mm]	[%]	[$L \cdot m^{-2} \cdot h^{-1} \cdot bar^{-1}$]	[µm]	[N]	[MPa]
1100	1.13 ± 0.03	38.0	$508{,}800 \pm 59{,}900$	1.23	1.0 ± 0.1	44.4 ± 2.0
1120	1.12 ± 0.03	38.6	$388{,}200 \pm 52{,}700$	1.15	1.7 ± 0.3	72.3 ± 6.4
1170	1.13 ± 0.01	38.0	$119{,}300 \pm 25{,}100$	0.92	2.7 ± 0.1	111.9 ± 0.1

3.2. **Morphology and microstructure of the LCCF hollow fiber**

3.2.1. **Porous hollow fiber with a dense layer on top**

The green p-LCCF hollow fiber were cut in 60 cm lengths, dip coated for the deposition of the dense layer on top with different velocities, and then sintered at 1170 °C. After sintering, the c-LCCF fibers have an outer diameter of 1.13 mm, an inner diameter of 0.72 mm and a thickness of the porous wall of 185 µm. The thickness of the dense layer was varied by using different dip coating velocities. Table 5 summarizes the used coating velocities and the resulting layer thicknesses. Furthermore, the gas-tightness of the hollow fibers is added. Not all coating velocities lead to a dense layer. The best results with the highest yield of gas-tight membranes (> 90 %) could be achieved for coating velocities between 1.75 and 2.00 cm s^{-1}. With lower coating velocities, it was not possible to form a stable dense layer on the p-LCCF hollow fiber. With higher coating velocities, the surface tension was too high and cracks appeared at the surface after sintering with the result that the coating was not gas-tight.

Table 5: Summary of the different coating velocities of the p-LCCF, the resulting layer thicknesses of the dense layer and gas-tightness after sintering of the c-LCCF.

Coating velocity [cm s^{-1}]	Layer thickness [µm]	Gas tightness
0.50	11.9	< 1 bar
0.75	13.3	< 1 bar
1.00	15.6	< 1 bar
1.25	17.9	≤ 2 bar
1.50	20.6	≤ 2 bar
1.75	21.2	> 4 bar
2.00	21.8	> 4 bar
2.50	22.6	< 2 bar
3.00	25.3	< 1 bar
4.00	25.1	< 0.5 bar
5.00	27.5	< 0.5 bar

Fig. 2 shows SEM images of a c-LCCF membrane prepared by coating a porous LCCF hollow fiber with an outside dense layer and sintered at 1170 °C. The support structure (Fig. 2 b) shows finger-like pores along the whole cross-section, which explains the good nitrogen permeance. The difference between the dense layer and the porous support can be seen clearly in Fig. 2 c. In the dense layer only small closed pores are present. Furthermore, neck growth between the support structure and the dense layer can be spotted. In Fig. 2 d, the surface of the dense layer of c-LCCF is shown to be without any porosity.
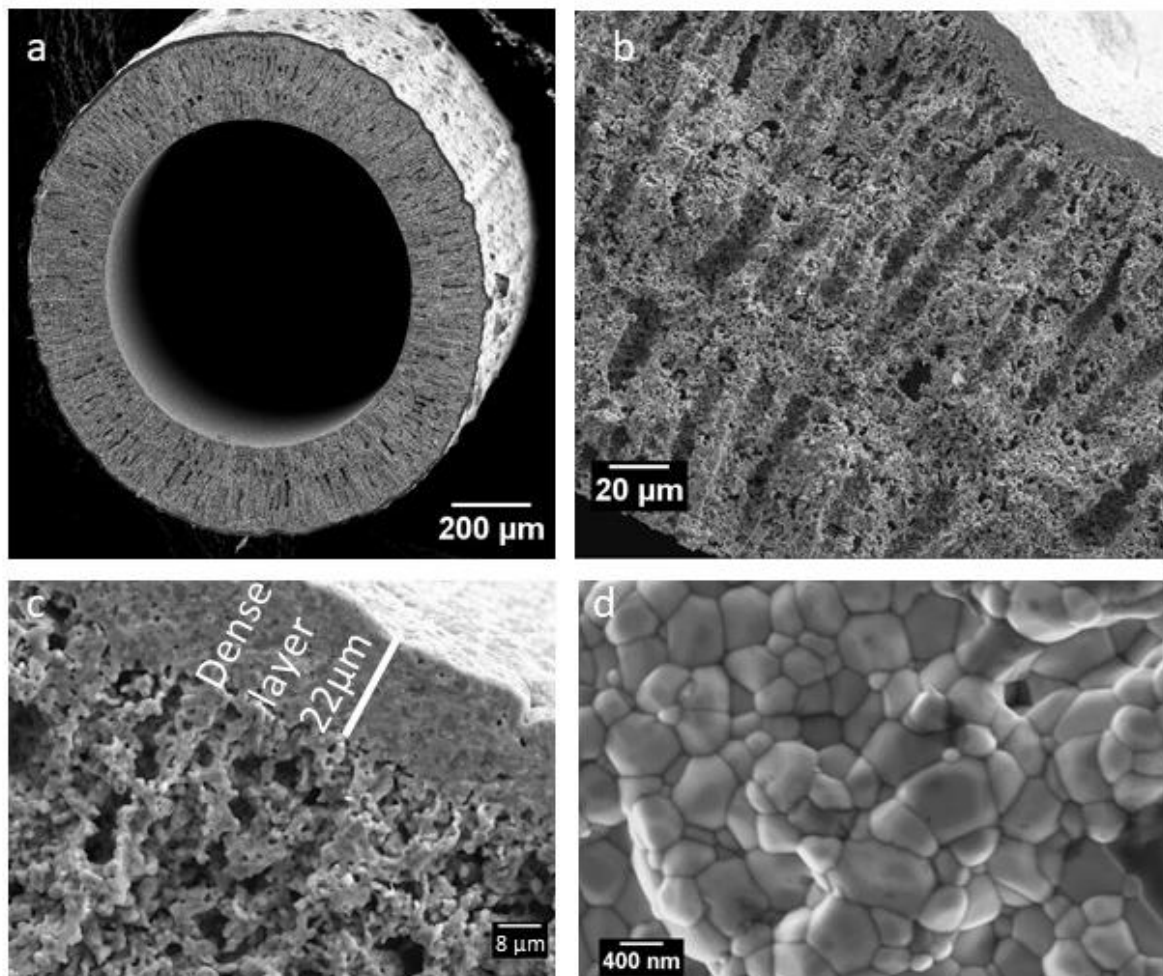
Fig. 2: SEM image of an asymmetric c-LCCF hollow fiber spun with the D_o = 2 mm spinneret, coated with a velocity of 2 cm s^{-1} and sintered at 1170 °C. (a) Support structure with dense layer; (b-c) cross-section and (d) dense surface of the fiber. Permeation study of this membrane see Fig. 7.

In our previous publication [41] it was found, that in LCCF the grain boundaries are barriers for oxygen permeation. Therefore, the average grain area of the dense layers of c-LCCF was derived from SEM images (Fig. 3) by particle analysis. For the dense layers of c-LCCF sintered at 1170 °C different grain areas between 0.07 µm^2 and 0.36 µm^2 were found. An average grain area of 0.16 µm^2 was calculated. For the d-LCCF, also sintered at 1170 °C an average grain area of 1.18 µm^2 was calculated. This can be explained by a particle size reduction due to the ball milling. As described in section 2.1, before the coating the LCCF powder was ball milled for 5 h at 300 U min^{-1}, which leads to a decrease of the particle size. The milled powder showed a 53 % decrease of the grain size compared to the untreated powder. The spinning solution of the d-LCCF fiber is also ball milled but at lower velocity and only to homogenise with the polymer and the solvent.
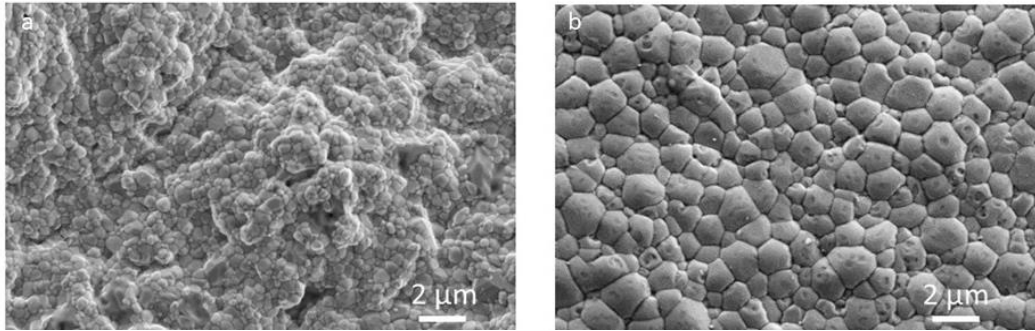
Fig. 3: SEM micrographs of LCCF hollow fiber outer surface sintered at 1170 °C to compare the particle areas of the different manufacturing methods. (a) c-LCCF and (b) d-LCCF. Permeation study of these membranes see Fig. 7.

3.2.2. **Surface etched e-LCCF hollow fibers**

The d-LCCF hollow fibers manufactured for the surface etching were spun without rice starch, sintered at 1220 °C having an outer diameter of 1.13 mm, an inner diameter of 0.79 mm and a wall thickness of 0.17 mm. The SEM micrographs of the non-etched membrane is shown in Fig. 4 a-c. The inner and outer surfaces (Fig. 4 b, c) show a dense surface. The cross section (Fig. 4 a) has some elongated non-interconnected pores, what is typical for hollow fibers manufactured via wet spinning. The d-LCCF hollow fibers were etched for 3 h at the outer surface (Fig. 4 e) and show a higher surface roughness compared to the untreated fiber. In the image of the cross section (Fig. 4 d), it can be seen that the acid did not soak into the fiber. The modification of the inner surface is shown in Fig. 4 g-i. The inner surface (Fig. 4 i) contains some radial aggregates (marked by arrow). The composition of the radial aggregates were analysed with EDX measurements in Fig. 6. The etching of both surfaces is shown in Fig. 4 j-l. Interestingly, the inner surface (Fig. 4 l) has some lengthwise cracks and no radial aggregates. The outer surface is quite similar to Fig. 4 e. Furthermore, no significant decrease of the wall thickness can be seen and the lengthwise cracks do not reach through the cross-section. Therefore, the etching of the surfaces results only in a higher surface roughness and not in a decrease of the wall thickness.
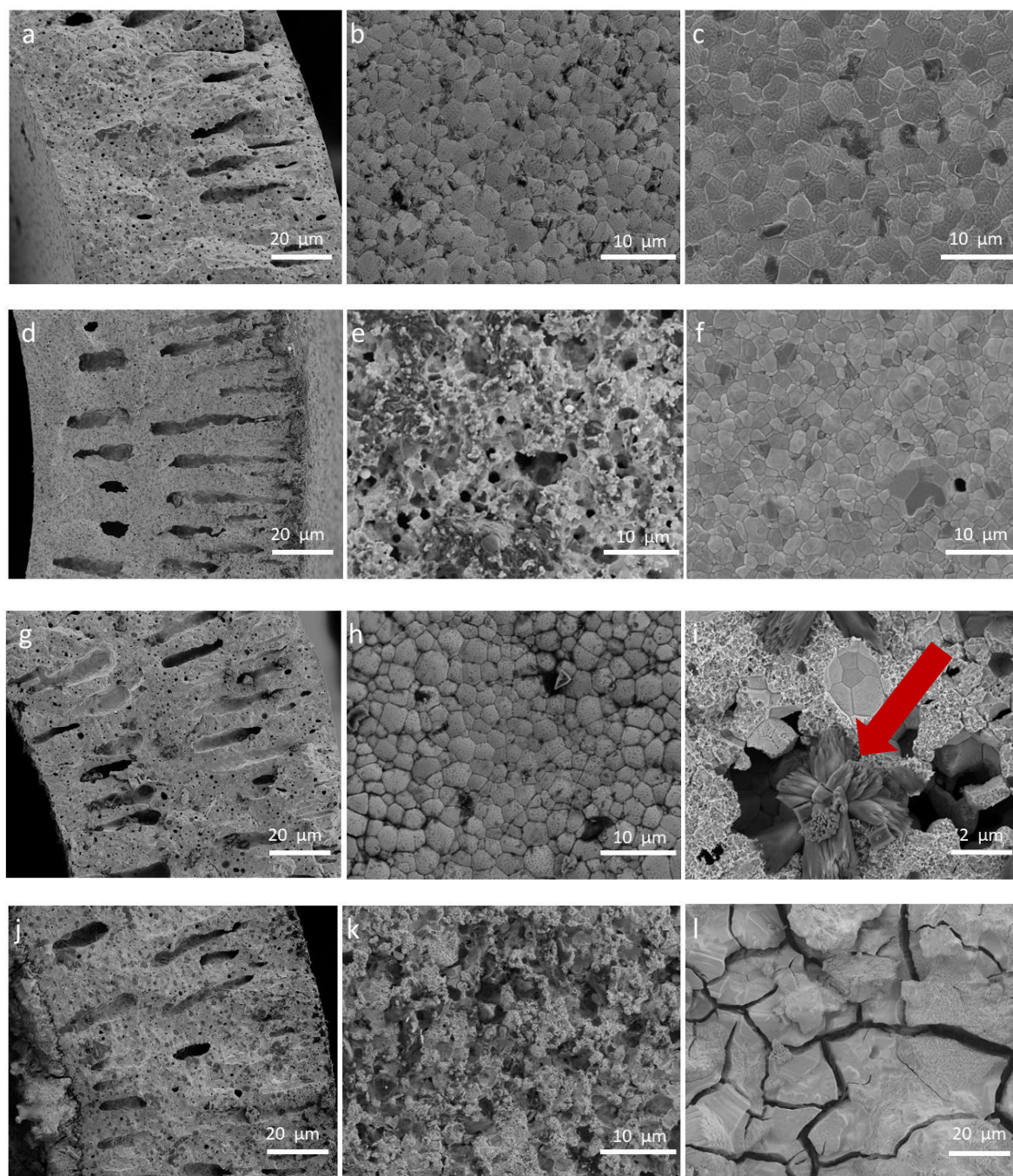
Fig. 4: SEM images of a LCCF hollow fiber before and after etching. a-c Untreated d-LCCF; d-f e-LCCF etched for 3 h with H_2SO_4 at outer surface; g-i etched for 3 h with H_2SO_4 at inner surface; j-l etched for 3 h with H_2SO_4 at inner and outer surfaces. a, d, g and j, cross section; b, e, h, and k outer surface and c, f, i and l inner surface. Permeation study of these membranes see Fig. 11, Fig. 12 and Fig. 13.

The mechanical strength of the d- and e-LCCF hollow fibers sintered at 1220 °C and etched inside and/or outside for different times is shown in Fig. 5. Here, the maximum bending force and the bending strength are shown for the different hollow fibers. As expected, the etching of the hollow fiber leads to a decrease of the max. bending force as well as the bending strength. The etching of the outer surface of the hollow fiber has a stronger impact compared to the etching of the inner surface. The highest decrease in the mechanical properties was found after etching the inner and the outer surface for 180 min. The max. bending force decreased by 30.5 % and the bending strength by 31.0 %.
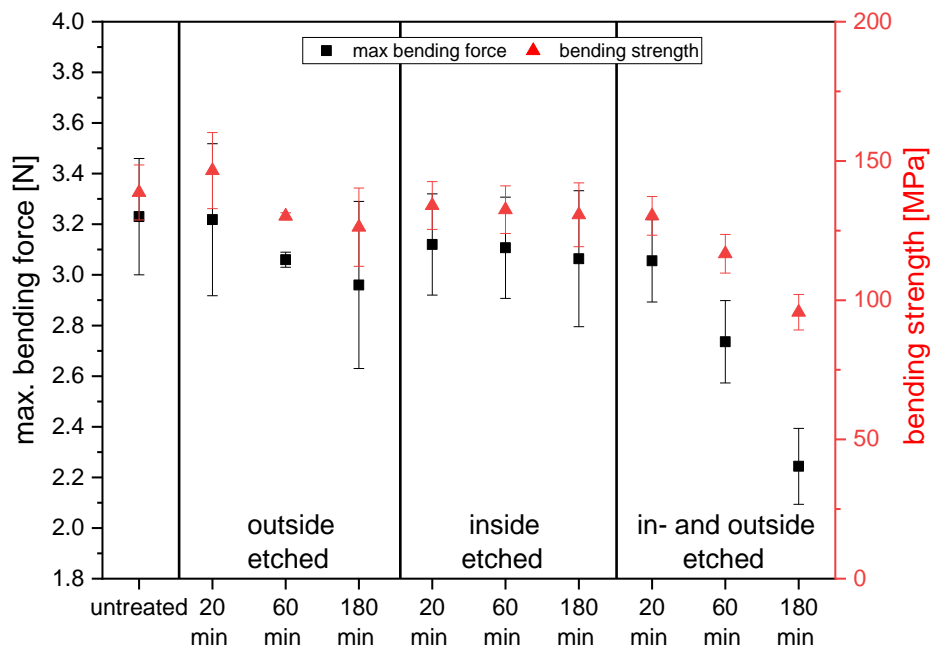
Fig. 5: Bending force and bending strength for e-LCCF fibers with different etching times and etching sites. All the starting d-LCCF fibers were spun with the spinneret D_o= 2mm and sintered at 1220 °C.

In Table 6, the composition of the cations found in the etching solution after the treatment of the outer surface of d-LCCF are shown. Compared to the bulk powder composition, the content of lanthanum is much higher. This indicates that dissolution of lanthanum from LCCF by H_2SO_4 is favoured. Cobalt, on the other hand, is less favoured. This means that after etching a higher amount of cobalt and a smaller amount of lanthanum is present in the surface of the e-LCCF hollow fiber. The etching duration plays a secondary role since the percentage ratio of the components are nearly the same after 20, 60 and 180 min. On the other hand, the total dissolved amount increases with increasing time. However, this increase is not linear with increasing etching time.

Table 6: Percentage ratio of the individual elements from the acidic etching solution analysed with ICP-MS and ICP-OES.

Sample	La [%]	Ca [%]	Co [%]	Fe [%]	Total dissolved amount [mg l^{-1}]
LCCF powder	0.3	0.2	0.4	0.1	-
20 min	0.60	0.13	0.20	0.07	407
60 min	0.61	0.13	0.19	0.07	472
180 min	0.59	0.13	0.22	0.07	503

From the SEM image of the e-LCCF fibers etched at the inner surface (see Fig. 4 i), EDX measurement were made to figure out the composition of the darker spots (Fig. 6). The images show an enrichment of cobalt in the center of the darker spots, and around them an enrichment of calcium. This means lanthanum is etched out of the fiber and cobalt is enriched in some areas. These results are in good agreement with the ICP measurements (Table 6).
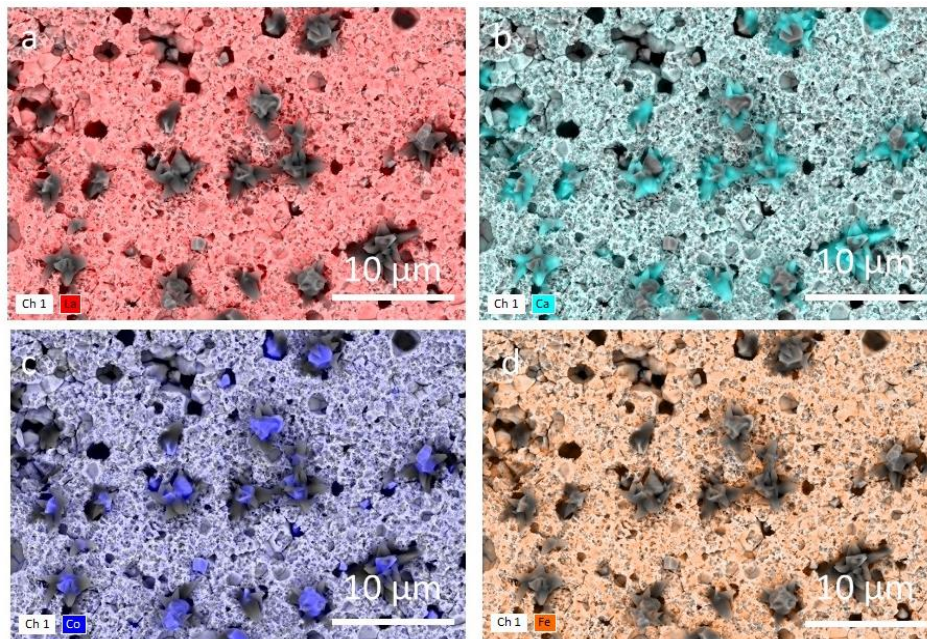
Fig. 6: EDX images of the inner surface of the e-LCCF hollow fiber etched for 3 h at the inner surface (see Fig. 4 i). a) lanthanum, b) calcium, c) cobalt, d) iron. Permeation study of these membranes see Fig. 12

3.3. **Permeation results**

3.3.1. **Porous hollow fiber with dense layer**

As mentioned above, the oxygen permeation through MIEC membranes can be limited by two mechanisms: Bulk diffusion and surface exchange reaction. To investigate the dominating step, c-LCCF and d-LCCF were manufactured and compared. Fig. 7 shows the permeation in dependence of the temperature for different dense layer thicknesses. The d-LCCF fibers have dense layers of 179 µm, 73 µm, and the c-LCCF fiber has a dense coating of 22 µm. As expected, the oxygen permeation increases by 63.9 % with a decrease of the wall thickness from 179 µm to 73 µm at 1000 °C. Surprisingly, no significant increase between the d-LCCF fiber with a dense layer thickness of 73 µm (4.87 ml min^{-1} cm^{-2} at 1000 °C) and the c-LCCF fiber (5.10 ml min^{-1} cm^{-2} at 1000 °C) can be seen. We expected a higher increase of the oxygen permeation due to the reduced dense layer thickness. Furthermore, we suggest a higher permeation due to the porous support structure. The porous structure should increase the surface area, which leads to a better oxygen exchange. The only small difference can be explained by the SEM images in Fig. 3. As already mentioned, the grain size has a big influence on the oxygen permeation. In our previous publication [41], a rise of the oxygen permeation with increasing average grain size was measured. In our case, the average grain size of the c-LCCF is 86.4 % smaller than the grain size in the d-LCCF fiber. Furthermore, concentration polarization in the porous layer could also lead to a decrease of the driving force for permeation. Values of the activation energy of oxygen permeation through the d-LCCF and c-LCCF hollow fibers with different thickness of the dense layers were determined from an Arrhenius plot, as given in Fig. 8. The activation energy decreases with decreasing thickness of the dense layer from 182.5 kJ mol^{-1} (179 µm) to 148.4 kJ mol^{-1} (22 µm).
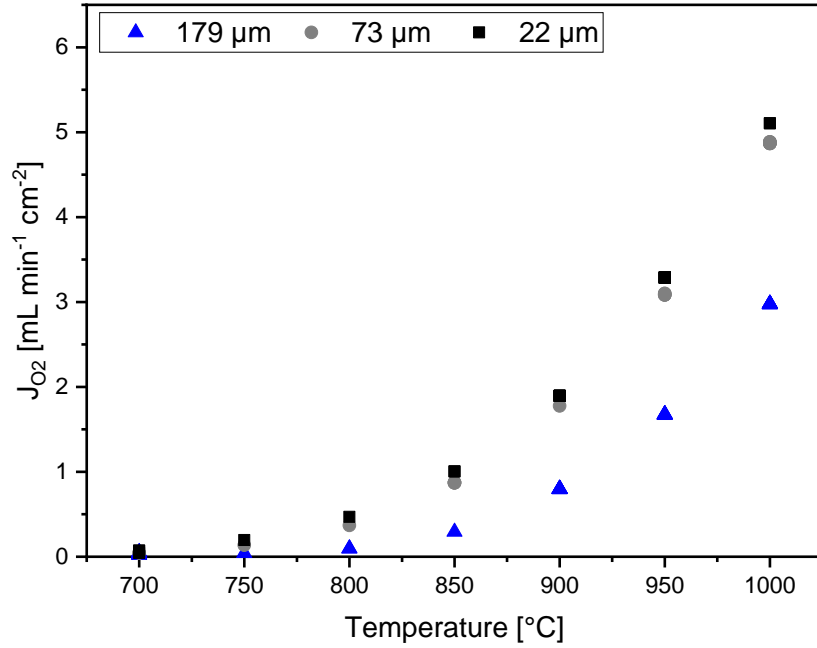
Fig. 7: Oxygen permeation through d-LCCF and c-LCCF hollow fibers sintered at 1170 °C with different dense layer thicknesses (d-LCCF: 179 µm, 73 µm; c-LCCF: 22 µm) in dependence of the temperature. Test conditions: Sweep flow: 100 Nml min^{-1} N$_2$; Feed flow: 35 Nml min^{-1} N$_2$, 65 Nml min^{-1} CO$_2$, 30 Nml min^{-1} O$_2$; Pressure feed side: 2 bar, pressure sweep side: 1 bar.
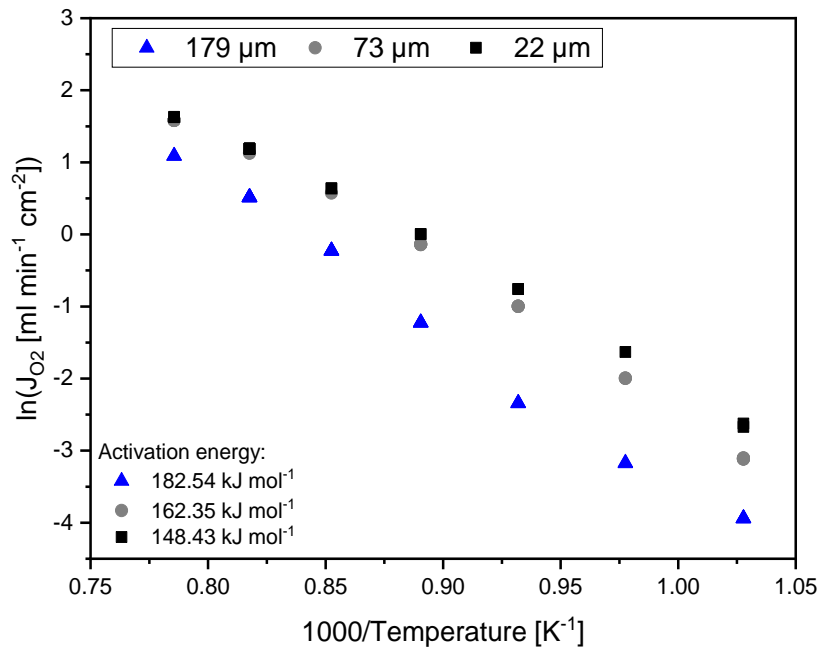
Fig. 8: Arrhenius plot of the oxygen flux through d-LCCF and c-LCCF fibers sintered at 1170 °C with different dense layer thicknesses. The various symbols show the different dense layer thicknesses. Test conditions see Fig. 7.

In Fig. 9, the Wagner plot for hollow fibers with different dense layer thicknesses is presented at 900 °C. The n-value according to Eq. 1 increases with decreasing thickness of the dense layer. The n-values reach from n = 0.11 for 179 µm to n = 0.39 for 22 µm. However, the n-values are still between 0 and 0.5, which means that both bulk diffusion and surface reaction are rate limiting steps controlling the oxygen transport. However, for the asymmetric c-LCCF hollow fiber with the dense layer of 22 µm, a higher n-value was expected. This mismatch can be explained by the small average grain size. A further reason might be the porous support structure, which offers more surface for oxygen exchange reaction and therefore reduces the n value.
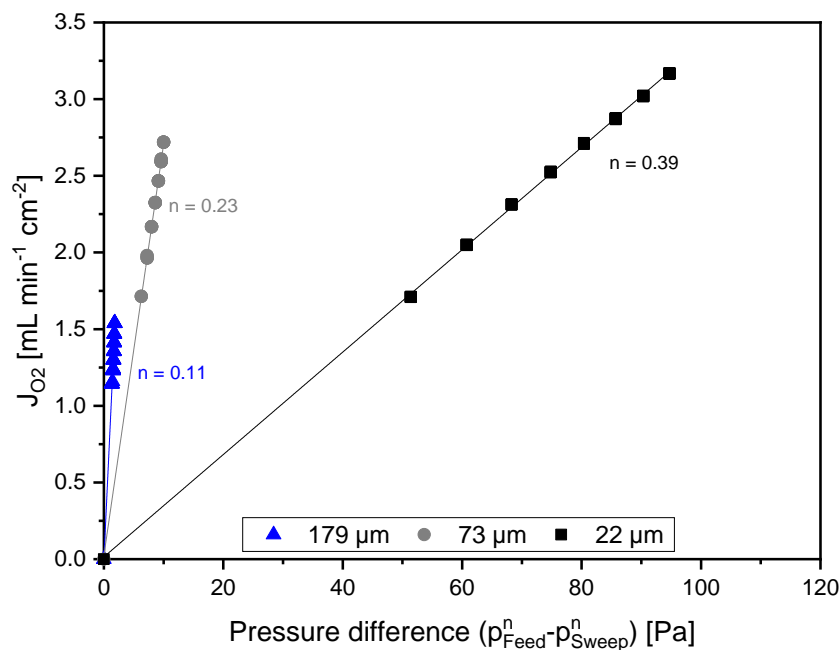
Fig. 9: Wagner plot for d-LCCF and c-LCCF hollow fibers with different dense layer thicknesses. The n-values are calculated for each measurement. Test conditions: Sweep flow 100 Nml min^{-1} N_2; Temperature: 900 °C; Total feed flow: 100 Nml min^{-1}. Pressure feed side: 2 bar; pressure sweep side: 1 bar.

For the coated hollow fibers with a dense layer thickness of 22 µm, a long-term stability test in 50 % CO_2 was made (Fig. 10). The fiber was tested for more than 250 h at 900 °C. At the beginning, a decrease of the permeation flux can be seen, but the curve approximates to the value of 1.66 ml min^{-1} cm^{-2}. Compared to the literature [11], it is an increase of 61 % for a long-term test in a CO_2 atmosphere at 900 °C.
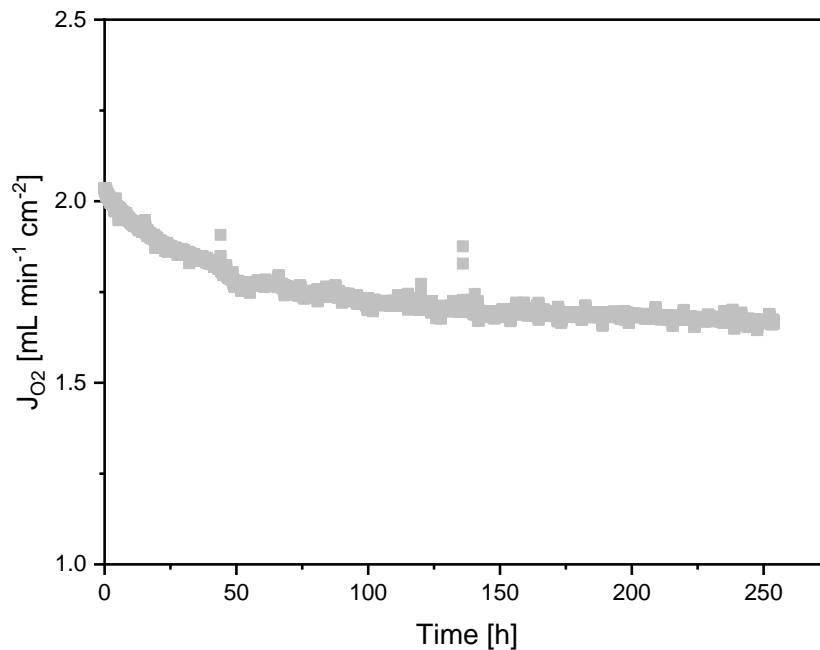
Fig. 10: Long-term test of the asymmetric c-LCCF hollow fiber with 22 µm dense layer sintered at 1170 °C. Test conditions see Fig. 7. The temperature was constant at 900 °C.

3.3.2. **Surface etched LCCF hollow fibers**

Another possibility to increase the transport through a MIEC membrane is to optimize the surface exchange reactions. Therefore, dense d-LCCF hollow fiber membranes were etched with H_2SO_4 on the outer, inner and both surfaces. In Fig. 11, the influence of the etching time on the oxygen permeation is shown when only the outer LCCF hollow fiber surface is etched. At 1000 °C the oxygen permeation increases from 3.21 ml min^{-1} cm^{-2} for the untreated fiber to 5.23 ml min^{-1} cm^{-2} for 180 min surface etching. This is an increase of 62.9 %. It can be seen from the curves that an etching time over 60 min does not lead to a further increase of oxygen permeation. The results of the etching of the inner surface (Fig. 12) and of both surfaces (Fig. 13) show the same tendency. However, the increase of the oxygen permeation for etching of the inner surface (4.18 ml min^{-1} cm^{-2} at 1000 °C by an etching time of 180 min) is in general smaller (30.2 %) compared to the etching of the outer surface. This result is in complete accordance with the SEM images in Fig. 4. The etching of the outer surface leads to a higher roughness, what means a larger surface for desorption of oxygen from the surface. It should be noted that etching does not reduce the layer thickness but only increases surface roughness. The largest increase of oxygen transport (86.0 % at 1000 °C for an etching time of 180 min) can be seen for the hollow fiber etched at both surfaces (Fig. 13). This experimental finding indicates that desorption on the oxygen lean side is controlling the overall oxygen permeation rather than

the adsorption on the oxygen rich side. This finding is in good agreement with literature [43] suggesting that the surface microstructure of the hollow fiber membrane plays an important role in the oxygen permeation behaviour.
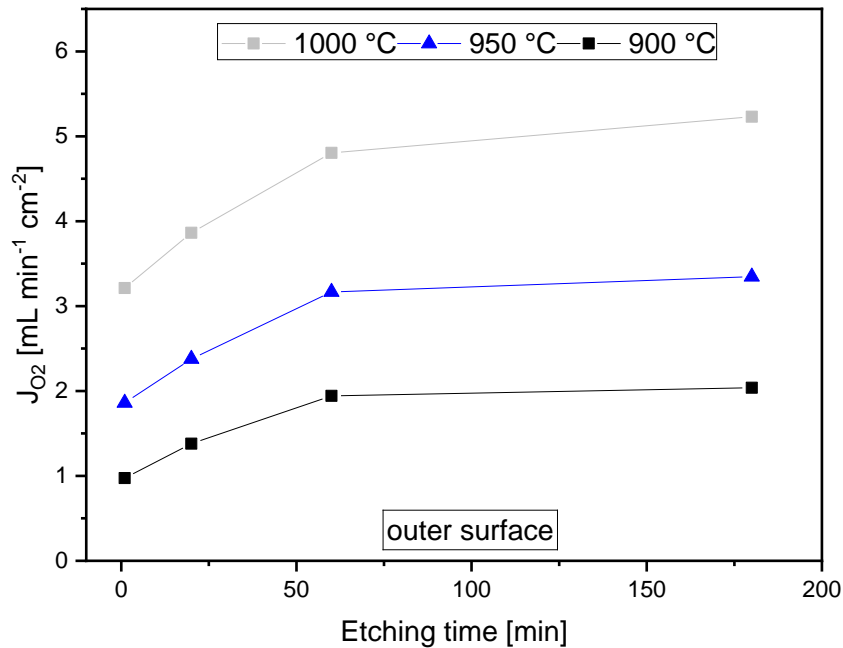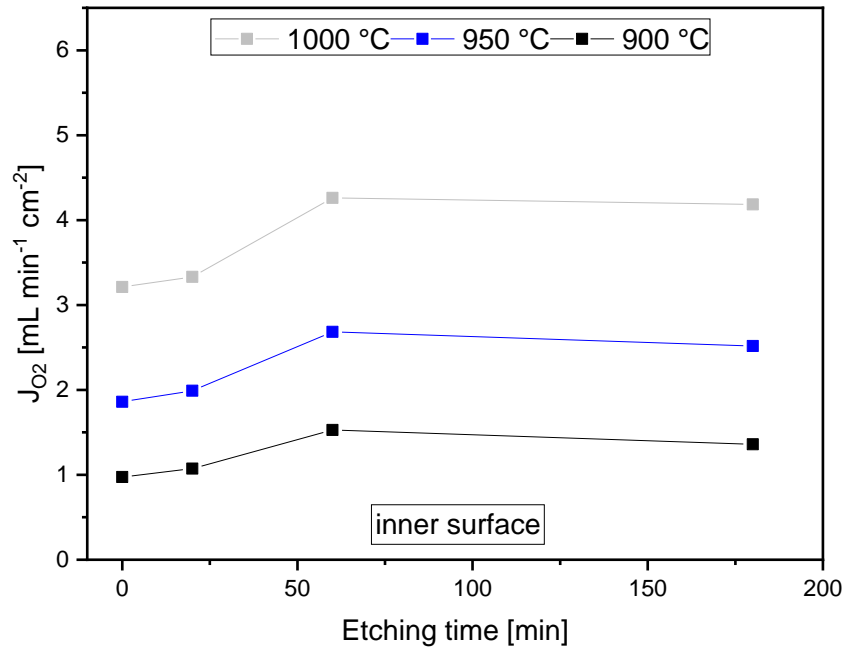

Fig. 11: Oxygen permeation of e-LCCF hollow fibers sintered at 1220 °C as a function of the etching duration at different temperatures (900 °C, 950 °C and 1000 °C) in a 50 % CO_2 atmosphere. The hollow fiber were etched at the outer surface. Test conditions: Feed flow: 65 Nml $min^{-1}cm^{-2}$ CO_2, 35 Nml min^{-1} cm^{-2} N_2, 30 Nml min^{-1} cm^{-2} O_2; Sweep flow: 100 Nml min^{-1} cm^{-2} N_2. Pressure feed side: 2 bar; pressure sweep side: 1 bar.

Fig. 12: Oxygen permeation of e-LCCF hollow fibers sintered at 1220 °C as a function of the etching duration at different temperatures (900 °C, 950 °C and 1000 °C) in a 50 % CO_2 atmosphere. The hollow fiber were etched at the inner surface. Test conditions see Fig. 11.
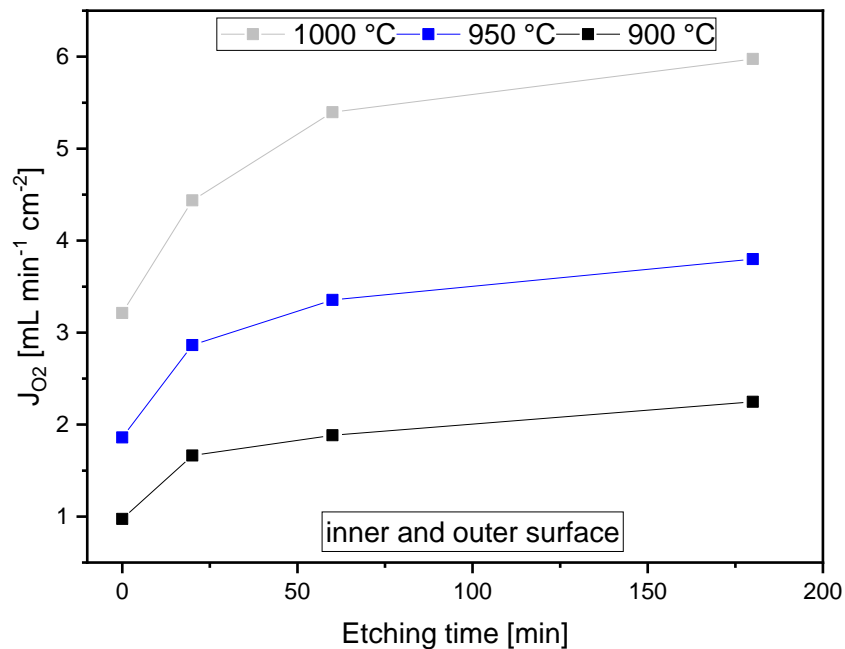
Fig. 13: Oxygen permeation at different temperatures (900 °C, 950 °C and 1000 °C) from a 50 % CO_2 atmosphere through e-LCCF hollow fibers as a function of the etching duration. The LCCF hollow fibers were sintered at 1220 °C and etched at the inner and the outer surface. Each surface was etched for the corresponding time. Test conditions see Fig. 11.

Fig. 14 shows the oxygen permeation improvement factor of the hollow fibers etched on both surfaces with different etching times as a function of the permeation temperature. For all three etching times (20 min, 60 min and 180 min) the improvement factor decrease with increasing temperature. For the fiber etched over 180 min, the improvement factor decreases from 3.2 (at 750 °C) to 1.9 (at 1000 °C). This phenomenon can be explained by the dependency of the oxygen vacancies on the temperature, which is in good agreement with previous findings [34]. At relative low temperatures, only a small amount of oxygen vacancies for bulk transport is present; therefore, the influence of the surface exchange reaction has a bigger influence on the overall oxygen transport. At higher temperatures, however, more oxygen vacancies are present, which leads to a smaller influence of the surface exchange reaction and a bigger influence of the bulk diffusion.
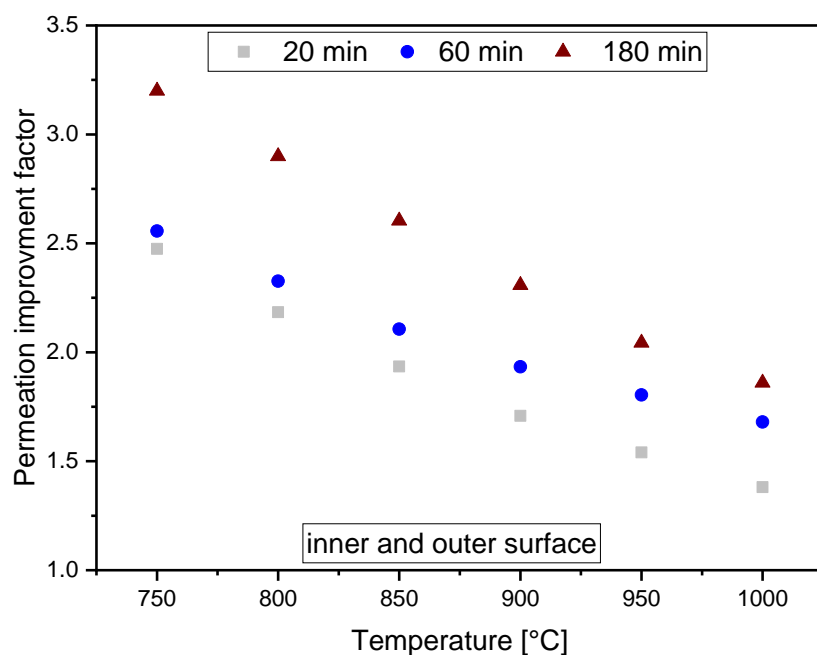
Fig. 14: Oxygen permeation improvement factors of e-LCCF hollow fibers sintered at 1220 °C and etched on their inner and outer surfaces for different times as function of temperature. Test conditions see Fig. 11.

The activation energies of oxygen permeation through the e-LCCF hollow fiber membranes were determined from an Arrhenius plot similar to Fig. 8. All the fibers etched with sulphuric acid have a lower activation energy than the untreated hollow fibers. Surprisingly, the activation energies of the outer surface etched fibers (60 min and 180 min) are the lowest (145.7 kJ mol^{-1} and 128.8 kJ mol^{-1}). The surface etching of the outer surface has a strong influence on oxygen

permeation at lower temperatures (< 800 °C), while at higher temperatures the influence strongly decreases because of the increase of the oxygen vacancy concentration, which pushes bulk transport. For fibers etched at both surfaces, this influence is less strongly pronounced. Therefore, the increase of oxygen permeation with rising temperature is lower for fibers etched on only one side. This finding results in a lower slope in the Arrhenius plot and, consequently, in a lower activation energy.
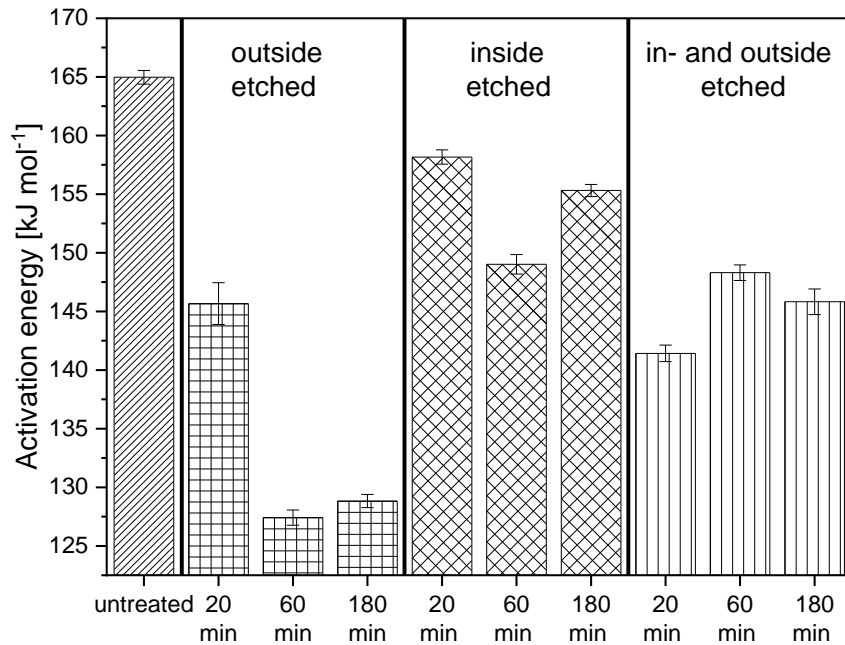

Fig. 15: Activation energy of oxygen permeation through e-LCCF hollow fibers sintered at 1220 °C with different surface etching sites (inner, outer and both surfaces) and different surface etching times (0 min, 20 min, 60 min, 180 min). Test conditions see Fig. 11.

4. Conclusions

In this work, the oxygen permeation flux of CO_2-stable LCCF hollow fibers was improved via two strategies. (i) Asymmetric hollow fiber membrane with a 22 µm thin dense LCCF layer on a macroporous LCCF support were successfully prepared by wet spinning, dip coating and co-sintering. (ii) The surface reaction of dense LCCF hollow fiber membranes was improved by etching with H_2SO_4.

To manufacture porous hollow fibers as support, rice starch as pore former was added to the LCCF spinning solution. This leads to finger-like pores perpendicular to the surface of the macroporous hollow fiber resulting in a high nitrogen permeance ($119.3 \cdot 10^3$ L m^{-1} h^{-1} bar^{-1} at 1170 °C) and a good mechanical stability (111.9 MPa bending strength). However, the oxygen permeation improvement of the asymmetric LCCF hollow fiber with a 22 µm dense layer

compared to the completely dense hollow fiber with a wall thickness of 73 μm was only 5 % higher. This unexpected small increase of oxygen permeation can be explained by the 86.4 % smaller average grain size of the dense LCCF layer of the asymmetric hollow fiber compared to the completely dense LCCF hollow fiber. The n-value of the Wagner plot showed an increase with decreasing wall thickness but the oxygen transport is still affected by both bulk diffusion and surface exchange. The long-term (>250 h) stability in a 50 % CO_2 atmosphere was successfully tested with a permeation flux of 1.7 ml min^{-1} cm^{-2} at 900 °C.

Dense LCCF hollow fibers sintered at 1220 °C were successfully etched with sulphuric acid at the inner and/or outer surfaces. By increasing the etching time, the permeation increases towards a limit. The highest oxygen permeation flux (5.9 ml min^{-1} cm^{-2} at 1000 °C) could be achieved by etching both surfaces for 180 min. In contrast, the permeation improvement factor decreases with increasing temperature because of the dependency of the oxygen vacancy concentration on the temperature.

With this study, applying the co-sintering technology, asymmetric hollow fibers at lower cost can be produced. Further, dense hollow fibers with optimized surface reaction can be prepared by etching. Both methods combine high oxygen permeation with high CO_2-tolerance.

References

[1] S. Dyatlov, N. Didenko, E. Ivanova, E. Soshneva, S. Kulik, Prospects for alternative energy sources in global energy sector, IOP Conference Series: Earth and Environmental Science, IOP Publishing (2020) 012014. https://doi.org/10.1088/1755-1315/434/1/012014

[2] IEA, Key Wolrd Energy Statistics 2020, (2020).

[3] G. Chen, F. Buck, I. Kistner, M. Widenmeyer, T. Schiestel, A. Schulz, M. Walker, A. Weidenkaff, A novel plasma-assisted hollow fiber membrane concept for efficiently separating oxygen from CO in a CO_2 plasma, Chemical Engineering Journal (2019) 123699. https://doi.org/10.1016/j.cej.2019.123699

[4] W. Fang, F. Steinbach, C. Chen, A. Feldhoff, An approach to enhance the CO_2 tolerance of fluorite–perovskite dual-phase oxygen-transporting membrane, Chemistry of Materials 27 (2015) 7820-7826. https://doi.org/10.1021/acs.chemmater.5b03823

[5] F. Schulze-Küppers, U. Unije, H. Blank, M. Balaguer, S. Baumann, R. Mücke, W. Meulenberg, Comparison of freeze-dried and tape-cast support microstructure on high-flux oxygen transport membrane performance, Journal of Membrane Science 564 (2018) 218-226. https://doi.org/10.1016/j.memsci.2018.07.028

[6] Y. Liu, V. Motalov, S. Baumann, D. Sergeev, M. Müller, Y.J. Sohn, O. Guillon, Thermochemical stability of Fe-and Co-functionalized perovskite-type $SrTiO_3$ oxygen transport membrane materials in syngas conditions, Journal of the European Ceramic Society 39 (2019) 4874-4881. https://doi.org/10.1016/j.jeurceramsoc.2019.06.045

[7] R. Ruhl, J. Song, V. Thoréton, S.P. Singh, K. Wiik, Y. Larring, H.J. Bouwmeester, Structure, electrical conductivity and oxygen transport properties of perovskite-type oxides $CaMn_{1-x-y}Ti_xFe_yO_{3-\delta}$, Physical Chemistry Chemical Physics 21 (2019) 21824-21835. https://doi.org/10.1039/C9CP04911H

[8] L. Wang, R. Dou, G. Wang, Y. Li, M. Bai, D. Hall, Y. Chen, A case study of mechanical properties of perovskite-structured $Ba_{0.5}Sr_{0.5}Co_{0.8}Fe_{0.2}O_{3-\delta}$ oxygen transport membrane, Journal of the European Ceramic Society 38 (2018) 647-653. https://doi.org/10.1016/j.jeurceramsoc.2017.09.002

[9] Y. Teraoka, H. Zhang, K. Okamoto, N. Yamazoe, Mixed ionic-electronic conductivity of $La_{1-x}Sr_xCo_{1-y}Fe_yO_{3-\delta}$ perovskite-type oxides, Materials Research Bulletin 23 (1988) 51-58. https://doi.org/10.1016/0025-5408(88)90224-3

[10] G. Chen, W. Liu, M. Widenmeyer, P. Ying, M. Dou, W. Xie, C. Bubeck, L. Wang, M. Fyta, A. Feldhoff, High flux and CO2-resistance of $La_{0.6}Ca_{0.4}Co_{1-x}Fe_xO_{3-\delta}$ oxygen-transporting membranes, Journal of Membrane Science 590 (2019) 117082. https://doi.org/10.1016/j.memsci.2019.05.007

[11] F. Buck, I. Kistner, C. Rosler, A. Schulz, M. Walker, G. Tovar, T. Schiestel, Use of Perovskite Hollow Fiber Membranes in a Microwave Plasma, Chemie Ingenieur Technik 91 (2019) 1117-1122. https://doi.org/10.1002/cite.201900048

[12] J. Stevenson, T. Armstrong, R. Carneim, L. Pederson, W. Weber, Electrochemical properties of mixed conducting perovskites $La_{1-x}M_xCo_{1-y}Fe_yO_{3-\delta}$ (M= Sr, Ba, Ca), Journal of the Electrochemical Society 143 (1996) 2722. https://doi.org/10.1149/1.1837098

[13] M. Salehi, M. Søgaard, V. Esposito, S.P.V. Foghmoes, E. Persoon, M. Schroeder, P.V. Hendriksen, Oxygen permeation and stability study of $(La_{0.6}Ca_{0.4})_{0.98}(Co_{0.8}Fe_{0.2})O_{3-\delta}$ membranes, Journal of Membrane Science 542 (2017) 245-253. https://doi.org/10.1016/j.memsci.2017.07.050

[14] K. Efimov, T. Klande, N. Juditzki, A. Feldhoff, Ca-containing CO_2-tolerant perovskite materials for oxygen separation, Journal of Membrane Science 389 (2012) 205-215. https://doi.org/10.1016/j.memsci.2011.10.030

[15] S. Baumann, F. Schulze-Küppers, S. Roitsch, M. Betz, M. Zwick, E. Pfaff, W. Meulenberg, J. Mayer, D. Stöver, Influence of sintering conditions on microstructure and oxygen permeation of $Ba_{0.5}Sr_{0.5}Co_{0.8}Fe_{0.2}O_{3-\delta}$ (BSCF) oxygen transport membranes, Journal of Membrane Science 359 (2010) 102-109. https://doi.org/10.1016/j.memsci.2010.02.002

[16] O. Czuprat, M. Arnold, S. Schirrmeister, T. Schiestel, J. Caro, Influence of CO_2 on the oxygen permeation performance of perovskite-type $BaCo_xFe_yZr_zO_{3-\delta}$ hollow fiber membranes, Journal of Membrane Science 364 (2010) 132-137. https://doi.org/10.1016/j.memsci.2010.08.019

[17] A.S. Sihar, N.H. Othman, N.H. Alias, M.Z. Shahruddin, S.S.A. Syed-Hassan, M.A. Rahman, A.F. Ismail, Z. Wu, Fabrication of lanthanum-based perovskites membranes on porous alumina hollow fibre (AHF) substrates for oxygen enrichment, Ceramics International 45 (2019) 13086-13093. https://doi.org/10.1016/j.ceramint.2019.03.242

[18] X. Yin, C. Choong, L. Hong, Z. Liu, Crafting $La_{0.2}Sr_{0.8}MnO_{3-\delta}$ membrane with dense surface from porous YSZ tube, Journal of Solid State Electrochemistry 10 (2006) 643-650. https://doi.org/10.1007/s10008-006-0131-1

[19] H.J. Bouwmeester, A.J. Burggraaf, Dense ceramic membranes for oxygen separation, in Membrane Science and Technology, Elsevier (1996) pp. 435-528.

[20] P. Zeng, R. Ran, Z. Chen, H. Gu, Z. Shao, J.D. da Costa, S. Liu, Significant effects of sintering temperature on the performance of $La_{0.6}Sr_{0.4}Co_{0.2}Fe_{0.8}O_{3-\delta}$ oxygen selective membranes, Journal of Membrane Science 302 (2007) 171-179. https://doi.org/10.1016/j.memsci.2007.06.047

[21] V. Middelkoop, H. Chen, B. Michielsen, M. Jacobs, G. Syvertsen-Wiig, M. Mertens, A. Buekenhoudt, F. Snijkers, Development and characterisation of dense lanthanum-based perovskite oxygen-separation capillary membranes for high-temperature applications, Journal of Membrane Science 468 (2014) 250-258. https://doi.org/10.1016/j.memsci.2014.05.032

[22] B. Zydorczak, Z. Wu, K. Li, Fabrication of ultrathin $La_{0.6}Sr_{0.4}Co_{0.2}Fe_{0.8}O_{3-\delta}$ hollow fibre membranes for oxygen permeation, Chemical Engineering Science 64 (2009) 4383-4388. https://doi.org/10.1016/j.ces.2009.07.007

[23] Z. Wang, N. Yang, B. Meng, X. Tan, K. Li, Preparation and oxygen permeation properties of highly asymmetric $La_{0.6}Sr_{0.4}Co_{0.2}Fe_{0.8}O_{3-\alpha}$ perovskite hollow-fiber membranes, Industrial & Engineering Chemistry Research, 48 (2009) 510-516. https://doi.org/10.1021/ie8010462

[24] H. Pan, L. Li, X. Deng, B. Meng, X. Tan, K. Li, Improvement of oxygen permeation in perovskite hollow fibre membranes by the enhanced surface exchange kinetics, Journal of Membrane Science 428 (2013) 198-204. https://doi.org/10.1016/j.memsci.2012.10.020

[25] N. Han, S. Zhang, X. Meng, N. Yang, B. Meng, X. Tan, S. Liu, Effect of enhanced oxygen reduction activity on oxygen permeation of $La_{0.6}Sr_{0.4}Co_{0.2}Fe_{0.8}O_{3-\delta}$ membrane decorated by K_2NiF_4-type oxide, Journal of Alloys and Compounds 654 (2016) 280-289. https://doi.org/10.1016/j.jallcom.2015.09.086

[26] D. Han, J. Sunarso, X. Tan, Z. Yan, L. Liu, S. Liu, Optimizing oxygen transport through $La_{0.6}Sr_{0.4}Co_{0.2}Fe_{0.8}O_{3-\delta}$ hollow fiber by microstructure modification and Ag/Pt catalyst deposition, Energy & Fuels 26 (2012) 4728-4734. https://doi.org/10.1021/ef300542e

[27] L. Wei, M. Ma, Y. Lu, D. Wang, S. Zhang, Q. Wang, Surface modification of macroporous Al_2O_3 tubes with carbon-doped TiO_2 intermediate layer and preparation of highly permeable palladium composite membranes for hydrogen separation, Separation Science and Technology 55 (2020) 980-987. https://doi.org/10.1080/01496395.2018.1481431

[28] Y. Liu, L. Hong, Fabrication and characterization of (Pd/Ag)–$La_{0.2}Sr_{0.8}CoO_{3-\delta}$ composite membrane on porous asymmetric substrates, Journal of Membrane Science 224 (2003) 137-150. https://doi.org/10.1016/j.memsci.2003.08.002

[29] S. Liu, K. Li, Preparation TiO_2/Al_2O_3 composite hollow fibre membranes, Journal of Membrane Science 218 (2003) 269-277. https://doi.org/10.1016/S0376-7388(03)00184-4

[30] T. He, M. Mulder, H. Strathmann, M. Wessling, Preparation of composite hollow fiber membranes: co-extrusion of hydrophilic coatings onto porous hydrophobic support structures, Journal of Membrane Science 207 (2002) 143-156. https://doi.org/10.1016/S0376-7388(02)00118-7

[31] J. García-Fayos, R. Ruhl, L. Navarrete, H.J. Bouwmeester, J.M. Serra, Enhancing oxygen permeation through $Fe_2NiO_4–Ce_{0.8}Tb_{0.2}O_{2-\delta}$ composite membranes using porous layers activated with Pr_6O_{11} nanoparticles, Journal of Materials Chemistry A 6 (2018) 1201-1209. https://doi.org/10.1039/C7TA06485C

[32] Y.-I. Kwon, B.T. Na, J.H. Park, K.S. Yun, S.K. Hong, J.H. Yu, J.H. Joo, Guidelines for selecting coating materials for a high oxygen permeation flux in a fluorite-rich dual-phase membrane, Journal of Membrane Science 535 (2017) 200-207. https://doi.org/10.1016/j.memsci.2017.04.036

[33] H. Liu, X. Tan, Z. Pang, J.D. Da Costa, G.Q. Lu, S. Liu, Novel dual structured mixed conducting ceramic hollow fibre membranes, Separation and Purification Technology 63 (2008) 243-247. https://doi.org/10.1016/j.seppur.2008.04.017

[34] Z. Wang, H. Liu, X. Tan, Y. Jin, S. Liu, Improvement of the oxygen permeation through perovskite hollow fibre membranes by surface acid-modification, Journal of Membrane Science 345 (2009) 65-73. https://doi.org/10.1016/j.memsci.2009.08.024

[35] T. Armstrong, F. Prado, A. Manthiram, Synthesis, crystal chemistry, and oxygen permeation properties of $LaSr_3Fe_{3-x}Co_xO_{10}$ ($0\leq x\leq 1.5$), Solid State Ionics 140 (2001) 89-96. https://doi.org/10.1016/S0167-2738(01)00696-8

[36] M. Liu, D. Wang, Preparation of $La_{1-z}Sr_zCo_{1-y}Fe_yO_{3-x}$ thin films, membranes, and coatings on dense and porous substrates, Journal of Materials Research 10 (1995) 3210-3221. https://doi.org/10.1557/JMR.1995.3210

[37] W. Jin, S. Li, P. Huang, N. Xu, J. Shi, Preparation of an asymmetric perovskite-type membrane and its oxygen permeability, Journal of Membrane Science 185 (2001) 237-243. https://doi.org/10.1016/S0376-7388(00)00650-5

[38] C. Xia, T.L. Ward, P. Atanasova, R.W. Schwartz, Metal-organic chemical vapor deposition of Sr–Co–Fe–O films on porous substrates, Journal of Materials Research 13 (1998) 173-179. https://doi.org/10.1557/JMR.1998.0023

[39] W. Deibert, F. Schulze-Küppers, E. Forster, M.E. Ivanova, M. Müller, W.A. Meulenberg, Stability and sintering of MgO as a substrate material for Lanthanum Tungstate membranes, Journal of the European Ceramic Society 37 (2017) 671-677. https://doi.org/10.1016/j.jeurceramsoc.2016.09.033

[40] T. Lee, Y. Yang, A. Jacobson, B. Abeles, M. Zhou, Oxygen permeation in dense $SrCo_{0.8}Fe_{0.2}O_{3-\delta}$ membranes: surface exchange kinetics versus bulk diffusion, Solid State Ionics 100 (1997) 77-85. https://doi.org/10.1016/S0167-2738(97)00257-9

[41] F. Buck, A. Feldhoff, J. Caro, T. Schiestel, Permeation improvement of LCCF hollow fiber membranes by spinning and sintering optimization, Separation and Purification Technology 259 (2021) 118023. https://doi.org/10.1016/j.seppur.2020.118023

[42] T. Schiestel, M. Kilgus, S. Peter, K. Caspary, H. Wang, J. Caro, Hollow fibre perovskite membranes for oxygen separation, Journal of Membrane Science 258 (2005) 1-4. https://doi.org/10.1016/j.memsci.2005.03.035

[43] T. Kida, S. Ninomiya, K. Watanabe, N. Yamazoe, K. Shimanoe, High oxygen permeation in $Ba_{0.95}La_{0.05}FeO_{3-\delta}$ membranes with surface modification, ACS Applied Materials & Interfaces 2 (2010) 2849-2853. https://doi.org/10.1021/am100524k

6. Effect of plasma atmosphere on the oxygen transport of mixed ionic and electronic conducting hollow fiber membranes

6.1. Summary

In this publication, the feasibility of the plasma induced CO_2 dissociation to oxygen and CO and the in situ separation of the oxygen were tested. Furthermore, the comparability of the plasma membrane reactor for air and CO_2 plasma to an oven heated systems was investigated. Firstly, hollow fiber membranes from LCCF, which have a good CO_2 tolerance as well as a high oxygen permeation, which were investigated in the three previous chapters, were spun and sintered at 1220 °C.

To improve the comparability the temperature inside the hollow fiber was measured in the plasma membrane reactor at different microwave powers. The gas flow for air and CO_2 was kept constant at 6 Nl min^{-1} to have a similar residence time of the plasma around the membrane. Furthermore, the working length of the membrane in the plasma was varied to find the effective membrane length of the hollow fiber in the plasma. The results in the air plasma showed an effective membrane length of 2 cm independent from the microwave power. The highest oxygen permeation (17.3 ml min^{-1} cm^{-2}) in an air plasma was measured at 0.5 cm membrane working length and a microwave power of 0.68 kW, which corresponds with a temperature of 1200 °C. Compared to the oven heated system the permeation is 60.6 % higher at 1000 °C. This indicates that the special atmosphere in the plasma improves the surface exchange kinetics.

In the CO_2 plasma the dissociation of CO_2 at different microwave powers could be measured and it is possible to separate oxygen from the plasma with LCCF hollow fiber membranes. The permeation reaches up to 5.0 ml min^{-1} cm^{-2}. Compared to the oven system, the permeation is 54.4 % lower because of the presence of CO.

6.2. Effect of plasma atmosphere on the oxygen transport of mixed ionic and electronic conducting hollow fiber membranes

Frederic Buck, Katharina Wiegers, Andreas Schulz, Thomas Schiestel

Review

Effect of plasma atmosphere on the oxygen transport of mixed ionic and electronic conducting hollow fiber membranes

F. Buck [a,b], K. Wiegers [c], A. Schulz [c], T. Schiestel [a,*]

[a] Fraunhofer Institute for Interfacial Engineering and Biotechnology IGB, 70569 Stuttgart, Germany
[b] Institute of Physical Chemistry and Electrochemistry, Leibniz Universität Hannover, 30167 Hannover, Germany
[c] Institute of Interfacial Process Engineering and Plasma Technology, Universität Stuttgart, 70569 Stuttgart, Germany

ARTICLE INFO

ABSTRACT

Perovskite hollow fibers have been used to extract oxygen from different oxygen containing plasmas. The influence of the working length and the temperature on the oxygen transport of $(La_{0.6}Ca_{0.4})(Co_{0.8}Fe_{0.2})O_{3-\delta}$ (LCCF) hollow fiber membranes in an air and a CO_2 plasma were investigated and compared with a conventional electrically heated oven system at a similar temperature. High-quality LCCF hollow fiber membranes were prepared via phase inversion spinning and sintering. In the CO_2 plasma, the feasibility of the oxygen extraction due to the CO_2 splitting according to $CO_2 \rightleftarrows CO + \frac{1}{2} O_2$ was studied. For an active membrane length of 0.5 cm, oxygen permeation values of 17.27 ml min^{-1} cm^{-2} in an air plasma at 0.67 kW and 4.97 ml min^{-1} cm^{-2} in a CO_2 plasma at 1 kW were reached.

Contents

* Corresponding author.
  E-mail address: Thomas.schiestel@igb.fraunhofer.de (T. Schiestel).

Introduction

Since the beginning of the industrial revolution in the 19th century, the importance of energy supply drastically increased [1]. Up to now, fossil fuels are still the most widely-used source for energy [1,2]. The disadvantage of this route is the emission of large amounts of the greenhouse gas CO_2 with a huge impact on global climate. Therefore, the conversion of CO_2 into value-added chemicals is one of the main challenges for the next decades. The CO_2 molecule is highly inert, therefore requiring a substantial energy input for any chemical conversion [3]. Due to the limitations of the traditional thermal approaches, several promising technologies are being developed, e.g. biological [4], electrochemical [5], solar thermochemical [6] or catalytic conversion [7]. In recent years, plasma technology [8–12] emerged as a new promising approach for CO_2 conversion. For the splitting of CO_2, warm plasmas seems to be very promising due to their operation at the boundary between non-thermal and thermal plasmas [12–14]. For this purpose an electrode-less microwave excited atmospheric plasma system (APS) is an excellent option [15]. This APS offers the advantages of high ion, radical and electron densities and a reduced electric field, which provides an excellent precondition for successful conversion of CO_2 [15–17]. These plasma conditions favour the excitation of the asymmetric mode vibrational levels of CO_2 [12,17]. The major disadvantage of this technology is the product separation [11]. Due to thermodynamics, the resulting products of high-temperature CO_2 splitting, $CO_2 \rightleftarrows CO + \frac{1}{2}O_2$, will recombine in the regions of lower temperature depending on the quenching rate [3]. To inhibit this recombination, Chen et al. [18] presented a new concept by combining a microwave plasma with ceramic hollow fiber membranes. The combination of these technologies has two major advantages: CO_2 can be decomposed and the remaining CO can be used to produce platform chemicals [18]. Moreover, as plasma generation is a flexible and quick process it is ideal to chemically store fluctuating renewable energies.

Membranes from mixed ionic and electronic conducting (MIEC) perovskite material can be used to separate oxygen from a gas mixture with a high selectivity [19–22]. At elevated temperatures (usually above 700 °C) not only electrons can pass through the membrane but also oxygen ions can diffuse through vacancies in the crystal lattice in the opposite direction [23,24]. The membranes can be manufactured in different geometries, like flat or tubular membranes, which are most common. A geometry with a high potential is the hollow fiber. MIEC hollow fiber membranes combine several advantages simultaneously like high specific surface area, thin walls with a low resistance against oxygen transport and at the same time very little material consumption [25]. Unfortunately, most of the known MIEC materials possess only a limited stability in the presence of CO_2 [26]. One material with a high CO_2 resistance is $(La_{0.6}Ca_{0.4})(Co_{0.8}Fe_{0.2})O_{3-\delta}$ (LCCF6482) [27,28]. It was already shown that hollow fiber membranes can be manufactured with the LCCF6482 material with a high oxygen permeation even in CO_2-containing atmospheres [18,25].

For any future application of plasma-membrane-reactors, a fundamental knowledge of the interaction between the plasma, the LCCF6482 hollow fiber membranes and the influencing factors (e.g. temperature profile over the membrane length, space- and temperature-resolved concentrations of CO and CO_2 in the plasma etc.) is necessary. For an accurate evaluation of plasma effects on oxygen transport, a precise control of experimental parameters is necessary. As temperature is the parameter with the most critical impact on oxygen transport, the control and measurement of temperature distribution in the plasma are crucial to determine the plasma effect on oxygen permeation. Another factor with a big influence is the composition of the plasma atmosphere and the

fraction of oxygen in it. For the evaluation of oxygen transport under an air or a CO_2 plasma and in a thermally heated oven with air or CO_2 atmosphere, the oxygen partial pressure and the temperature must be comparable in all four experiments. The findings of this work shall be used to further optimize the performance of the plasma membrane reactors for thermal CO_2 splitting.

Experimental

Hollow fiber preparation

The perovskite powder LCCF6482 was prepared by Cerpotech (Tiller, Norway) using a spray pyrolysis process. The hollow fibers were manufactured by a phase inversion and sintering technique, which was described elsewhere [22]. The spinning solution consisted of 58.02 wt% LCCF powder, 34.41 wt% N-Ethyl-2-Pyrrolli done (NEP, $\geq$ 98 %, Carl Roth GmbH + Co KG, Karlsruhe, Germany) and 7.57 wt% Polyetherimide (Merck KGaA, Darmstadt, Germany). For the spinning process, deionised water (DI) was used as external coagulant and for the bore fluid a mixture of DI water /NEP (25 vol % / 75 vol%) was used. The hollow fibers were spun with a spinneret of D_o/D_i 2.0/1.2 mm and sintered at a temperature of 1220 °C. All manufacturing parameters are shown in Table 1.

Oxygen permeation devices: oven and plasma reactor

Oxygen permeation in a heated oven

The set up for the measurement of oxygen permeation of the LCCF hollow fiber in the conventional oven was described in detail elsewhere [22]. O_2, CO_2 and N_2 were injected to the feed side. In this study, the feed side is outside the hollow fiber, in order to allow a direct comparison with the results of the plasma configuration. Argon was injected into the lumen of the hollow fiber (sweep side). For all the measurements, the sweep flow was kept constant at 140 Nml min^{-1}. For comparison with the air plasma the total feed flow was 130 Nml min^{-1} with a mixture of 20.6 vol% O_2 and 79.4 vol% N_2. For comparison with the CO_2 plasma, the total feed flow was 130 Nml min^{-1} with a mixture of 4.9 vol % O_2, 7.5 vol% N_2 and 87.6 vol% CO_2. The flow velocity of the feed flow is 662.1 $\frac{m}{min}$ with an inner diameter of the membrane containing steel tube of 5 mm. The oxygen concentration of sweep and feed flow were measured with an oxygen analyser (Zirox SGM 7). To guarantee isothermal conditions, the hollow fibers were coated with a gold paste (ChemPur, Karlsruhe, Germany) with the exception of 1 cm in the middle of the fibers, and sintered at 950 °C. This process was repeated three times. Therefore, it was possible to define an effective isothermal membrane length of 1 cm. For the plasma experiments, the uncoated length was varied between 4 cm and 0.5 cm to minimize effects of temperature gradients in the plasma torch.

Table 1
Parameters of the manufacturing of LCCF hollow fiber membranes for oxygen permeation studies.

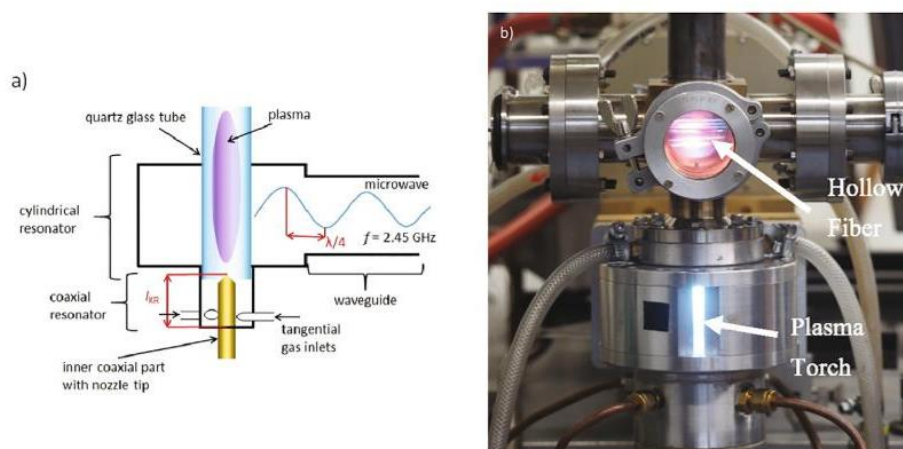| Experimental parameters	Values	
Dimensions of spinneret:		
• $D_{outside}$	2.0 mm	
• D_{inside}	1.2 mm	
Bore liquid	DI water/NEP (25 vol% / 75 vol%)	
Flow rate of the bore liquid	7.5	cm³ min^{-1}
External coagulant	DI water	
Air gap	0	cm
Sintering conditions		
• Temperature	1220	°C
• Time	16	h

2

Fig. 1. a) Schematic diagram of the plasma torch. b) Plasma membrane reactor in operation; Hollow fiber membrane is placed perpendicular above the plasma torch.
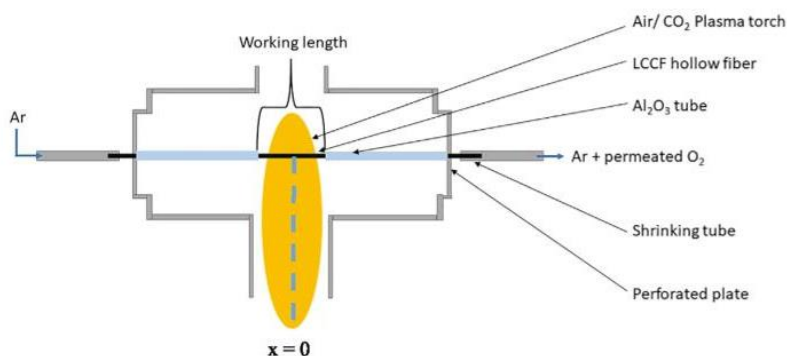

Fig. 2. Schematic set up of the plasma membrane reactor (front view).

Microwave plasma membrane reactor. A microwave plasma torch at atmospheric pressure was used as plasma source. Fig. 1 a) shows a schematic diagram of the plasma torch configuration. It consists of a broadband cylinder and a narrowband coaxial resonator (Muegge GmbH, Reichelsheim, Germany). Resonance can be generated if a microwave with a frequency of 2.45 GHz is induced into the combination of the two resonators via a waveguide and if the length of the coaxial resonator I_{KR} corresponds exactly to a quarter wavelength of the microwave. This creates a very high electric field at the tip of the coaxial inner conductor, thus igniting the plasma. After ignition, the plasma switches to a cylinder mode, i.e. the operation condition. The gas can be supplied via four tangential inlets. The inflow via the tangential gas inlets leads to a rotational flow, which stabilize the plasma in the center of the quartz glass tube. Thus, the plasma torch enables independent ignition and can be operated in a freestanding modus (see Fig. 1 b), which ensures a maintenance-free operation. The gas flow in the plasma was set to 6 Nl min^{-1} for the air plasma as well as for the CO_2 plasma. The flow velocity is 558.1 $\frac{m}{min}$ with an inner diameter of the plasma chamber of 37 mm.

Oxygen permeation in a plasma membrane reactor

The membrane reactor holding the hollow fiber is placed on top of the plasma torch. In Fig. 2, the schematic set up is shown. The hollow fiber membranes were fixed with a perforated plate and a shrinking tube. An argon flow of 140 ml min^{-1} was injected inside the hollow fiber. The plasma flow was 6 Nl min^{-1}. The oxygen concentration of the sweep flow was also measured by means of an oxygen analyser (Zirox SGM 7). The spectroscopy port, orthogonal to the membrane mounting, provides a view of the plasma and the hollow fiber, ensuring that the fiber is always located at the same position. Due to the hot plasma, the capillary begins to glow. To define the working length an Al_2O_3 tube (D_o/D_i 4.0/2.0 mm) (Friatech AG, Mannheim, Germany) was cut into the desired length and glued to the perforated plate. Furthermore, the fibers were coated with gold in the area of the Al_2O_3 tube. This construction allows to vary the working length of the membrane in the 4 cm to 0.5 cm range.

The oxygen permeation J_{O2} (ml cm^{-2} min^{-1}) can be calculated by means of the following equation:

$$J_{O2} = \frac{c_{O2} \cdot \dot{V}_s}{A_{Membrane}} \quad (1)$$

Here, c_{O2} is the oxygen concentration (in vol%) in the sweep flow, $\dot{V}_s$ the sweep flow (Nml min^{-1}) and $A_{Membrane}$ the membrane area (cm^2). To calculate the membrane area of a hollow fiber the logarithmic mean is used:

$$A_{Membrane} = \frac{\pi \cdot L \cdot (D_o - D_i)}{ln\left(\frac{D_o}{D_i}\right)} \quad (2)$$
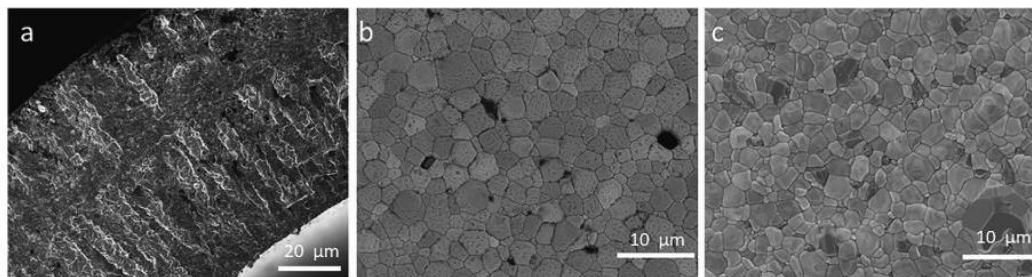
3

Fig. 3. SEM micrograph of LCCF hollow fiber cross section (a), outer surface (b) and inner surface (c), spun with D_o = 2.0 mm spinneret and sintered at 1220 °C.
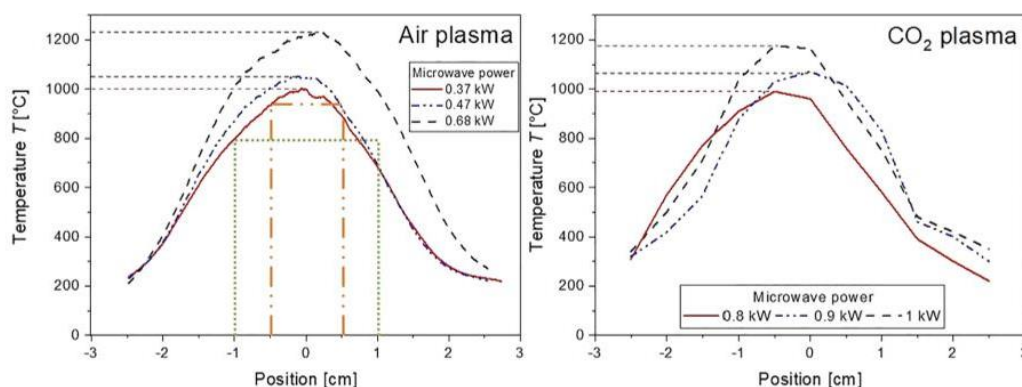

Fig. 4. Temperature profile at different microwave power output with 6 Nl min^{-1} gas flow for air plasma (left) CO_2 plasma (right). The orange dash/dot/dot line symbolises 1 cm membrane working length and the green dotted line 2 cm membrane working length.

With D_o as outer and D_i as inner diameter of the hollow fiber and the effective membrane length L.

Characterization of the plasma

The temperature profile of the different plasmas was measured with a thermocouple type N with an outer diameter of 0.5 mm (Mantelrohr Nicrotherm D^{TM} (1250 °C), TC Direct, Mönchengladbach, Germany). In order to avoid destruction of the thermocouple by the plasma, the temperature profile is measured inside the hollow fiber. The starting point (x = 0 (Fig. 2)) is the middle of the membrane reactor. The temperature was measured over a total length of 6 cm.

The splitting rates of CO_2 for the different powers in the CO_2 were measured with a mass spectrometer. The samples are taken at the x = 0 position with a metal capillary.

Results and discussion

Morphology of LCCF hollow fiber

The optimization of LCCF hollow fiber membranes has been already described in detail in our previous work [25]. The fibers used in this study have an outer diameter of 1.20 mm and an inner diameter of 0.85 mm with a wall thickness of 175 μm. The hollow fibers are tested for gas tightness up to 5 bars and show a good bending strength of 128 MPa. The SEM micrograph shows no porosity on the outer surface (Fig. 3, right). In the cross section, some radially aligned elongated pores are visible (Fig. 3, left). These pores are a typical by-product for hollow fibers manufactured by phase inversion process.
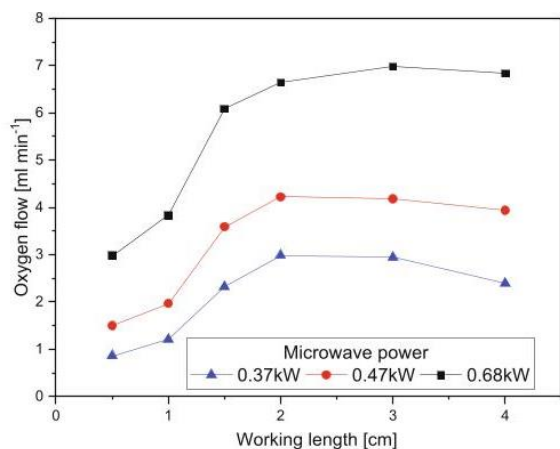
Temperature profile in the plasma

As temperature has a strong influence on oxygen permeation of MIEC membranes [25], the determination of the temperature profile in the plasma is a basic requirement for any comparison of oxygen transport. Fig. 4 shows the temperature for air and CO_2 plasma depending on the x-position. The gas flow is in both cases 6 Nl min^{-1}, to have a similar residence time of the plasma around the membrane. In addition, the power output of the microwave generator was varied to have similar peak temperatures in the different plasmas. This approach allows a direct comparison of oxygen permeation in both plasmas. It follows from Fig. 4 that similar temperature profiles can be obtained for 0.37 kW air plasma and 0.8 kW CO_2 plasma, for 0.47 kW air plasma and 0.9 kW CO_2 plasma, and 0.68 kW air plasma and 1.0 kW CO_2 plasma.

Oxygen permeation in air plasma

In order to define the area in which the oxygen permeates, it is necessary to consider the oxygen flow through the membrane. Fig. 5 shows the oxygen flow as a function of the working length at different microwave power in an air plasma. The air flow for the plasma was set to 6 Nl min^{-1} and the sweep gas flow was kept at 140 Nml min^{-1}. The working length of the hollow fiber was varied between 0.5 cm and 4 cm. It can be clearly seen that the oxygen flow reaches a saturation at a working length of 2 cm. This means that the membrane outside of this zone does not contribute to any
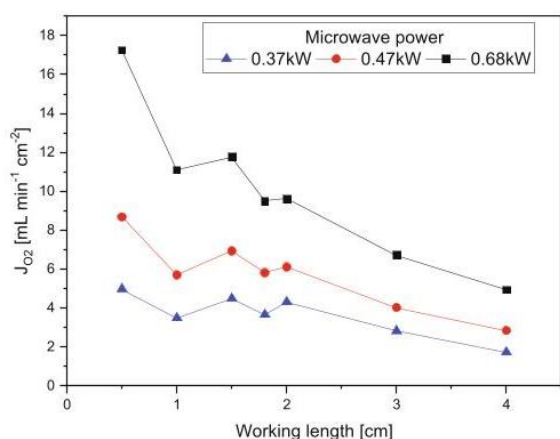
4

Fig. 5. Oxygen flow of LCCF hollow fiber as a function of microwave power and working length of the membrane in an air plasma. Experimental: Gas flow 6 Nl min^{-1}, sweep flow Ar inside the hollow fiber 140 Nml min^{-1}. The temperature profile for the different microwave power is shown in Fig. 4.

oxygen transport due to its low temperature. Therefore, an almost linear increase of the amount of the permeated oxygen is observed with up to 2 cm membrane length. Furthermore, no widening of the active hollow fiber length for increasing the microwave power seems to occur.

Fig. 6 shows the oxygen permeation in dependence on the working length at different microwave power in an air plasma. As expected, the oxygen permeation increases with increasing microwave power. The oxygen permeation through the hollow fiber with a working length of 0.5 cm increases from 4.98 ml min^{-1} cm^{-2} at 0.37 kW ($\sim$1000 °C) up to 17.27 ml min^{-1} cm^{-2} at 0.68 kW ($\sim$1200 °C).

In our previous publication [29], the oxygen permeation was 2.24 ml min^{-1} cm^{-2} at 1000 °C (1 kW) but at a higher gas flow of 25 Nl min^{-1} which means a power per flow ratio of 0.04 kW min Nl^{-1}. Now, we work with a power per flow ratio of

0.0617 kW min Nl^{-1}, which explains the higher oxygen permeation values.

Furthermore, an increasing dependence of the permeation on the effective membrane area can be seen by increasing the microwave power. At 0.68 kW microwave power, the permeation increases by 156 % with a decrease of the working length from 3 cm to 0.5 cm. This finding can be explained by the sharp temperature profile (see Fig. 4; left image). At 0.68 kW, the temperature drops from 1200 °C by 200 °C in less than 1 cm. Therefore, the permeation deteriorates with increasing distance from the centre. The same effect can be seen for lower microwave power but not as strongly pronounced as at 0.68 kW.
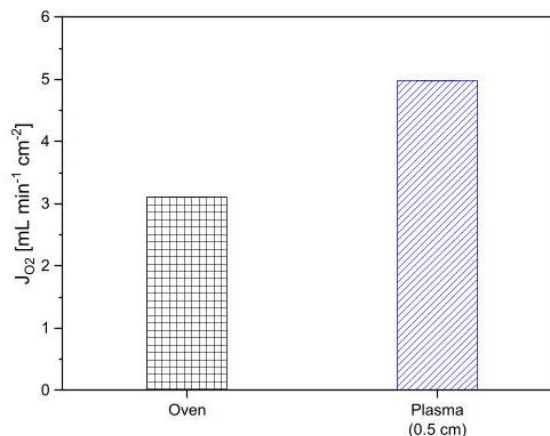
Fig. 7 shows the oxygen permeation through a LCCF hollow fiber in the conventional oven system and in the air plasma. To compare the results, the similar temperature must be adjusted at the membrane site in both systems. The plasma measurements at 0.5 cm working length was used for comparison as this is the measurement with the smallest temperature gradient over the working length. The oxygen permeation in the plasma (4.98 ml min^{-1} cm^{-2}) is 60.6 % higher than the one measured in the oven (3.10 ml min^{-1} cm^{-2}). The higher oxygen permeation in the plasma can be explained by the special plasma atmosphere. In the conventional oven, the oxygen dissociates at the surface of the membrane, by means of the following equation:

$$O_2(g) + 4e^- \rightarrow 2O^{2-} \qquad [3]$$

In the plasma, the oxygen molecules are partly dissociated before reaching the surface, whereby this energy-consuming step can left out. This might lead to an acceleration of surface exchange kinetics in the plasma phase.

Oxygen permeation in CO$_2$ plasma

To figure out the effective membrane length, the oxygen flow as a function of the different microwave power in a CO$_2$ plasma is shown in Fig. 8. The CO$_2$ flow for the plasma was set to 6 Nl min^{-1} and the Ar sweep gas flow was 140 Nml min^{-1}. The working length of the hollow fiber varied between 4 cm and 0.5 cm. First of all, it can be seen that the feasibility of the conversion of CO$_2$ in CO and oxygen is proven and the generated oxygen can be extracted

Fig. 6. Oxygen permeation of LCCF hollow fiber for different microwave power as a function of the working length of the hollow fiber in an air plasma. Experimental: Gas flow of the air plasma 6 Nl min^{-1}, sweep flow Ar inside the hollow fiber 140 Nml min^{-1}. The temperature profile for the different microwave power is shown in Fig. 4.

**Fig. 7.** Oxygen permeation of LCCF hollow fiber in a conventional electrically heated oven and in an air plasma. Experimental of oven: Feed flow 130 Nml min^{-2} air and 140 ml min^{-1} Ar as sweep, oven temperature 1000 °C. Experimental of air plasma: Plasma flow 6 Nl min^{-1}, flow of sweep gas Ar inside the hollow fiber 140 Nml min^{-1}, plasma power 0.37 kW, working length of fiber 0.5 cm, temperature ca. 1000 °C.
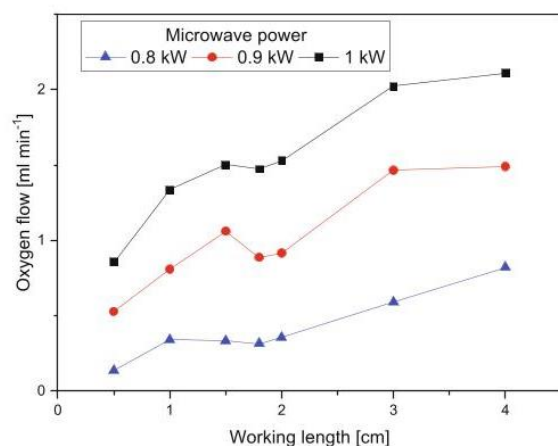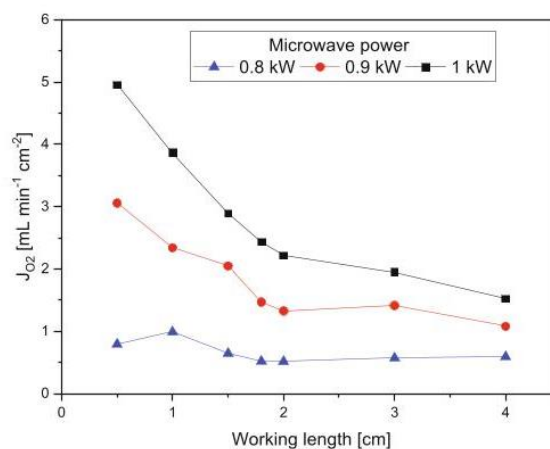
Fig. 8. Oxygen flow of LCCF hollow fiber as a function of microwave power and working length in a CO_2 plasma. Experimental: Gas flow of CO_2 plasma 6 Nl min^{-1}, sweep flow Ar inside the hollow fiber 140 Nml min^{-1}. The temperature profile for the different microwave power is shown in Fig. 4.

Fig. 9. Oxygen permeation (area-normalised oxygen flow as shown in Fig. 8) of the LCCF hollow fiber for different microwave power as a function of working length in a CO_2 plasma. Experimental: Gas flow of CO_2 plasma is 6 Nl min^{-1}, sweep flow Ar inside the hollow fiber 140 Nml min^{-1}. The temperature profile for the different microwave power is shown in Fig. 4.

through an MIEC membrane. Depending on the microwave power, different amounts of oxygen can be separated through the membrane. The splitting rates of CO_2 were measured with a mass spectrometer. The gas composition is determined at the x = 0 position. The relevant parameters for different microwave powers are given in Table 2. It can be seen that with increasing microwave power the CO_2 conversion increases and correspondingly higher O_2 concentrations from 4.9 vol% to 6.0 vol% are found in the quenched plasma gas. This means that the rate of quenching the plasma gas influences the oxygen content.

In contrast to the air plasma, the oxygen flow reaches the saturation level at an effective membrane length of 3 cm for 0.9 kW and 1.0 kW. This tendency cannot be seen for the measurements at 0.8 kW. This finding could be explained by the flickering of the plasma torch along the hollow fiber since at low power the torch is less stable. Such fluctuations are less pronounced with increasing microwave power. Therefore, for the lowest power output it is difficult to define an effective membrane length for oxygen permeation.

In Fig. 9, the oxygen permeation as a function of the working length at different microwave powers in a CO_2 plasma is shown. As expected, the oxygen permeation increases with increasing microwave power. For the hollow fiber with an exchange area of 0.5 cm the oxygen permeation increases from 0.79 ml min^{-1} cm^{-2} at 0.8 kW ($\sim$1000 °C) up to 4.96 ml min^{-1} cm^{-2} at 1.0 kW ($\sim$1200 °C).

Chen et al. [18] measured an oxygen permeation of 4 ml min^{-1} cm^{-2} with La$_{0.6}$Ca$_{0.4}$Co$_{0.5}$Fe$_{0.5}$O$_{3-\delta}$ (LCCF) and a microwave power of 1 kW. The assumed working length of Chen et al. was 2 cm. The comparability is difficult due to different definition of the working length and the different composition of the LCCF. The higher iron fraction in the perovskite, used by Chen et al. also has a positive influence on the oxygen permeation [30].
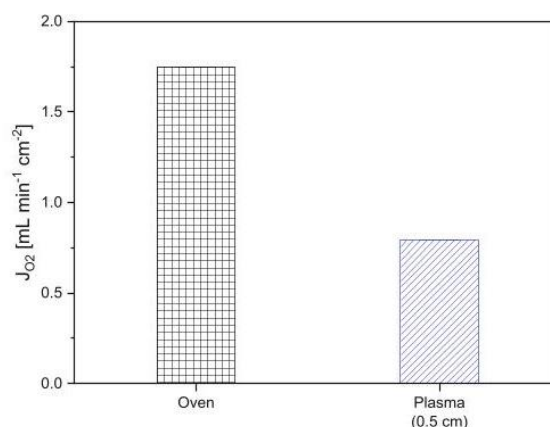
Furthermore, Fig. 9 shows that for 0.9 kW and 1.0 kW the permeation decreases with increasing working length – like for the air plasma. Exact permeation measurements below a working length of 0.5 cm are not reasonable due to increasing errors in separation area definition. Furthermore, for a working length of 0.5 cm the temperature distribution is nearly constant. However, for a working length of 0.5 cm the temperature gradient in the separation zone is minimized.

Fig. 10. shows the oxygen permeation in the conventional oven system and in the CO_2 plasma for a working length of 0.5 cm. To compare the oxygen permeation in oven and plasma, the data for a microwave power of 0.8 kW at 1000 °C were used. As stated above, the composition of the plasma gas (88.0 vol% CO_2, 7.7 vol% CO, 4.3 vol% O_2) is not the thermodynamic equilibrium composi-

Table 2
Gas composition in dependence of the microwave power in a CO_2 plasma with a gas flow of 6 Nl min^{-1}.

Power [kW]	CO_2 [vol%]	CO [vol%]	O_2 [vol%]
0.8	88.0 ± 1.0	7.7 ± 1.0	4.3 ± 1.0
0.9	85.7 ± 1.0	9.1 ± 1.0	5.2 ± 1.0
1.0	83.6 ± 1.0	10.6 ± 1.0	5.8 ± 1.0

Fig. 10. Oxygen permeation of LCCF hollow fiber for a conventional electrically heated oven and for a CO_2 plasma. Experimental of oven: Total feed flow 130 Nml min^{-1}, composition feed gas 4.3 vol% O_2, 7.7 vol% N_2 and 88.0 vol% CO_2 thus simulation the composition of the CO_2 plasma gas at the site of the membrane, sweep flow 140 Nml min^{-1} Ar, oven temperature 1000 °C. Experimental of CO_2 plasma: Plasma flow 6 Nl min^{-1}, sweep gas flow inside the hollow fiber 140 Nml min^{-1} Ar, microwave power of the CO_2 plasma 0.8 kW, working length of the fiber 0.5 cm.

tion at 1000 °C but a result of the interplay of microwave power and quenching. Therefore, a synthetic gas mixture with a comparable oxygen partial pressure has been prepared for the permeation experiment in the oven (4.3 vol% O_2, 7.7 vol% N_2 and 88.0 vol% CO_2). Surprisingly, the oxygen permeation in the oven (1.74 ml min^{-1} cm^{-2}) is 119.1 % higher than the one in the CO_2 plasma with a working length of 0.5 cm. The negative effect in the latter case can be explained by the presence of other species in the CO_2 plasma. It is well known that CO_2 can chemically adsorb at the surface of LCCF membranes and thereby can block available oxygen vacancies [25]. We suggest due to the higher reactivity of CO compared to CO_2 that CO can also chemically adsorb on these oxygen vacancy sites on the membrane surface, thus could result in an additional competitive factor for the O_2 adsorption.

Conclusions

In this work, the perovskite LCCF6482, which is well known to be CO_2-tolerant, was used to manufacture hollow fiber membranes. The oxygen permeation through these hollow fibers was tested in an air plasma as well as in a CO_2 plasma. Furthermore, tests in an electrically heated oven at similar temperature and with the same gas mixtures were carried out.

With rising microwave power of an air plasma, the oxygen permeation increases up to 17.27 ml min^{-1} cm^{-2}. In comparison to the conventional oven at the same temperature, the permeation is 60 % higher, most probably due to the active oxygen species formed in the air plasma and being still alive after quenching the plasma gas to 1000 °C.

The feasibility of oxygen extraction from CO_2 splitting in a carbon dioxide plasma due to $CO_2 \rightleftarrows CO + \frac{1}{2} O_2$ was evaluated. After quenching the CO_2 plasma gas to 1000 °C, the oxygen content was still 4.3 vol% and it is possible to separate this oxygen from a CO_2 plasma by a MIEC membrane. In the CO_2 plasma, the effective membrane length is dependent on the microwave power. For a microwave power above 0.8 kW, the effective membrane length is 3 cm. Furthermore, the oxygen permeation increases up to 4.96 ml min^{-1} cm^{-2} with increasing microwave power and decreasing membrane length. In comparison to the conventional oven, the oxygen permeation from the plasma gas is 54.4 % lower because of the presence of competing species like CO, which can block oxygen vacancy sites on the membrane surface.

With this study, the effective membrane length in the plasma membrane concept was investigated in detail for the first time. These results allow a direct comparison between permeation in a conventional oven and in air or CO_2 plasmas. These findings enable a further optimization of oxygen separation from a CO_2 plasma.

Declaration of Competing Interest

The authors declare that they have no known competing financial interests or personal relationships that could have appeared to influence the work reported in this paper.

Acknowledgement

References

[1] S. Dyatlov, N. Didenko, E. Ivanova, E. Soshneva, S. Kulik, I.O.P. Conf Ser.: Earth Environ. Sci. 434 (2020), https://doi.org/10.1088/1755-1315/434/1/012014.

[2] [2] IEA, CO2 emissions from fuel combustion. https://www.iea.org/reports/world-energy-outlook-2020, 2020 (accessed 15 June 2021).

[3] H.S. Kwak, H.S. Uhm, Y.C. Hong, E.H. Choi, Sci. Rep. 5 (2015) 1–13, https://doi.org/10.1038/srep18436.

[4] P.M. Schenk, S.R. Thomas-Hall, E. Stephens, U.C. Marx, J.H. Mussgnug, C. Posten, O. Kruse, B. Hankamer, Bioenergy research 1 (2008) 20–43, https://doi.org/10.1007/s12155-008-9008-8.

[5] J. Albo, M. Alvarez-Guerra, P. Castaño, A. Irabien, Green Chem. 17 (2015) 2304–2324, https://doi.org/10.1039/C4GC02453B.

[6] W. Liang, Z. Cao, G. He, J.r. Caro, H. Jiang, ACS Sustainable Chemistry & Engineering, 5 (2017) 8657-8662. https://doi.org/10.1021/acssuschemeng.7b01305

[7] C.M. Marin, E.J. Popczun, T.-D. Nguyen-Phan, D. Alfonso, I. Waluyo, A. Hunt, D. R. Kauffman, Appl. Catal. B Environ. 284 (2021), https://doi.org/10.1016/j.apcatb.2020.119711.

[8] A. Bogaerts, A. Berthelot, S. Heijkers, S. Kolev, R. Snoeckx, S. Sun, G. Trenchev, K. Van Laer, W. Wang, Plasma Sour. Sci. Technol. 26 (2017), https://doi.org/10.1088/1361-6595/aa6ada.

[9] B. Ashford, X. Tu, Curr. Opin. Green Sustain. Chem. 3 (2017) 45–49, https://doi.org/10.1016/j.cogsc.2016.12.001.

[10] A. Bogaerts, E.C. Neyts, ACS Energy Lett. 3 (2018) 1013–1027, https://doi.org/10.1021/acsenergylett.8b00184.

[11] K.D. Weltmann, J.F. Kolb, M. Holub, D. Uhrlandt, M. Šimek, K. Ostrikov, S. Hamaguchi, U. Cvelbar, M. Černák, B. Locke, Plasma Process. Polym. 16 (2019) 1800118, https://doi.org/10.1002/ppap.201800118.

[12] A. Bogaerts, T. Kozák, K. Van Laer, R. Snoeckx, Faraday Discuss. 183 (2015) 217–232, https://doi.org/10.1039/C5FD00053J.

[13] A. Fridman, Plasma chemistry, Cambridge University Press, 2008.

[14] R. Snoeckx, A. Bogaerts, Chem. Soc. Rev. 46 (2017) 5805–5863, https://doi.org/10.1039/C6CS00066E.

[15] M. Leins, K.M. Baumgärtner, M. Walker, A. Schulz, U. Schumacher, U. Stroth, Plasma Process. Polym. 4 (2007) S493–S497, https://doi.org/10.1002/ppap.200731213.

[16] C. Tendero, C. Tixier, P. Tristant, J. Desmaison, P. Leprince, Spectrochim. Acta Part B Atom. Spectr. 61 (2006) 2–30, https://doi.org/10.1016/j.sab.2005.10.003.

[17] V. Rusanov, A. Fridman, G. Sholin, Soviet Phys. Uspekhi 24 (1981) 447, https://doi.org/10.1070/PU1981v024n06ABEH004884.

[18] G. Chen, F. Buck, I. Kistner, M. Widenmeyer, T. Schiestel, A. Schulz, M. Walker, A. Weidenkaff, Chem. Eng. J. (2019), https://doi.org/10.1016/j.cej.2019.123699.

[19] Y. Teraoka, T. Nobunaga, N. Yamazoe, Chem. Lett. 17 (1988) 503–506, https://doi.org/10.1246/cl.1988.503.

[20] A.J. Burggraaf, L. Cot, Fundamentals of inorganic membrane science and technology, fourth ed., Elsevier, 1996.

[21] J. Stevenson, T. Armstrong, R. Carneim, L. Pederson, W. Weber, J. Electrochem. Soc. 143 (1996) 2722, https://doi.org/10.1149/1.1837098.

[22] T. Schiestel, M. Kilgus, S. Peter, K. Caspary, H. Wang, J. Caro, J. Membr. Sci. 258 (2005) 1–4, https://doi.org/10.1016/j.memsci.2005.03.035.

[23] A. Feldhoff, J. Martynczuk, M. Arnold, M. Myndyk, I. Bergmann, V. Šepelák, W. Gruner, U. Vogt, A. Hähnel, J. Woltersdorf, J. Solid State Chem. 182 (2009) 2961–2971, https://doi.org/10.1016/j.jssc.2009.07.058.

[24] C. Li, J.J. Chew, A. Mahmoud, S. Liu, J. Sunarso, J. Membr. Sci. 567 (2018) 228–260, https://doi.org/10.1016/j.memsci.2018.09.016.

[25] F. Buck, A. Feldhoff, J. Caro, T. Schiestel, Separ. Purificat. Technol. 259 (2021), https://doi.org/10.1016/j.seppur.2020.118023.

[26] O. Czuprat, M. Arnold, S. Schirrmeister, T. Schiestel, J. Caro, J. Membr. Sci. 364 (2010) 132–137, https://doi.org/10.1016/j.memsci.2010.08.019.

[27] K. Efimov, T. Klande, N. Juditzki, A. Feldhoff, J. Membr. Sci. 389 (2012) 205–215, https://doi.org/10.1016/j.memsci.2011.10.030.

[28] M. Salehi, M. Søgaard, V. Esposito, S.P.V. Foghmoes, E. Persoon, M. Schroeder, P. V. Hendriksen, J. Membr. Sci. 542 (2017) 245–253, https://doi.org/10.1016/j.memsci.2017.07.050.

[29] F. Buck, I. Kistner, C. Rosler, A. Schulz, M. Walker, G. Tovar, T. Schiestel, Chem. Ingenieur Tech. 91 (2019) 1117–1122, https://doi.org/10.1002/cite.201900048.

[30] G. Chen, W. Liu, M. Widenmeyer, P. Ying, M. Dou, W. Xie, C. Bubeck, L. Wang, M. Fyta, A. Feldhoff, J. Membr. Sci. 590 (2019), https://doi.org/10.1016/j.memsci.2019.05.007.

7. Conclusions and outlook

This thesis deals with the mixed ionic and electronic conducting material $(La_{0.6}Ca_{0.4})(Co_{0.8}Fe_{0.2})O_{3-\delta}$ (LCCF) in the form of hollow fiber membranes for the oxygen separation from a CO_2 plasma. The membrane material crystallizes in a cubic perovskite structure. This material has the potential to selectively transport oxygen ions through the membrane at high temperatures (>700 °C). Through direct integration into a CO_2 plasma, the products (CO and O_2) can be separated instantly.

The results of the thesis are separated in four chapters.

In chapter 3, the hollow fiber membrane manufacturing via the non-solvent induced phase inversion (NIPS) and sintering process is described. The negative influence of sulphur containing polymer binders on the oxygen permeation could be shown. The good CO_2 stability in sulphur free LCCF hollow fibers could be investigated with a long-term oxygen permeation test in an oven heated system at 900 °C. Furthermore, first successful experiments in an air plasma were performed to investigate the thermal shock resistance. According to the good results from chapter 3 in relation to the CO_2 stability and the thermal shock resistance, the optimization of the membrane with respect to oxygen permeation was investigated in the following chapters 4 and 5.

In chapter 4, the bulk diffusion was optimized by reducing the wall thickness via different spinneret geometries and by manipulating the grain sizes of the membrane via sintering temperature variation. The LCCF phase contains different amounts of brownmillerite and a spinel-type cobalt oxide phase as foreign phase, depending on the sintering temperatures. The variation of the sintering temperature also showed that grain boundaries act as barriers for the oxygen diffusion. Therefore, higher sintering temperatures are favoured as these lead to bigger grains. The permeation flux could be improved by increasing sintering temperature (1220 °C) and reducing wall thickness (81 µm) up to 6.16 ml min^{-1} cm^{-2} at 1000 °C. However, the results showed that the oxygen permeation through the membrane is not only dominated by the bulk diffusion but also by the surface exchange kinetics. Therefore, further optimization approaches were made in chapter 5.

Two promising optimization paths were investigated to further improve the oxygen permeation flux of the CO_2 stable LCCF hollow fiber membranes. On the one hand, both limiting processes (bulk diffusion and surface exchange kinetics) were optimized via asymmetric hollow fibers. Here, a porous support of LCCF and a dense coating of LCCF were manufactured via wet spinning, dip coating and co-sintering. On the other hand, the surface exchange reactions were optimized via surface etching with H_2SO_4. Here, the inner, outer and both surfaces were

modified not only to investigate the overall surface reactions but also the surface reactions on each side.

Dense layer of 22 µm thickness on a porous support could be achieved by a one-step sintering process. This new manufacturing process offers the potential of significant reduction of the costs. The mechanical stability and the porosity of the support are strongly dependent on the sintering temperature but contrary to each other. Therefore, a compromise was made with a sintering temperature of 1170 °C. The oxygen permeation of this asymmetric hollow fiber showed an increase by 68.6 % in comparison to a dense hollow fiber with a wall thickness of 179 µm. The long-term stability (> 250 h) at 900 °C could also be confirmed.

The oxygen permeation of surface modified hollow fibers showed a dependency on the etching time and the etching area. The etching of the inner side (oxygen rich side) leads to the smallest increase of the oxygen permeation (30.2 %) and the etching of both areas leads to the largest increase (86.0 %). Furthermore, the results showed that the improvement factor decreases with increasing operating temperature. This indicates that the bulk diffusion has a smaller influence at lower temperatures.

In the final chapter (chapter 6) the applicability of the LCCF hollow fiber in different plasmas and the comparability of the oxygen transport behaviour in comparison to a conventional oven system were investigated. The microwave power of the air and the CO_2 plasma as adjustable parameter of the plasma was set to establish similar working temperatures in the permeation experiments. Therefore, it was possible to compare the results of the oven system and the plasma system. The results showed that the permeation in an air plasma is 60.6 % higher than in the oven system at similar temperatures. This indicates that the special atmosphere, with oxygen ions and radicals, optimize the surface exchange kinetics. The experiments in the CO_2 plasma showed on the one hand that it is possible to dissociate the CO_2 and on the other hand that the oxygen can be extracted from the plasma. After quenching, the CO_2 plasma to 1000 °C the oxygen content was still 4.3 %. From the thermodynamic perspective the oxygen amount should be close to zero. In comparison to the oven system, the oxygen permeation in the CO_2 plasma is 54.4 % lower due to the presence of CO.

In this work MIEC hollow fiber membranes were successfully used for the first time in a plasma. It could be demonstrated that such membranes can separate oxygen from a microwave plasma, which can split CO_2 in CO and O.

The oxygen permeation results of the LCCF hollow fibers in the oven system and in the plasma system can be used to develop membrane modules for a more effective oxygen separation. Thereby, the application could grow from the lab scale system up to an industrial process.

For the concrete application of such membranes in a *Plasma-Membrane-Reactor* (PMR), not only the membrane separation has to be improved, but also the plasma reaction and the integration of reaction and separation process. In a parallel Ph.D. at IGVP, Katharina Wiegers made fundamental studies to control and understand the CO_2 plasma. The plasma torch enables independent ignition and can be operated in a freestanding modus, which ensures a maintenance-free operation. The biggest challenge for the PMR seems to be the integration of sufficient separation area. Therefore, it would be helpful if both flow rate and temperature gradients in the plasma could be reduced. On the one hand side, this would allow a longer contact time of oxygen species with the membrane surface and on the other side, the membrane area could be used more efficient.

There are a couple of interesting questions to be answered in the next step:

- How will the increasing number of membranes in the plasma influence the temperature gradients and the flow rate distribution in the plasma?
- Is it possible to increase the exchange area by widening the plasma with different plasma nozzle geometries? And if, how does it influence the temperature distribution and the dissociation rate of CO_2
- Is it possible to address separation from the plasma at different levels, which means different temperature with membranes with various working temperatures?
- Is it possible to add other possible reaction partners, like hydrogen or even water, directly to the plasma to initiate reactions with CO to high value products?

This work could only be the first step in a hopefully not to long line to come to a *Plasma-Membrane-Reactor* for CO_2 splitting and therefore be a part of a Power-to-X economy.

Curriculum Vitae

Personal Information

Name	Frederic Felix Buck
Address	Breslauer Straße 5
	71254 Ditzingen
Date of Birth	25.05.1991
Place of Birth	Heilbronn
Nationality	German

Education

03/2018 - now	Ph.D. Candidate
	Gottfried Wilhelm Leibniz Universität Hannover
10/2015 - 12/2017	Master degree study
	Chemical Engineering
	Technische Universität München
10/2011 - 09/2015	Bachelor degree study
	Chemical Engineering
	Technische Universität München
09/2001 - 06/2010	Abitur
	Albert-Schweitzer Gymnasium Neckarsulm

Work experience

03/2018 - now	Research associate
	Fraunhofer-Institut für Grenzflächen- und
	Bioverfahrenstechnik IGB
07/2017 - 12/2017	Master Thesis
	MAN Diesel und Turbo Augsburg
03/2015 - 08/2015	Internship
	BMW Group München

Publications and Conferences

Publications included in this thesis

1. **F. Buck**, I. Kistner, C. Rösler, A. Schulz, M. Walker, G. Tovar, T. Schiestel, Einsatz von perowskitischen Hohlfasermembranen in einem Mikrowellenplasma. **Chem. Ing. Tech.** (2019), 91, No. 8, 1117-1122

2. **F. Buck**, A. Feldhoff, J. Caro, T. Schiestel, Permeation improvement of LCCF hollow fiber membranes by spinning and sintering optimization. **Separation and Purification Technology** (2021), 259, 118023

3. **F. Buck**, O. Bunjaku, J. Caro, T. Schiestel, High-flux CO_2-stable oxygen transport hollow fiber membranes through surface engineering. (Submitted to **Journal of the European Ceramic Society**)

4. **F. Buck**, K. Wiegers, A. Schulz, T. Schiestel, Effect of plasma atmosphere on the oxygen transport of mixed ionic and electronic conducting hollow fiber membranes. **Journal of Industrial and Engineering Chemistry** (2021), 104. 1-7

Publications not included in this thesis

1. G. Chen, **F. Buck**, I. Kistner, M. Widenmeyer, T. Schiestel, A. Schulz, M. Walker, A. Weidenkaff, A novel plasma-assisted hollow fiber membrane concept for efficiently separating oxygen from CO in a CO_2 plasma. **Chemical Engineering Journal** (2019), 392, 123699

2. **F. Buck**, K. Wiegers, A. Schulz, T. Schiestel, Keramische Hohlfasermembranen in einem Plasma-Membran-Reaktor, Keramische Zeitschrift (2021), 73, 38 - 43

3. **F. Buck**, K. Wiegers, A. Schulz, T. Schiestel, MIEC Hollow-Fibre Membranes in a Plasma Membrane Reactor. Interceram - International Ceramic Review (2021), 70, 40 - 45

Contributions to Conferences

1. **<u>F. Buck</u>**, K. Wiegers, A. Schulz, T. Schiestel, MIEC hollow fiber membranes for the separation of oxygen from a CO_2 plasma, 12th International Congress on Membranes and Membrane Processes, Web-Conference, 2020. (Poster)

2. **<u>F. Buck</u>**, K. Wiegers, A. Schulz, T. Schiestel, Plasmainduzierte CO_2 Spaltung mit Sauerstoffabtrennung durch MIEC Hohlfasermembranen, Web-Conference, 2020. (Poster)